Optimal Workloop Energetics of Muscle-Actuated Systems

by

Waleed A. Farahat

B.Sc. in Mechanical Engineering, The American University in Cairo (1997)
S.M. in Mechanical Engineering, Massachusetts Institute of Technology (2000)

Submitted to the Department of Mechanical Engineering
in partial fulfillment of the requirements for the degree of

Doctor of Philosophy

at the

MASSACHUSETTS INSTITUTE OF TECHNOLOGY

June 2007

Author .....
Department of Mechanical Engineering
May 4, 2007

Certified by .....
Hugh M. Herr
Assistant Professor of Health Science and Technology
Associate Professor of Media Arts and Sciences
Thesis Adviser

Certified by .....
H. Harry Asada
Professor of Mechanical Engineering
Thesis Committee Chair

Accepted by .....
Lallit Anand
Graduate Officer, Professor of Mechanical Engineering

Optimal Workloop Energetics of Muscle-Actuated Systems

by

Waleed A. Farahat

Submitted to the Department of Mechanical Engineering
on May 4, 2007, in partial fulfillment of the
requirements for the degree of
Doctor of Philosophy

Abstract

Skeletal muscles are the primary actuators that power, stabilize and control locomotive and functional motor tasks in biological systems. It is well known that coordinated action and co-activation of multiple muscles give rise to desirable effects such as enhanced postural and dynamic stability. In this thesis, we study the role of muscle co-activation from an energetics perspective: Are there situations in which antagonist co-activation leads to enhanced power generation, and if so, what is the underlying mechanism?

The mechanical energetics of muscles are traditionally characterized in terms of workloop measures where muscles are activated against oscillating, zero-admittance motion sources. We extend these measures to more natural, "mid-range" admittance loads, actuated by multiple muscles. Specifically, we set up the problem of a second-order mechanical system driven by a pair of antagonist muscles. This is the simplest problem where the influences of load dynamics and muscle co-activation on the output energetics may be investigated.

To enable experimentation, a muscle testing apparatus capable of real-time servo emulation of the load is developed and utilized for identification and workloop measurements. Using this apparatus, an experimentally identified model predicting muscle contractile force is proposed. Experimental data shows that with a simple Weiner structure, the model accounts for 74% (sigma = 5.6%) of the variance in muscle force, that force dependence on contraction velocity is minimal, and that a bilinear approximation of the output nonlinearity is warranted.

Based on this model we investigate what electrical stimulation input gives rise to maximal power transfer for a particular load. This question is cast in an optimal control framework. Necessary conditions for optimality are derived and methods for computing solutions are presented. Solutions demonstrate that the optimal stimulation frequencies must include the effects of muscle impedances, and that optimal co-activation levels are indeed modulated to enable a pair of muscles to produce more work synergistically rather than individually. Pilot experimental data supporting these notions is presented. Finally, we interpret these results in the context of the familiar engineering notion of impedance matching. These results shed new light on the role of antagonist co-activation from an energetics perspective.

Thesis Supervisor:

Hugh M. Herr

Associate Professor, Harvard-MIT Division of Health Sciences and Technology

Associate Professor, The Media Lab

Thesis Committee:

Anuradha Annaswamy
Senior Research Scientist, Department of Mechanical Engineering

H. Harry Asada – Thesis Committee Chair
Professor, Department of Mechanical Engineering

Neville Hogan
Professor, Department of Mechanical Engineering
Professor, Department of Brain & Cognitive Sciences

Acknowledgments

There are so many people who helped me and impacted me profoundly throughout the process leading up to this thesis. Now is my chance to thank them. My sincere thanks to:

Hugh Herr for giving me the intellectual freedom, full trust and full support to run with my research in whichever direction I chose; **Neville Hogan** for keeping me honest, setting the bar high, and for injecting a constant dose of enthusiasm; **Harry Asada** for serving as the chair of my committee, and for being genuinely interested in my work; **Anuradha Annaswamy** for her encouragement, thoughtful suggestions, and for serving on my committee; **Max Berniker**, for being one sharp guy one can always rely on for a healthy dose of critical feedback; **Sam Au**, for his genuine desire to help, and for his camaraderie; **Anna Ahn**, for teaching me a ton about muscles, workloops and how to run the experiments; **Katie Madden, Chris Auterie and Robert Marini**, for their invaluable veterinarian services – without them, I would be still running those experiments; **members of the Biomechatronics Group**, past and present, for being a fun group to be around; some deserve special mention, like **Dan Paluska**, for increasing the average coolness factor of our lab by threefold; **Bruce Deffenbaugh**, for consistently dragging me out of the lab to get sugar and caffeine; **Ken Pasch** for making everything look so easy; **Hartmut, Aaron and Sungho**, for helping me with my thesis defense presentation; **Ernesto Martinez** for being very helpful all around; **Leslie Regan and Joan Kravit** at the Mechanical Engineering Graduate Office, the latter for getting me into MIT, and the former for getting me out; **Danielle Guichard-Ashbrook and the staff of the International Students Office** for helping me overcome challenges at the beginning of my return to MIT; **the MIT Rowing Club** for making me get up at 5:00AM and brave the extreme cold to help clear my mind; **friends**, too many of them to count or list, thank you all; **my in-laws** for welcoming me into the family; **my family** for their long-distance, rock-solid, unwavering support – I have been constantly thinking about them all; and finally, my beautiful wife **Mayssam**, for being the most wonderful partner I could ever have.

This work was supported by the DARPA Biomolecular Motors Program (award N66001-02-C-8034) and the MIT Media Lab.

Contents

List of Figures

List of Tables

Chapter 1

Introduction

Skeletal muscles are the primary mechanical actuators in biological organisms. Their actions, which are modulated by neural input, powers, stabilize and control locomotive and functional motor tasks. Anatomically, muscles are situated to act on skeletal joints in groups of two or more with some degree of antagonism. It is well known that antagonist muscles co-activate simultaneously to enhance postural and dynamic stability of joints [37, 38, 32, 11]. The focus of this thesis is on the power-generating capability of muscles and the role antagonist co-activation plays in enhancing their energetics. Specifically, two questions are posed:

- How is the power generating capability of muscle maximized?
- Are there situations in which antagonist co-activation leads to enhanced muscle power generation, and if so, what is the underlying mechanism?

These questions touch upon three distinct but interrelated areas of research: i) muscle physiology and biomechanics, ii) biological motor control, and iii) functional electrical stimulation. Skeletal muscles play a central role in all these areas, but are studied from different perspectives and with different objectives in mind. In what follows, we briefly discuss these three areas, and describe how they relate to the questions.

1.1 Muscle physiology and biomechanics

Under appropriate neural control, muscles provide a variety of biomechanical motor functions that are rich and subtle. *In vivo* measurements have shown that muscles approximate the actions of power generating sources, springs, struts, dampers, or a combination thereof [18]. Such behaviors are in part due to the intrinsic mechanical properties of muscle, and in part due to feedforward and feedback neural control [77, 2]. Numerous biomechanical studies have focused on investigating how muscles give rise to such behaviors [73], and providing correlations between muscle properties, electro-myographic (EMG) measurements, biomechanical constraints, and motor control objectives. Figure 1-1, which is reproduced from [18], shows an exposition of the wide range of muscle functions that are used in locomotion.

To understand what gives rise to such responses, it is necessary to look carefully at the microscopic structure of skeletal muscles, and how it relates to their macro scale properties. Appendix A provides a basic description of the contractile mechanisms of muscle and their properties.

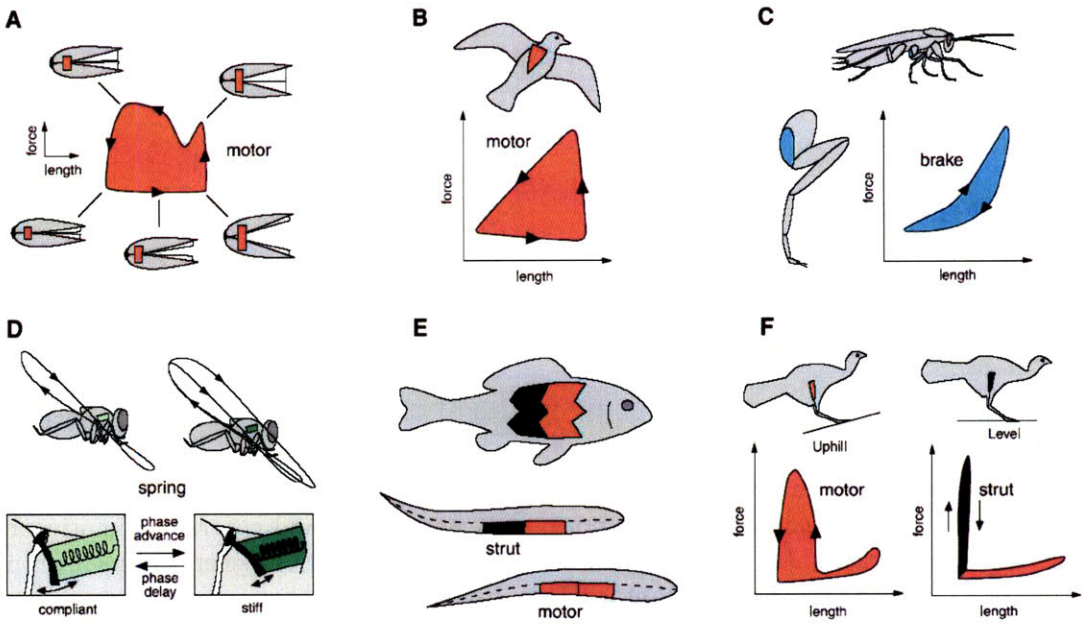

Figure 1-1: Reproduced from [18] with permission. Muscles play a wide range of biomechanical functions that can be described succinctly in terms of workloops.

Workloops

In the muscle physiology literature, the capability of muscles to generate mechanical work has been traditionally characterized in terms of *workloop measurements* [46]. In these measurements, the muscle is subjected to prescribed sinusoidal length variations in time by means of an external motion source. An electrical stimulus is triggered at a particular phase of the cycle, resulting in a contractile force. A plot of measured force vs. displacement results in a workloop plot. The area enclosed in the workloop is a measure of the mechanical work done by the muscle on its environment (its mechanical energetics). In [46, 69, 68, 53, 16, 43, 47, 2], the dependence of the energetics of muscles on electrical stimulus parameters was investigated and correlated with the biological functions of particular muscles.

Workloops may be viewed not only as measures of muscle power, but also as succinct descriptions of the biomechanical roles that muscles play under periodic motions. While the area enclosed by the workloop is an indication of the amount of mechanical work done by the muscle, its shape, volume and directional sense can be interpreted in relation to the function of the muscle. For example, in Figure 1-1, power generating muscles produce more voluminous workloops, whereas power dissipating muscles produce workloops that have a different directional sense. If the workloops are of small volume, this would indicated that they have more of a structural function, such as a stiffness element, a strut, or in some cases a clutching mechanism.

1.2 Biological motor control

Research in biological motor control seeks to understand how the actions of multiple muscles are coordinated to give rise to motor behavior. A central theme is the interplay between the

mechanical properties of muscles, and how motion is generated and stabilized. One of the clearest examples of this is the relationship between active muscle force, and the impedance of a muscle. As a muscle is activated, not only that a contractile force is generated, but also its output stiffness and damping increase dramatically. From an engineering perspective, this coupling confounds the control problem and makes it more challenging. Yet this feature is exploited by the central nervous system advantageously. It has been suggested that for muscles acting in concert about a common joint, antagonist muscles may provide the central nervous system with the capability of modulating the stiffness of the joints. This is achieved via *co-activation of antagonist muscles.* Co-activation has been observed to play an important role in postural and dynamics stability.

In this thesis we study the role of muscle impedance and co-activation from an energetics perspective, and offer a parallel motivation for co-activation. The same mechanisms that stiffen a joint for stabilization purposes may also be used to modulate joint impedance, and therefore enhance power transfer. Connections with the engineering notion of impedance matching are therefore be drawn.

1.3 Functional electrical stimulation

Functional electrical stimulation (FES) is the artificial stimulation of muscles *in vivo* to rehabilitate functional capabilities. It has been an active area of research, with the elusive goal of re-animating limbs and motor skills that are adversely affected either due to paralysis or other neurological disorders.

In the FES literature, much attention has been directed to the problem of developing algorithms for controlling the mechanical response (particularly contractile force) of muscle via artificial electrical stimulation [72, 15, 13, 14, 71, 44, 61, 31, 17]. The basic motivation is that FES may provide a compelling rehabilitation modality for spinal chord injuries (SCI) and stroke subjects. This gave rise to an extensive literature that focuses on many of the subproblems such as: what muscle models should be used, [9, 67, 63], what system identification schemes [12, 22, 21], what electrodes and stimulation patterns [52, 33, 75], and so forth.

The predominant approach in the FES literature has been to control muscles to act as ideal (impedance-free) force sources, and then using those " force sources" to provide the desired functions via an outer control loop. This approach seems to be influenced by approaches in robotics that involve actuation by motors, which ideally are impedance free, but has the drawback of attempting to negate some of the inherent muscle dynamics. In this thesis, however, we focus directly on the desired functions, while operating within the constraints imposed by the muscle dynamics. In doing so, it may be possible to harness some of the muscle properties in a manner the enhances performance. The particular function chosen is that of power generation.

1.4 Where does this thesis lie?

This thesis lies at the intersection of the three fields mentioned above. It is worthwhile repeating the question here:

- How is the power generating capability of muscle maximized?

- Are there situations in which antagonist co-activation leads to enhanced muscle power generation, and if so, what is the underlying mechanism?

In relation to biomechanics, the focus of this thesis is on the capability of muscle to do mechanical work on a load, and how this capability is achieved and maximized. In relation to biological motor control, the focus is on how the actions of multiple muscles are coordinated to maximize power energetics. In relation to FES, instead of focusing on force trajectory tracking, we focus directly on the power generating capability of muscles.

Problem Setup Choosing an appropriate problem setup as an embodiment for answering these questions is crucial. The problem should be rich enough to test for the desired effects, but stripped of superfluous details. The problem setup is shown in Figure 1-2.

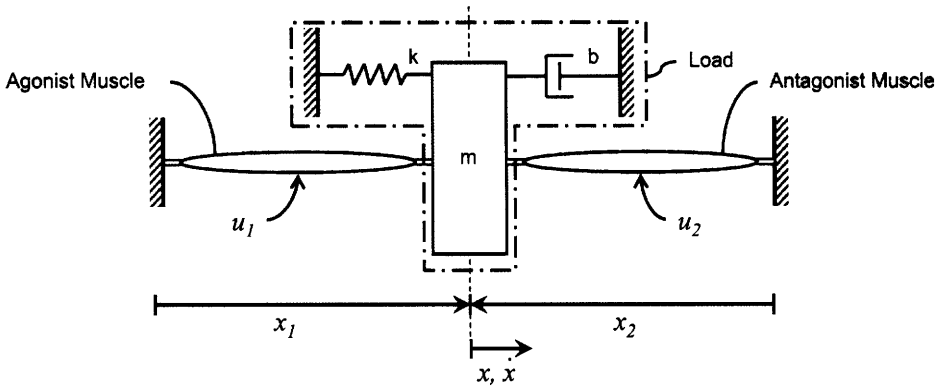

Figure 1-2: Problem setup: antagonist muscle pair acting on a second order mechanical load.

Why choose this setup? First, it is general enough to model antagonist mono-articular muscles actuating a single degree-of-freedom joint acting on realistic loads such as ankle muscles delivering power to the body during normal walking. Second, this is the simplest system in which the net force produced by the muscles can be modulated with some degree of independence over the net stiffness by appropriately co-contracting the muscles – a problem with only one muscle will not allow for this effect. Third, by simplifying the muscle loads to well understood, but non-trivial loads, we can focus our attention on the muscle response, and eliminate the complexities of real skeletal loads. Finally, the load has to be a non-zero admittance load, otherwise the muscles would not be able to "feel" the effects of one another since the motion source acts as a barrier preventing them from communicating mechanically.

Approach The first question is tackled via model-based optimal control, with the objective of finding what electrical stimulation input to the muscles maximizes their power output. The optimization requires a mathematically tractable model describing the problem setup. The models are obtained via system identification methods, and are based on experimentally measured data.

The second question is answered via computation of the optimal controls, and observing the effect of co-activation on the solutions. Conclusions based on the optimization of the computations are then verified experimentally.

1.5 Dissertation Overview and Contributions

This dissertation is organized around the main contributions of the thesis:

- One of the main challenges in muscle research is robust experimentation. Chapter 2 presents the design and hardware implementation of a muscle testing apparatus that is used as the experimental platform for a wide variety of experiments. It is fitting that this chapter is presented early on since this apparatus is used as a test platform for all experiments conducted in this thesis, including muscle identification and workloop energetics measurements.

- Chapter 3 presents a method for identification of dynamical models that describe the contractile dynamics of muscles undergoing periodic oscillation. We assess the ability of multi-affine models to capture the force response of the muscles. We conclude that bilinear models with no velocity dependence are sufficient.

- Chapter 4 discusses the problem of maximizing the the power generated by muscles against a passive second order mechanical system. Several approaches are taken, ranging from the mechanistically intuitive to the mathematically rigorous. Basic analysis shows that co-activation can be beneficial from an energetics point of view. Then via direct simulations and optimal control analysis, we show that for a full-fledged model that this indeed is the case. The computed optimal solutions demonstrate that the optimal stimulation frequency must include the effects of muscle impedances, and that optimal co-activation levels are indeed modulated to enable a pair of muscles to produce more work synergistically rather than individually. Roughly this means that a muscle pair when working in concert under optimal conditions can produce more work than individual muscles, also working optimally. Finally, the results are interpreted in the context of impedance matching conditions (in conjunction with the development in Appendix B).

- Chapter 5 describes the results of workloop experiments in relation to the predictions of the optimization work of Chapter 4. The experimental results support optimization conclusions.

- Finally, in Chapter 6, we summarize the conclusions and present directions for future work.

Enjoy!

Chapter 2

Experimental Apparatus and Methods

In this chapter I describe the experimental approach and apparatus utilized in the identification and energetics measurements of chapters 3 and 5. This chapter is essentially a reprint of [26]. The focus is to describe the apparatus (hardware components, integration and real-time software implementation) as well as some of the experiments that are possible under the system architecture. For illustration purposes, experimental measurements comparing single muscle workloops under zero and non-zero admittance loads are presented. In doing so, methods for conducting experiments on isolated skeletal muscles harvested from frogs are also described.

2.1 Motivation for Hardware Development

Muscle biomechanists have evaluated the mechanical response of muscle cells and tissues using a variety of experimental approaches, including isometric force-length characterizations [36, 35, 74, 56, 42], force-velocity testing [34, 23, 55, 4], quick release motion profiles [74, 56], and workloop testing [46, 69, 68, 70, 47]. These classical experimental protocols can be classified in one of two categories: i) position-trajectory controlled experiments, or ii) force-controlled experiments. In position-trajectory controlled experiments, the motion of the endpoints of the muscle-tendon structure is controlled as a predetermined function of time. This motion is usually delivered by means of a mechanical servo-system attached to the end points of the muscle-tendon structure. Consequently, the contractile forces generated by the muscle do not affect its endpoint motion trajectory. In distinction, in force-controlled experiments, the force imposed on the muscle is regulated independent of its motion. Therefore, as the muscle moves, there is no change in the reaction forces from its surroundings. Force controlled experiments are mostly implemented via a force feedback servo, but simple dead weights may be used. Examples of position-trajectory controlled experiments include isometric force-length experiments where muscle position is regulated at constant length, standard sinusoidal workloop experiments where muscle strain follows a sinusoidal path in time, and force-velocity experiments where the velocity is the independent variable. Examples of force-controlled experiments include quick release experiments, where the force imposed on the muscle is regulated to zero, and force-velocity experiments, where the force is the independent variable.

These two experimental categories offer two extremes of the load admittance range. In

position-trajectory control mode, the admittance of the mechanical boundary conditions acting on the muscle is ideally zero (practically to within limitations of the servo-system used). In force-control mode, the admittance is ideally infinite, since there will be no change in force applied on the muscle due to a change in its length or velocity. Catering to such experimental requirements, standard off-the-shelf muscle testing systems provide dual-mode servo functionality, corresponding to these two extremes [65].

Therefore the question arises as to whether testing for finite (but non-zero) admittance boundary conditions is necessary to fully characterize muscle tissue. Clearly, to understand *in vivo* tissue performance, muscle dynamics and the dynamics of the load for which the muscle acts upon must be taken into consideration. Examples of finite-admittance boundary conditions include loads such as springs, dampers, masses, drag friction, coulomb friction, or a combination thereof. Such loads prescribe boundary conditions that are generally defined in terms of dynamic relationships between force and displacement. Under these loading conditions, it would be expected that the dynamics of the load will interact with the contraction dynamics of the muscle, leading to a behavior that is a resultant of both. This is primarily because the force generated by the muscle is dependent on its mechanical state, namely its length and velocity. Several researchers characterized muscle under such loads by developing task specific apparatuses. Bawa [6, 5] characterized muscle under inertial and elastic loads. Krylow and Rymer [48] and Zhou [78] characterized muscle under pure inertial loading.

Aside from the need for generalized boundary conditions, there is increasing experimental interest in real-time control of muscle, primarily in the context of Functional Electrical Stimulation (FES) [13, 72, 71, 30, 44, 31, 25, 14]. In these investigations, attempts were made to control the response of muscle(s) and associated loads to a desired trajectory by varying electrical stimulation parameters as a function of time. Electrical stimulation patterns are typically square pulses characterized by frequency, amplitude, pulse-width and number of pulses per trigger (considering the cases of doublets, triplets, or more generally N-lets). In feedback experiments, these parameters are varied by a control algorithm to achieve a desired muscle response. Feedback control via pulse width modulation has been popular [13, 72, 71, 44, 31] due to ease of implementation, and is preferred over amplitude modulation since it minimizes tissue damage [14]. In [25] frequency was modulated, and in [14], both frequency and pulse width were modulated. In [75, 57] the number of pulses per cycle was modulated. For testing a variety of FES algorithms, an experimental apparatus is needed that is capable of real-time modulation of stimulation parameters as a function of a muscle's mechanical response.

In this chapter we present a system that can implement muscle testing protocols under generalized boundary conditions while also providing flexible feedback control of electrical stimulation parameters (see for examples [22, 20, 49]). These features are accomplished by having two real-time control loops running in parallel (see Figure 2-1). The first loop, the Mechanical Boundary Conditions (MBC) control loop, ensures that the mechanical response of the servo simulates the dynamics of the associated muscle boundary condition. For example, if the desired boundary condition is a linear spring, the MBC control loop controls the motion of the end points of the muscle-tendon to be proportional to the force generated by the muscle. The second loop implements the electrical stimulus control based on measurements of the muscle's mechanical response. This loop, referred to as the Electrical Stimulus (ES) control loop, offers simultaneous real-time modulation of pulse-width, amplitude, frequency, and the number of pulses per cycle.

In one experimental embodiment, dynamic boundary conditions may be applied to a

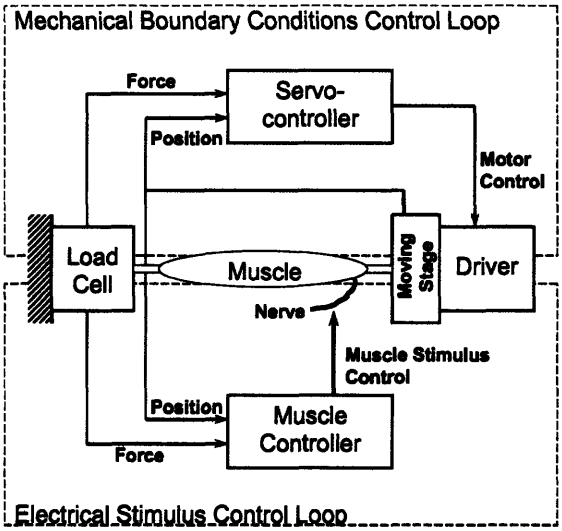

Figure 2-1: Two control loops are operating simultaneously. The Mechanical Boundary Conditions (MBC) control loop causes the moving stage to simulate desired boundary conditions based on current position and force signals. The Electrical Stimulus (ES) control loop regulates muscle stimulus based on mechanical response.

muscle performing workloops. As a demonstration of the capabilities of the system, we present this new approach to workloop experiments for oscillatory power output measurements. The experiments were performed on *Plantaris longus* muscles of *Rana pipiens*. We show pilot data illustrating the difference between the finite-admittance testing method and current standard methods reported in the muscle workloops literature [46].

In Section 2.2 we provide a description of the apparatus, and in Section 2.4, we discuss various experimental protocols that are easily implemented using the apparatus. Finally, in Section 2.5, we present workloop experimental data of muscle acting against finite and zero-admittance boundary conditions.

2.2 Muscle Testing Apparatus

Figure 2-2 summarizes the system. A description of its functional requirements and components follows.

2.2.1 Functional Requirements

Off-the-shelf dual-mode servo muscle testing systems are capable of generating classical muscle characterizations mentioned in Section 2.1. In addition, the following functional requirements are recognized:

Capability to implement generalized dynamic boundary conditions on muscle This involves simulating the different mechanical environments with which a muscle interacts. A flexible approach would be to simulate such environments in software, and allow for a servo-system to deliver their response. The servo-system needs to be responsive enough to accommodate force disturbances generated by the muscle. A bandwidth > 120 Hz was determined as a requirement for the muscles under consideration (*Rana pipien* jumping

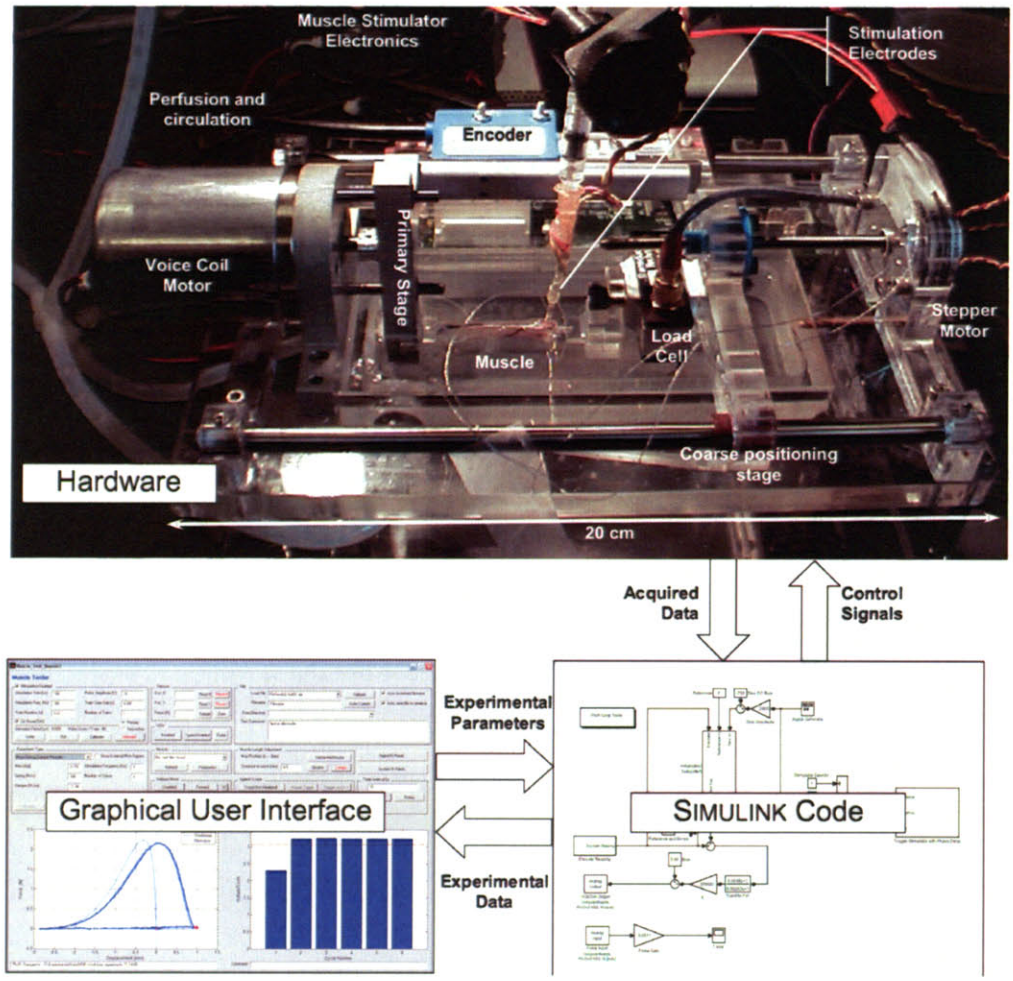

Figure 2-2: Overall system summary. Experimental definitions and parameters are entered via the Graphical User Interface, which in turn invokes the appropriate SIMULINK block diagram and downloads the experimental parameters. The real-time code then takes control over the hardware to acquire the muscle data, which is then sent back to the GUI for post-processing. The apparatus is shown above with the primary sensors and actuators noted. The coarse positioning stage is adjusted at the beginning of the experiment to accommodate different lengths, but is typically kept at a constant position during a particular contraction. The primary stage provides the motion that simulates the boundary conditions. The muscle shown in the apparatus is a frog (*Rana pipien*) *semimembranosus* muscle submerged in Ringer's solution. The vertical syringe has a suction electrode at its tip that is connected to the stimulation electronics in the background. Silicone tubing recirculates solution via a peristaltic pump, while oxygen is injected in the loop.

muscles). This estimate was based on the rise time of a typical twitch force profile (typically 40 ms). This requirement is fulfilled by the MBC control loop shown in Figure 2-1. A closed-loop impedance of 20 kN/m, approximately corresponding to 1% muscle strain at maximum force, was deemed sufficient.

Electrical stimulus real-time feedback control For FES and control purposes, the system should allow for real-time changes to the signal parameters as a function of the muscle's mechanical state. This requirement is fulfilled by the ES control loop shown in Figure 2-1.

Testing of agonistic/antagonistic muscle pairs In a single muscle arrangement, the force and impedance of the muscle are both modulated simultaneously by its activation level. At least two muscles are needed to achieve independent control of impedance and net force generation over a joint. A testing apparatus, or a combination of apparatuses, should be capable of mimicking a situation where agonistic and antagonistic muscles act against a common load. This requirement is fulfilled by connecting two testing apparatuses to the same PC, and controlling them by the same real-time process. The two systems are therefore linked in software, and are essentially seeing the same virtual load. As the antagonistic contracts, the agonist stretches commensurately. Under this arrangement, not only can the system be used for motion trajectory control via the muscle pair, but also for muscle impedance control strategies.

2.2.2 Sensors/Actuators

The sizing of the components for the apparatus depends on the type of muscles desired for experimentation. The particular unit presented here is sized to accommodate muscles extracted from *Rana pipien* frogs (e.g. *semitendinosus*, *semimembranosus*, *plantaris longus*, etc.). These muscles are typically less than 15-25 mm in length (muscle belly, at l_o, the length corresponding to maximum force output), with a mass < 1 gram. The maximum forces generated by these particular muscles are on the order of 3-5 N. *In-vivo* aggregate strains are generally less than $\pm$ 15%, resulting in end point motion of less than $\pm$ 4 mm [1, 60]. The time to peak force in a twitch is typically 30-40 ms. During apparatus design, these figures guided the selection of sensors and actuators.

A two-actuator approach was used to achieve large-stroke and high-bandwidth.

- A linear stepper motor actuator [Haydon Switch and Instruments] provides a large travel stroke of the coarse positioning stage, covering a total span of over 100 mm. The actuator is driven by a bi-polar stepper motor driver.

- A high-bandwidth voice coil motor (VCM) [BEI Kimco] provides fine positioning of the primary stage. A transconductance H-bridge amplifier [Centent Company] drives current through the VCM, resulting in a force proportional to current that acts on the moving mass. The VCM has a smaller stroke ($\pm$ 4 mm) [1] and a stall force of ($\pm$ 30 N).

[1] This stroke range is sufficient for *in-vivo* like strains for the muscles considered. Larger strokes may be achieved by combined dual control of the linear stepper motor and the VCM [64]. While this feature has not been implemented yet, its implementation is straight-forward within the software framework described below.

During initialization of a particular experiment, the coarse stage positioning stepper motor is adjusted to accommodate the nominal length of the muscle under experimentation. Its location is typically held fixed for the duration of the experiment. The high-bandwidth actuator takes control to provide desired endpoint motions, rejecting disturbances due to muscle contraction via the servo loop.

Position sensing is attained by a 1 μm resolution, incremental, non-contact magnetic encoder [SIKO Products]. In-series force sensing is attained via a strain gage based load cell [Transducer Techniques Inc.] in conjunction with a wheat-stone bridge amplifier [2].

An electric stimulator with real-time programmable pulse parameters is implemented via an H-bridge design on a custom built breakout board. The stimulus is controlled by a Field Programmable Gate Array that controls all stimulus timing parameters. Stimulator specifications are provided in Table 2.2.

2.2.3 Integration and Design

The sensors and actuators are mechanically integrated into the design shown in Figure 2-2. A breakout board was designed to integrate all the system components electrically, to provide stimulation to the muscle via an onboard programmable stimulator, and to act as a communication interface between the hardware and the real-time software.

2.2.4 Mechanical Boundary Conditions Control Loop

As is the case with standard muscle testing apparatuses, the mechanical boundary conditions control loop can be operated in direct position-trajectory control mode and in force-control mode. Additionally, implementation of simulated dynamic boundary conditions is achieved by directly measuring the muscle force, filtering it through the transfer function of the desired boundary condition, and directing the result as the new reference position of the servo controller. This assumes that the bandwidth of the servo-system is high enough to accommodate the dynamics of the simulated boundaries, and that the backloading effects of the muscle are small. Typically, this condition is satisfied. Boundary conditions of interest have natural frequencies <10 Hz, which is well below the servo-system bandwidth.

Experimentally identified closed-loop bode plots confirm a -3 dB bandwidth of 150 Hz for the MBC control loop. (See Figure 2-3). Root locus analysis was performed to ensure that this bandwidth and stability are not compromised as the muscle stiffness changes. Section 2.3 summarizes the system's servo-mechanical performance metrics.

2.2.5 Electrical Stimulus Control Loop

The electrical stimulus applied to the muscle is a pulse train that is characterized by amplitude, pulse width, period between pulses, and number of pulses per trigger. All four quantities can be controlled in real-time, simultaneously and independently. In feedback muscle control experiments, these parameters are typically a function of the mechanical response of the muscle-actuated system (that is, the muscle in a given experiment, and its virtual load that is simulated by the mechanical boundary conditions control loop). Table 2.2 summarizes the electrical stimulator specifications.

[2]The in-series measured force is assumed to be entirely due to the contraction of the muscle. Inertial effects due to acceleration of the muscle mass were estimated to be 3 orders of magnitude less than its contractile force, and therefore safely neglected.

2.2.6 Control Implementation

Real-time control, data acquisition and storage are implemented under the MATLAB Real-Time Workshop, SIMULINK and the xPC Target [Mathworks Inc.]. A multipurpose data acquisition card [Measurement Computing] is used in conjunction with a target PC to communicate with the breakout board. Control and data acquisition sampling rates are set at 2 kHz. A library of block diagrams implementing different experimental logics is developed. New experiments are easily added since all that is required is the generation of the appropriate SIMULINK block diagram.

2.2.7 Graphical User Interface

A graphical user interface implemented in MATLAB's Graphical User Interface Development Environment (GUIDE) allows the user to select and control all experimental parameters. The interface invokes the real-time code to operate and trigger data-acquisition for a particular experiment. It also invokes appropriate subroutines for high-level data post-processing and plotting.

2.3 System specifications

The performance specifications of the servo-mechanical system are summarized in Table 2.1. Table 2.2 shows the specifications of the electrical stimulus parameters. Figure 2-3 shows the closed-loop position frequency response of the mechanical boundary conditions (MBC) control-loop.

Table 2.1: Servo-mechanical specifications

Displacement	Total coarse positioning range	0 - 100 mm
	Sensing resolution	1 μm
	Voice coil motor range	8 mm
Force	Sensing range	$\pm$ 22.5 N
	Sensing resolution	1 mN
Bandwidth	Open-loop	92 Hz
	Closed-loop	153 Hz
	Gain margin	14 dB
	Phase margin	$>$ 50 degrees
Voice coil motor	Stall Force	$\pm$ 30 N

Table 2.2: Stimulator Electrical Specifications

Amplitude	Max	16.2 V
	Resolution	0.25 mV
	Saturation Current	25 mA
Output Impedance	Driving high	4.7 Ω
	Driving low	2.2 Ω
Waveform	Bipolar square pulses,	both electrodes driving
Pulse width	Max	0.32 s
	Resolution	1 μs
Pulse interval	Max	0.32 s
	Resolution	1 μs
Pulse count	1 to 65,536	pulses per trigger

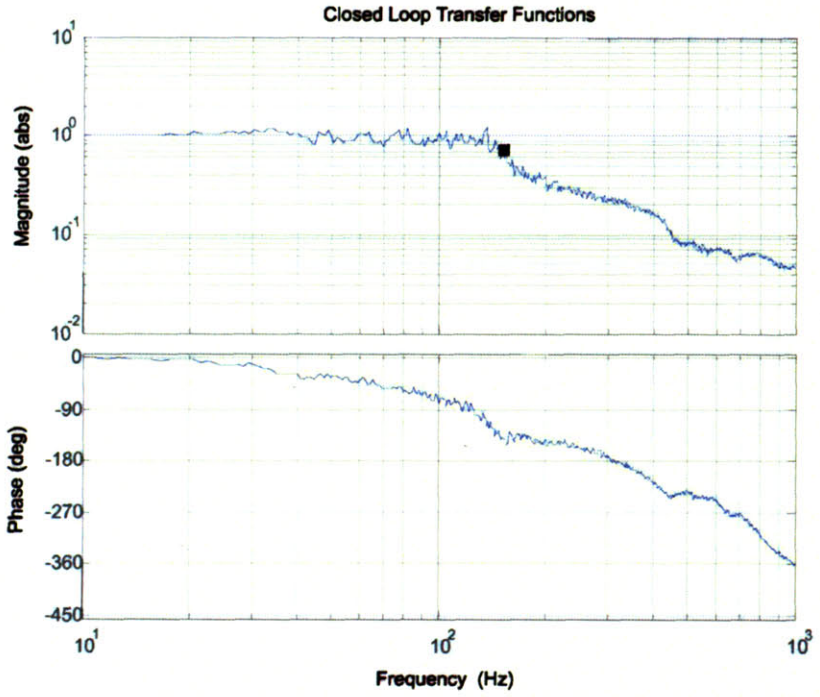

Figure 2-3: Unloaded closed-loop position frequency response of the mechanical boundary conditions (MBC) control-loop. Shown is the experimentally measured transfer function from desired reference motion to actual motion. The -3 dB bandwidth was measured at 153 Hz. Actuator reference signal was white noise (to within sampling frequency), with a standard deviation $\sigma = 1$ mm, implying a 6σ range of ± 3 mm.

2.4 Experimental Applications

In this section we provide descriptions of potential experimental protocols that can be implemented using the muscle testing apparatus.

Muscle Identification Experiments Basic open-loop muscle identification experiments including force-length, force-velocity, quick release and workloop characterizations can be implemented using the apparatus. Here the term open-loop refers to the electrical stimulus since it is predetermined at the start of an experiment. In classical muscle characterization experiments, the boundary conditions implemented have generally been constant length, constant velocity or constant force boundary conditions [74, 56, 23, 55, 4]. Furthermore, pseudo-binary random sequence (PBRS) identification and deconvolution methods have been implemented under isometric conditions to identify the muscle recruitment characteristics [31, 8, 22]. The apparatus presented here may extend these experiments in the context of generalized boundary conditions.

Position/Force Control of a Simulated Load Using Electrical Stimulus Feedback The objective of this experiment would be to test algorithms for position control of a known load via muscle actuation. See for example [22] and [49]. Here the MBC control loop would simulate the dynamics of the load, (e.g. a second order mass-spring-damper system) while the ES control loop would implement the algorithms being evaluated.

Impedance control of Agonistic/Antagonistic Pairs It is known that co-contraction is employed to increase the output impedance of muscle-actuated systems [37]. Implementing impedance control (without human supervisory control as in [20]) in electrically stimulated muscle systems has not been demonstrated experimentally to the authors' knowledge, and is considered an open area of research. Using two apparatuses in an agonistic/antagonistic muscle testing arrangement would allow for the testing of control strategies with impedance as the desired output. Here the impedance of the closed loop (muscle plus simulated load) system would be measured via perturbation response.

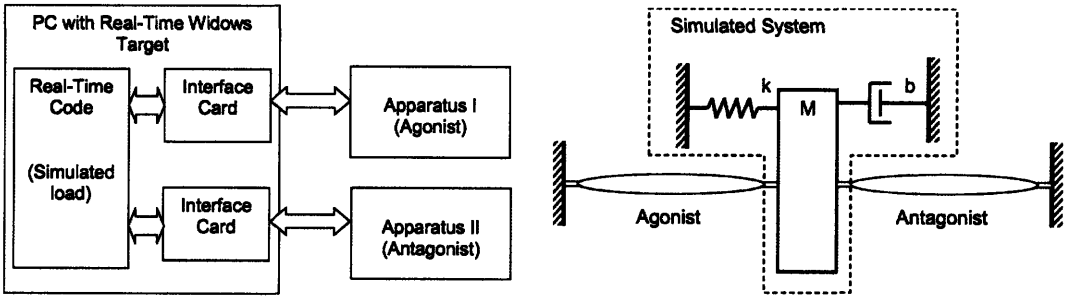

(a) System setup

(b) Agonist-antagonist pair acting on common load

Figure 2-4: Setup for agonist antagonist control experiments. 2-4(a) Two testing apparatuses are controlled by the same program, simulating the physical system shown in 2-4(b)

Fatigue Studies It has been reported that the number of pulses per cycle affects the fatigue life of a muscle undergoing electrical stimulation [57, 75]. The experiments in [57]

and [75] focused on isometric development. Using the apparatus presented, fatigue studies may be implemented under generalized boundary conditions.

Identification of Muscle Workloop Power Output Under Finite Admittance Boundary Conditions The capacity of muscles to generate mechanical power output has been characterized in terms of workloops. In [46], Josephson presented a method of measuring muscle workloop output under sinusoidal conditions. This method set the standard for muscle workloop testing in the muscle physiology literature. Briefly described, the muscle is subjected to prescribed sinusoidal length variations in time. An electrical stimulus is triggered at a particular phase of the cycle, resulting in a contractile force. A plot of force vs. displacement results in a workloop plot (as in Figure 2-5(a) and 2-5(c)). The area enclosed in the workloop is a measure of mechanical the work output by the muscle. In [46, 69, 68, 53, 16, 43, 47, 2] the dependence of the energetics of muscles on electrical stimulus parameters was investigated, and was correlated with the biological functionality of particular muscles.

The testing methodology in [46] is essentially an zero-admittance testing methodology. A richer test would be to have the muscle perform workloop experiments under passive, finite-admittance loads. In this scheme the muscle stimulus is triggered at a particular frequency. Consequently a force is generated, that results in a motion trajectory that is dependent on the boundary conditions. This alters the character of the workloop output of the muscle, and therefore the muscle energetics estimate. Sample results for this particular experiment are presented in the next section.

2.5 Pilot Data of Workloop Experiments

In this section we present pilot data on the workloop experiments described in 2.4. Pilot data are presented as an illustration of the system's capacity to measure workloop power production under finite-admittance boundary conditions. Using the MBC control loop, a second order mass-spring-damper system is simulated as the compliant boundary condition against which the experimental muscle specimen acts. This experiment is designed to show how muscle power output may change significantly in the context of a finite-admittance boundary condition compared to the traditional zero-admittance motion source first proposed by Josephson [46].

2.5.1 Methods

Plantaris longus muscles were dissected out of adult male *Rana pipiens* (approx. 30 gram frogs). Prior to removal from the animal, the muscle rest length was measured with both the knee joint and the hip joint positioned at 90 degrees. To minimize tendon damage, the muscle was removed with bone chips attached to both ends. A reflex clip was stapled to the bone chips, tightly sutured, and secured to the interface points in the testing apparatus via a dove tail connection (the muscle's distal end to the primary stage, and the proximal end to the coarse positioning stage through the load cell). Periodic testing throughout the experiment ensured that there was no slack or slippage of the muscle specimen. Tests included visual inspection as well as monitoring the shape and peak levels of single isometric twitch force profiles. The muscle was submerged in a tub of Ringer's solution that was circulated via a peristaltic pump. The solution was generously oxygenated via direct O_2 gas bubbling at an insertion point in the circulation loop.

Stimulation was delivered through a suction electrode to the sciatic nerve of the muscle. Initial successive isometric twitch measurements were used to establish full recruitment voltage levels, beyond which there was no increase in force production. Additionally, isometric twitch tests were interleaved periodically within experimental measurements to ensure that the muscle did not fatigue, and that force production levels remained constant throughout the duration of the experimental session. When muscle twitch force levels decreased to below 90% of their initial value, the ensuing data were discarded.

Electrical stimulus parameters were set at: pulse frequency = 200 Hz, pulse width = 100 μs, and amplitude = full recruitment voltage[3]. Two sets of data with stimulation durations of 40 ms and 60 ms were acquired. For the zero-admittance cases, the stimulation was triggered at 90° phase, corresponding to the point of maximal stretch.

In the zero-admittance case, the motion of the endpoints was sinusoidal with a frequency of 4 Hz and an amplitude of ± 2 mm. Correspondingly, for the finite admittance case, the natural frequency of the passive load and the frequency of the stimulus trigger were both set at 4 Hz. The stimulus trigger was matched with the system's resonance frequency so as to produce maximum amplitude excursions. This condition provided the highest energy absorption in the simulated damper, or the highest muscle workloop power output. The static stiffness of the simulated load was set such that the resulting motion had the same amplitude as that of the zero-admittance case for relevant comparison.

2.5.2 Results

Sample experimental results are plotted in Figure 2-5. In the zero-admittance case (Figures 2-5(a) and 2-5(c)), the motion was driven by the servo-system, and the muscle force did not affect its motion trajectory. In the finite admittance case (Figures 2-5(b) and 2-5(d)), the motion was caused by the muscle force.

Energy output was estimated by integrating the areas inside the workloops. To normalize the results, power output was divided by the total muscle mass. The normalized results are summarized in Table 2.3. Under the described conditions, muscle preparations typically lasted for 5-15 data sets (similar to that shown in Figure 2-5) over the course of 1-3 hours.

Table 2.3: Experimental Workloop Muscle Power Output

Stimulation Duration	FAW [Watt/kg]	ZAW [Watt/kg]	Ratio [%]
40 ms	14.7 ± 0.25	29.3 ± 0.43	50.1
60 ms	18.0 ± 0.38	31.7 ± 0.31	56.8

Muscle power output for finite-admittance workloops (FAW) and zero-admittance workloops (ZIW). Data shown are mean $\pm$ S.E., $N = 6$ workloop trials for each case.

[3]In the muscle workloop literature (see for example [46, 69, 1]), the muscle is typically overstimulated to guarantee full recruitment. While this decreases the *in-vitro* life of the muscle, we opted to use such patterns to enable relevant comparison with established data

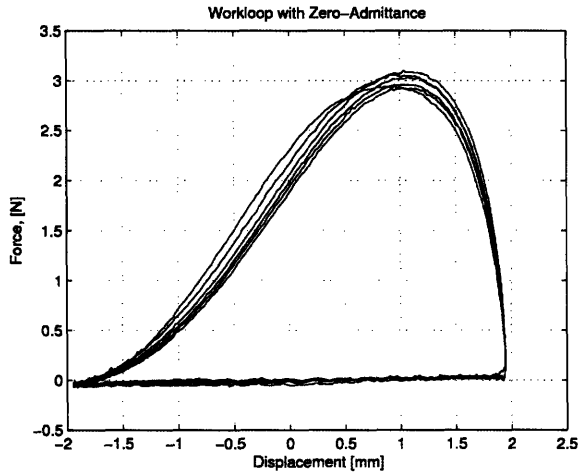

(a) Zero-Admittance Workloop

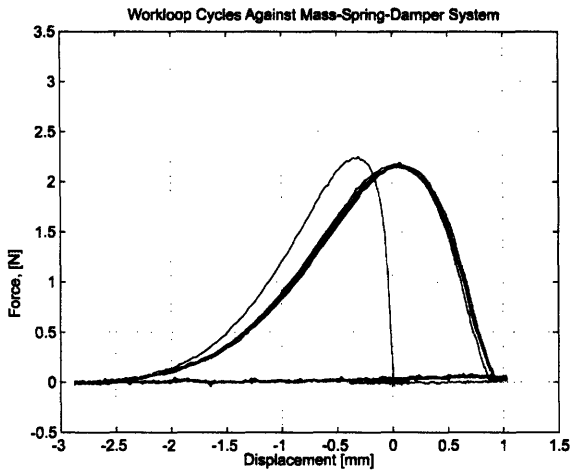

(b) Finite-Impedance Workloop

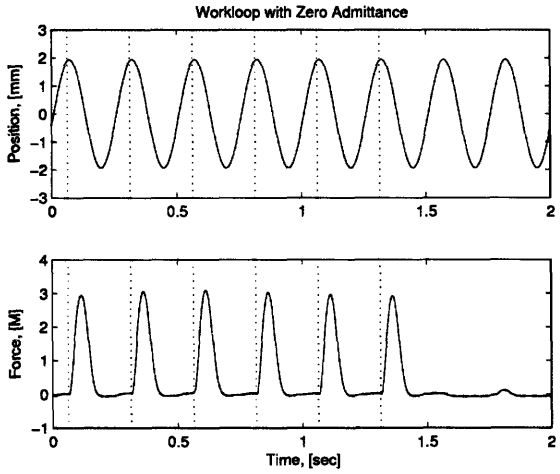

(c) Zero-Admittance Position and Force Time Trajectories

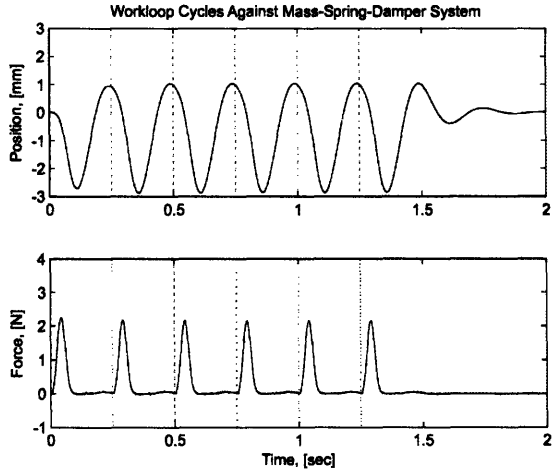

(d) Finite-Impedance Position and Force Time Trajectories

Figure 2-5: Comparison of zero-admittance workloops (ZAW) vs. finite-admittance workloops (FAW). Here the FAW power output was 56% of that of the ZAW. (a) Sinusoidal stimulation with frequency of 4 Hz and amplitude = 20 % strain. (b) Workloop plot with a mass-spring-damper boundary condition. Parameters for this particular measurement are: $m = 0.79$ kg, $k = 500$ N/m, $b = 11.9$ Ns/m. These parameters were chosen such that the natural frequency $\omega_n = 4$ Hz = stimulation frequency, damping ratio $\zeta = 0.3$, and static gain $k_s = 10\%$ strain at maximum force generated.

2.6 Discussion

The measurements of Section 2.5 indicate that although the motion of the muscle had the same frequency and peak-to-peak amplitude in both the zero and finite admittance cases, the power output was substantially different (almost by a factor of 2). This is primarily attributed to the dependence of muscle force output on its mechanical state. Changing boundary conditions changes the dynamic relationship between state and force, and therefore the character of the work output.

While these experimental results are meant as an illustration of the capabilities of the testing apparatus, they lead to a set of interesting research directions regarding muscle energetics. Specifically, there is a need to understand how muscle workloop performance changes with boundary condition admittance, as described by natural frequency, damping ratio, and spring stiffness. Experiments of this nature may provide important insights as to how muscle power output is affected by the nature of the task at hand, and in light of variations in muscle environment. While it not surprising that the power generated by a muscle is influenced by its boundary conditions, the methods presented provide a direct means of quantification.

In the muscle control arena, the apparatus may also be employed to investigate the merits of different algorithms. Typical muscle control investigations, specially in the context of FES, are conducted on limbs where muscular contraction dynamics confound with complexities of skeletal dynamics. This results in a highly complicated problem. One way to decompose this complexity is to simulate idealized loads acted upon by the muscle. The apparatus presented here allows for the implementation of such idealized loads precisely via the MBC control loop. This includes linear, nonlinear, as well as loads that simulate actual *in vivo* biomechanics. The simulation of idealized loads in series with the muscle specimen allows the experimenter to focus only on the muscle control problem. Once adequate control schemes are advanced for these idealized boundary conditions, one may then move to more complex environmental muscle conditions.

The muscle testing system presented provides a versatile platform for generalized muscle testing experiments, in open-loop stimulation as well as closed-loop stimulation modes. Additional system functionality may be added with minimal software development (primarily the development of the associated SIMULINK block and adding relevant GUI controls). The flexibility of the system stems from its capacity to implement simulated boundary conditions on the tested muscles, coupled with its capacity to modulate electrical stimulus parameters in real-time based on a computed control output. In future studies on muscle behavior, we anticipate this platform will support a wide variety of muscle control and identification investigations.

Chapter 3

Identification of Muscle Dynamics

In this chapter I develop models that describe the dynamics of electrically stimulated muscle undergoing periodic mechanical oscillations. The objective is to identify models that are simple in their structure, therefore enabling mathematical tractability, while capturing the essential features of a muscle's response. The objective is not to arrive at a comprehensive model for muscles that captures all facets of their response.

It is well known that the force generated by a muscle is a function of many factors, including its length, contraction velocity, activation levels, chemical state, fatigue state and time history [74, 56]. At a first glance, this makes the modeling task formidable. However, by restricting the models investigated to certain classes, and by limiting their scope, simplifications arise.

This chapter proceeds as follows. First, the utilization of a Wiener model structure is motivated. This structure consists of an LTI system representing activation dynamics in cascade with an algebraic nonlinearity that represents the dependence of a muscle's force on its mechanical state. Then, via successive approximations, a multi-affine structure for this nonlinearity is motivated. We describe a set of experiments that enable fitting of parameters for this structure via least squares regression, and present the experimental data. Based on the data, three questions are tackled:

1. What is the efficacy of multi-linear models in capturing essential features of a muscle's mechanical response for oscillatory motions?
2. What terms of the model should be retained, and what terms can be discarded without significant loss of model performance?
3. Based on experimental data, what are appropriate model parameters, and what is their variance?

Scope We focus on the force response of a muscle undergoing periodic oscillatory motions with frequencies in the range of 1 Hz to 7 Hz and amplitudes of 0.5 mm to 2 mm, comprising muscle strains of upto $\pm 20\%$. Additionally, we focus on aggregate behaviors, meaning that we are not interested in isolating canonical features of a muscle response, such as the force-length, force-velocity or history dependent effects. Rather, we are interested in the net effect of the interaction of all of those features simultaneously.

Summary of findings Based on experimentation, our results indicate that bilinear models in the form of $F = A + Bx + C\alpha + Dx\alpha$ have a performance that is virtually indistin-

guishable from a multi-affine model in the form of $F = A + Bx + C\alpha + Dx\alpha + E\dot{x} + G\dot{x}\alpha + Hx\dot{x} + Ix\dot{x}\alpha$, where x is the muscle displacement, $\dot{x}$ is its velocity and α is its activation. Bilinear models capture approximately 64.55% to 80.58% of the variance of the muscles output ($\mu = 73.61\%, \sigma = 5.73\%$). The active terms $C\alpha$ and $Dx\alpha$ were found to contribute most to the variance of the response. The dependence of force on active and passive velocity and visco-elasticity was minimal.

3.1 Motivating the model structure

3.1.1 Hammerstien-Wiener model structures

Hammerstein-Weiner cascades have been proposed, and to a large degree successful, in modeling muscle dynamics [40, 58, 62, 19]. The cascade is shown in figure 3-1. The inputs to the model are the electrical stimulus signal $u(t)$, the muscle length $x(t)$ and velocity $\dot{x}(t)$. The output $F(t)$ is the force produced by the muscle. The variables $v(t)$ and $\alpha(t)$ are intermediate variables, where $\alpha(t)$ represents the muscle activation and $v(t)$ represents the stimulus transformed by the input nonlinearity. The cascade consists of an algebraic nonlinear function $f(u)$, followed by a linear dynamical system $G(s)$ (where s is the Laplace variable) followed by another algebraic nonlinear function $h(\alpha, x, \dot{x})$. In the context of muscles $f(u)$ typically describes the recruitment properties of muscles, $G(s)$ represents the dynamics of calcium transport between the sarcoplasmic reticulum and the sarcoplasm, and $h(\alpha, x, \dot{x})$ represent the modulation of force due to the force-length and force-velocity characteristics of the muscle, which can be traced back to the sliding filament theory and the cross-bridge hypothesis of muscle contraction [74, 56].

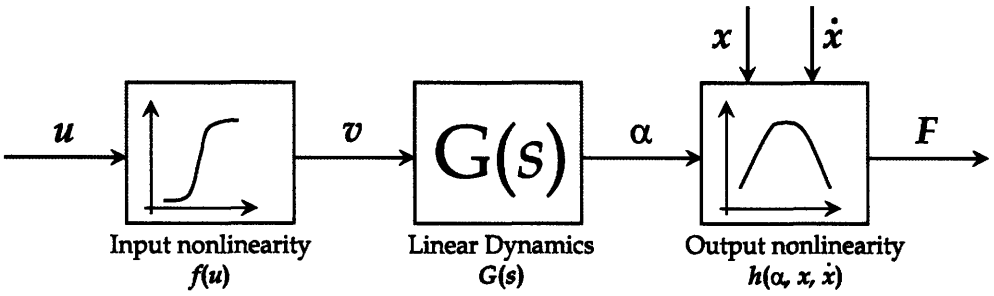

Figure 3-1: Hammerstien-Wiener model cascade consisting of a static nonlinearity $f(u)$, followed by a linear dynamical system $G(s)$, followed by another static nonlinearity $h(\alpha, x, \dot{x})$.

This model structure is further simplified in the following ways:

- **Ignore the recruitment characteristics** $f(u)$. Maximizing the power output delivered to the load via optimal control leads to bang-bang control trajectories, meaning that the control input assumes only two values, either u_{min} or u_{max} (see section 4)[1]. Therefore, intermediate values do not matter, and the shape of the function $f(u)$ will not be of concern. Thus we may eliminate this function with a linear counterpart that passes through the points $[u_{min}, v_{min}]$ and $[u_{max}, v_{max}]$. This linear gain may then be easily incorporated, without loss of generality, to any of the other two blocks.

[1] Assuming the optimization does not include any penalty on the command u.

- **Simplify the dynamics of $G(s)$.** First, we ignore any time delays since we are working with open loop control. The temporal shifting of the output of $\alpha(t)$ due to the delay will have no effect on the muscle's power. Second, calcium diffusion dynamics are assumed to bear the response of a second order system with real poles. This is a plausible model since the underlying process is a diffusion process. Thus, $G(s)$ is written as:

$$G(s) = \frac{p_u}{(s + p_\beta)(s + p_\alpha)} \tag{3.1}$$

- **Assume a multi-affine approximation to $h(\alpha, x, \dot{x})$.** This will be discussed in detail in the next section.

These simplifications result in the model structure shown in figure 3-2.

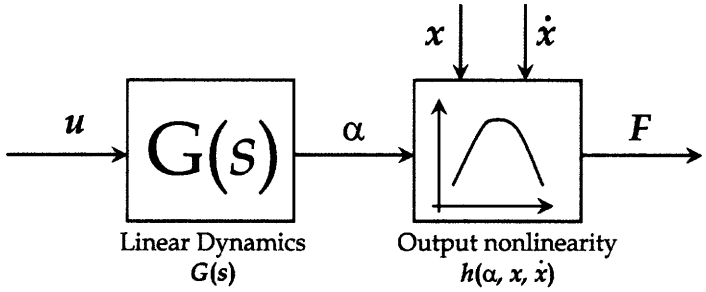

Figure 3-2: Wiener model cascade of a linear dynamics block followed by a static nonlinearity.

3.1.2 Multilinear models for $h(\alpha, x, \dot{x})$

Consider the output nonlinear function:

$$F(t) = h\left(x(t), \dot{x}(t), \alpha(t)\right)$$

The following analysis is based largely on [39]. Assuming differentiability, we take a Taylor series expansion of $h(\cdot)$ about some operating point $(x_0, \dot{x}_0, \alpha_0)$.

$$\begin{aligned} h\left(x, \dot{x}, \alpha\right) = \; & h(x_o, \dot{x}_o, \alpha_o) + (x - x_o)\left.\frac{\partial h}{\partial x}\right|_{x=x_0} + (\alpha - \alpha_0)\left.\frac{\partial h}{\partial \alpha}\right|_{\alpha=\alpha_0} \\ & + (\dot{x} - \dot{x}_0)\left.\frac{\partial h}{\partial \dot{x}}\right|_{\dot{x}=\dot{x}_0} + (x - x_o)(\dot{x} - \dot{x}_0)\left.\frac{\partial^2 h}{\partial x \partial \dot{x}}\right|_{x=x_0, \dot{x}=\dot{x}_0} \\ & + (x - x_o)(\alpha - \alpha_0)\left.\frac{\partial^2 h}{\partial x \partial \alpha}\right|_{x=x_0, \alpha=\alpha_0} + (\alpha - \alpha_0)(\dot{x} - \dot{x}_0)\left.\frac{\partial^2 h}{\partial \alpha \partial \dot{x}}\right|_{\dot{x}=\dot{x}_0, \alpha=\alpha_0} \\ & + (x - x_o)(\alpha - \alpha_0)(\dot{x} - \dot{x}_0)\left.\frac{\partial^3 h}{\partial \alpha \partial \dot{x} \partial x}\right|_{x=x_0, \dot{x}=\dot{x}_0, \alpha=\alpha_0} + \quad \text{Higher-order terms} \end{aligned}$$

By neglecting the higher order terms (H.O.T.) of the Taylor series and collecting similar terms, one obtains an approximation in the form of

$$F(t) \approx A + Bx + C\alpha + Dx\alpha + E\dot{x} + G\dot{x}\alpha + Hx\dot{x} + Ix\dot{x}\alpha \tag{3.2}$$

What are the physical interpretations of each of the terms in this approximation? The A term represents the residual force in the muscle about the linearization point. In the context of the experiments of this chapter, this point is at $\alpha_0 = 0$, $\dot{x} = 0$, and $x = l_o$, which is a nominal estimate of the resting length of the muscle in the frog. This residual force is subtracted out from any force measurements, and therefore the value of A is equal to zero. The Bx and $E\dot{x}$ represent linear approximations to the muscles' passive elasticity and damping respectively. The $C\alpha$ term represents a linearization of the muscles' dependence on activation. The $Dx\alpha$ and $G\dot{x}\alpha$ terms are important terms that capture the dependence of a muscles stiffness and damping on activation. Figure 3-3 shows schematics of the force-strain and force-strain rate curves of a muscle at different activation levels. At the operating point $(x_0, \dot{x}_0)$, the slopes of those curves vary as a function of activation. This variation of the slope is thus captured in the model. Finally, the $Hx\dot{x}$ and $Ix\dot{x}\alpha$ terms are a natural extension that capture the passive and active visco-elastic effects as well. These terms may be considered generalizations of the bilinear models proposed in [37].

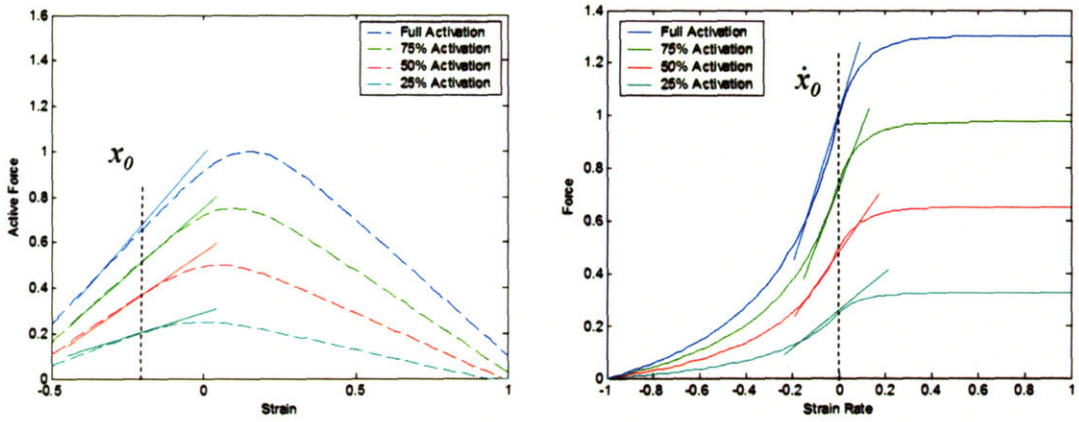

(a) Active force-strain curves.

(b) Active force-strain rate curves.

Figure 3-3: At the operating point, the muscle stiffness and damping are dependent on its activation level. This is evident from the slopes that increase in magnitude with activation.

In summary the model structure for muscle contraction is given by:

$$\alpha(s) = \left\{ \frac{p_\alpha p_\beta}{(s + p_\alpha)(s + p_\beta)} \right\} U(s) \tag{3.3}$$

$$F = A + Bx + C\alpha + Dx\alpha + E\dot{x} + G\dot{x}\alpha + Hx\dot{x} + Ix\dot{x}\alpha \tag{3.4}$$

where $\alpha(s)$ and $U(s)$ are the Laplace transforms of $\alpha(t)$ and $u(t)$ respectively.

For the rest of this chapter, I focus on the multi-linear model of equation 3.4, and take it as a departure point for experimentation and parameter identification. Equation 3.3 is not used in the identification scheme, but rather more direct estimates of α are used (as described in the next section). Equation 3.3 is only used as a basis model to derive the

optimal control in chapter 4 when an analytical formulation of the activation dynamics is required.

3.2 Experimental approach

The goal for this section is to estimate the parameters A through I of equation 3.4. Those parameters are determined experimentally using direct measurements of $x(t)$, $\dot{x}(t)$, $F(t)$ and estimates of $\alpha(t)$. Recall that direct measurements of the muscle activation $\alpha(t)$ are not accessible experimentally.

Since the purpose of the experiments is to determine the efficacy of the model under periodic workloop oscillations, it may be tempting to use the data generated from such experiments to estimate those parameters directly. This, however, is not feasible. Figure 3-4 shows a typical plot of the system trajectories for a mass-spring-damper load excited by an antagonist muscle pair. Each muscle is stimulated, with the stimulus triggered at a given frequency, and both muscles stimulated out of phase (180^o phase). Owing to the dynamics of the combined muscles-load system, the time trajectory of the solutions converges to a limit cycle, with the the stimulation points being phase-entrained with the limit cycle. Thus, the stimulation points become clustered around a narrow region of the force-velocity space.

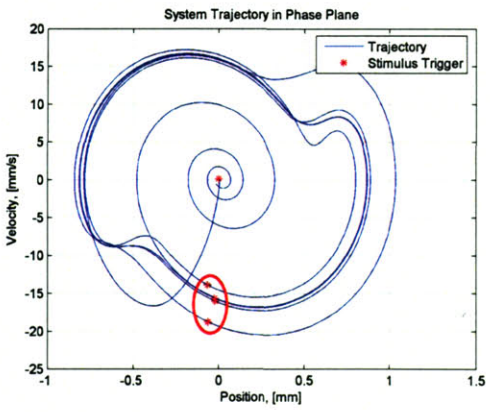

(a) Trajectory in the force-velocity space

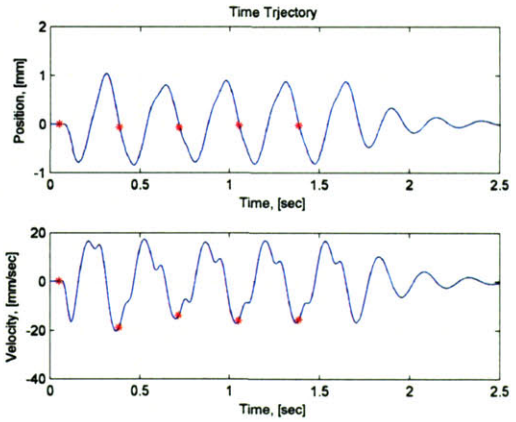

(b) Time domain plots of position and velocity. Red asterisks indicate trigger points.

Figure 3-4: Trajectory of the muscle undergoing periodic oscillations. Note that, with the exception of the first trigger point, all remaining triggers are confined to a very small region of the position-velocity space indicated by the red ellipse.

Clearly, the restriction of stimulation to a narrow range of the force-velocity space diminishes the informativity of the data. To get a model that spans a wider region of the position-velocity space, it is desirable to scatter those stimulation points more uniformly. To achieve this, the muscle is subjected to sinusoidal oscillations by programming the apparatus to act as a high impedance motion source. The sinusoids trace ellipsoids in the position-velocity plane. At different points that are temporally equidistant on the ellipsoid, the muscle stimulus is triggered as shown in figure 3-5(a). Consequently a contractile force is generated. This force, coupled with the position and velocity signals, is used to fit the multi-linear model parameters. The procedure is repeated for different oscillation amplitudes and frequencies, thereby spanning a wider region in the position-velocity combinations.

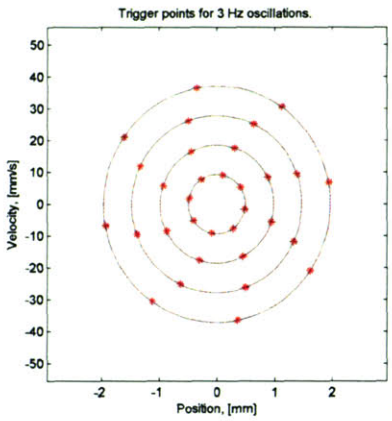

(a) Location of stimulus points at different harmonics.

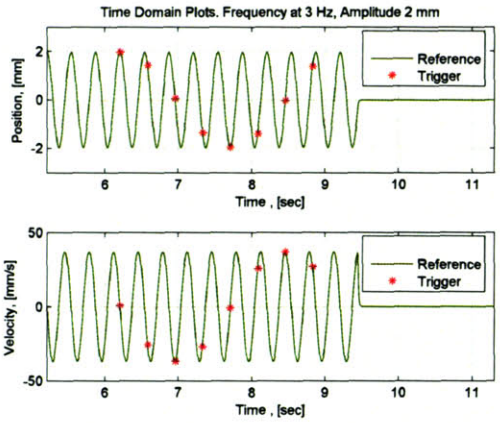

(b) Time domain plots for reference trajectories (shown only for the outer most ring.

Figure 3-5: Distribution of stimulus trigger points in the position-velocity space.

This experimental procedure gives us direct measurements of $x(t)$, $\dot{x}(t)$, and $F(t)$. But what about $\alpha(t)$? One approach is to model the dynamics of $G(s)$ of figure 3-1 (perhaps using the model of equation 3.3) and use this model to estimate $\alpha(t)$. Instead, we use the following procedure. Noting that $\alpha(t)$ is the muscle activation, and noting that it is inaccessible experimentally, and assume that the profile of the force generated under isometric conditions is an indication of the activation level of the muscle. Therefore, at the beginning of each set of measurements, a pre-twitch is measured isometrically. One such pre-twitch has the profile showin in figure 3-6(a). This profile is then normalized and convolved with the trigger pulse signals, to produce an estimate of the activation trace shown in figure 3-6(b). This gives us an estimate of $\alpha(t)$.

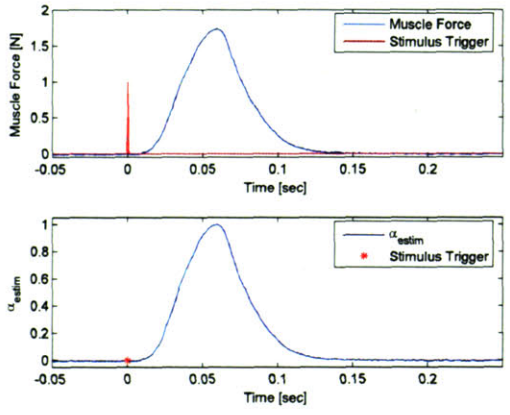

(a) The profile of a single twitch force is normalized to create an estimate of $\alpha(t)$.

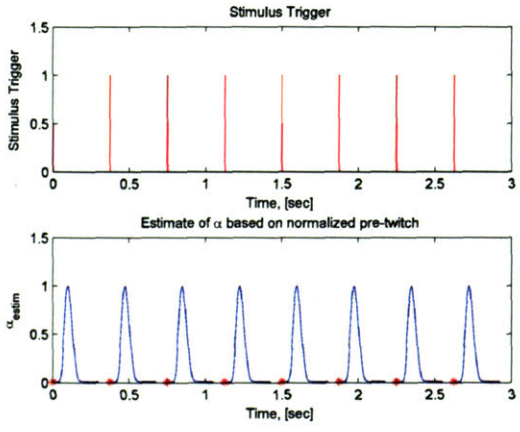

(b) $\alpha(t)$ is estimated by convolving the normalized twitch profile with trigger impulses.

Figure 3-6: Estimating $\alpha(t)$

Two points are worth noting regarding this experimental design:

- This method avoids the explicit modeling and estimation of $G(s)$, and therefore focuses on $h(\alpha, x, x)$. This is advantageous since modeling errors of $G(s)$ will not contaminate estimates of the parameters of $h(\alpha, x, x)$.
- In some cases it may be possible to use boot-strapping methods to estimate the parameters of both $G(s)$ and $h(\alpha, x, x)$ simultaneously. One such procedure is outlined in [27].

3.2.1 Parameter estimation via least-squares regression

Parameter estimates are obtained in a straightforward manner via least-squares regression. At each time instance t_i, we assume that the muscle force is generated according to

$$F_i = A + Bx_i + C\alpha_i + Dx_i\alpha_i + E\dot{x}_i + G\dot{x}_i\alpha_i + Hx_i\dot{x}_i + Ix_i\dot{x}_i\alpha_i$$

where the subscript denotes the value of the quantity at time index i. Writing the equations in matrix form for all values of $i \in [1, N]$

$$\begin{Bmatrix} F_1 \\ \vdots \\ F_i \\ \vdots \\ F_N \end{Bmatrix} = \begin{bmatrix} 1 & x_1 & \alpha_1 & x_i\alpha_1 & \dot{x}_1 & \dot{x}_1\alpha_1 & x_1\dot{x}_1 & x_1\dot{x}_1\alpha_1 \\ \vdots & \vdots & \vdots & \vdots & \vdots & \vdots & \vdots & \vdots \\ 1 & x_i & \alpha_i & x_i\alpha_i & \dot{x}_i & \dot{x}_i\alpha_i & x_i\dot{x}_i & x_i\dot{x}_i\alpha_i \\ \vdots & \vdots & \vdots & \vdots & \vdots & \vdots & \vdots & \vdots \\ 1 & x_N & \alpha_N & x_N\alpha_N & \dot{x}_N & \dot{x}_N\alpha_N & x_N\dot{x}_N & x_N\dot{x}_N\alpha_N \end{bmatrix} \begin{Bmatrix} A \\ B \\ C \\ D \\ E \\ G \\ H \\ I \end{Bmatrix}$$

or

$$\mathbf{F} = \mathbf{M}\boldsymbol{\Theta} \tag{3.5}$$

Standard least squares regression yields the optimal $\boldsymbol{\Theta}^*$.

$$\boldsymbol{\Theta}^* = \left(\mathbf{M}^\mathbf{T}\mathbf{M}\right)^{-1}\mathbf{M}^\mathbf{T}\mathbf{F} \tag{3.6}$$

It is important to note that the columns of the matrix $\mathbf{M}$ are not necessarily orthogonal given the experimental procedure outlined. This has consequences that will play a role when determining which of the model terms are significant and which are not. The first consequence is that the values of the parameters $\boldsymbol{\Theta}^*$ will depend on which columns of the regressors matrix $\mathbf{M}$ are included in the regression. For example, if we choose to include only the first four columns of the matrix $\mathbf{M}$ in the regression (dropping out all velocity terms), the values of the parameters A through D will not necessarily be the same as those obtained when the entire $\mathbf{M}$ matrix is used. This is not the case with orthogonal regressors. The second consequence is that the variance of the vector $\mathbf{F}$ is *not* equal to the sum of variances of the individual terms $(A, Bx, C\alpha, \cdots, Ix\dot{x}\alpha)$.

3.3 Experimental Protocol

The experiments described for the rest of this chapter are all conducted using the test apparatus and methods reported in chapter 2. Briefly described, *plantarus longus* muscles are

harvested from leopard frogs (*Rana pipiens*). The muscle is placed in a bath of amphibian Ringer's solution. The relative motion of both ends of the muscle is controlled using a servo system that imposes the sinusoidal motions at specified frequencies and amplitudes. Electrical stimulation is delivered through the sciatic nerve, which is left connected to the muscle during the dissection phase. Every time the electrical stimulus is triggered, a 200 Hz pulse train is delivered for a period of 5 ms (10 pulses), with each pulse having a duration of 100 μs. The amplitude of the pulses is usually between 10 to 15 volts. While the motions and stimulations are imposed on the muscles, the contractile muscle force is measured via an in-series force transducer.

Experiments were conducted on seven muscle specimens. For each muscle, measurements were taken for a variety of oscillation frequencies and amplitudes. Table 3.1 summarizes the different conditions under which measurements were taken. Muscles 1 and 2 were both left and right *plantaris longus* muscles (respectively) harvested from the same frog. Likewise for muscle pair 3 and 4 and muscle pair 5 and 6.

Frequency Hz	Amplitude mm	Muscle 1	Muscle 2	Muscle 3	Muscle 4	Muscle 5	Muscle 6	Muscle 10
1	2.0	*	*	*	*			
	1.5	*	*	*	*			
	1.0	*	*	*	*			
	0.5	*	*	*	*			
2	2.0	*	*	*	*			*
	1.5	*	*	*	*			*
	1.0	*	*	*	*			*
	0.5	*	*	*	*			*
3	2.0	*	*	*	*			*
	1.5	*	*	*	*			*
	1.0	*	*	*	*			*
	0.5	*	*	*	*			*
4	2.0			*	*			*
	1.5			*	*			*
	1.0			*	*			*
	0.5			*	*			*
5	2.0					*	*	*
	1.5					*	*	*
	1.0					*	*	*
	0.5					*	*	*
6	2.0					*	*	
	1.5					*	*	
	1.0					*	*	
	0.5					*	*	
7	2.0					*	*	
	1.5					*	*	
	1.0					*	*	
	0.5					*	*	

Table 3.1: Summary of experimental conditions. Measured data are indicated by an asterisk.

3.4 Experimental results

The data is presented in the following sequence. First, a detailed description of one data set (one particular muscle at one particular frequency and amplitude) is presented. Then data

sets at all frequencies and amplitudes for one particular muscle are combined in a single model. Finally, we look at all the muscle responses in combination.

3.4.1 One data set: A detailed look

Figure 3-7 shows one data set from measuring the response of muscle 1 subjected to 2 mm oscillations at 3 Hz, which is a typical data set. Notice that the trigger points span a wide range of the position-velocity space. Also notice that there is clear modulation of the force levels produced by the muscle as a function of the different position and velocity combinations.

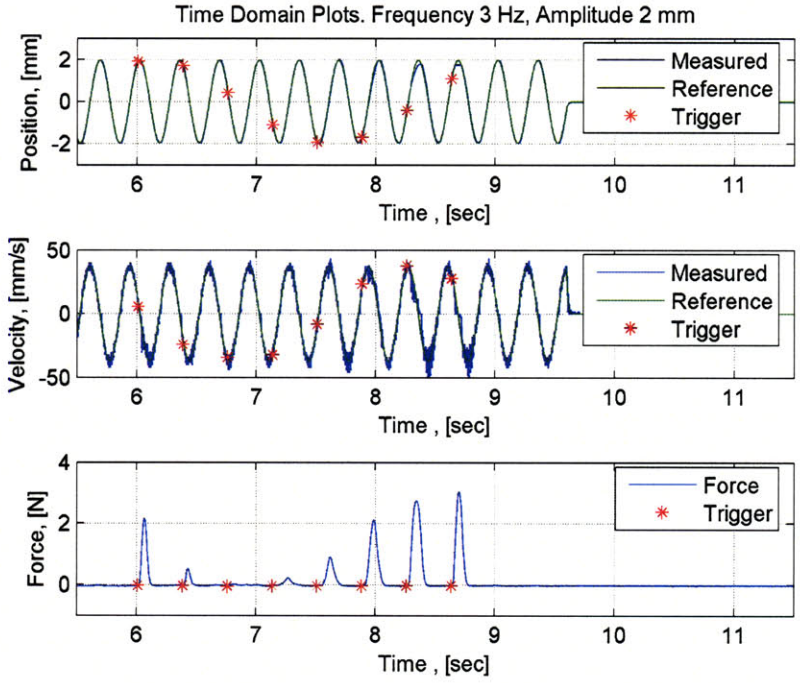

Figure 3-7: Sample data set of multi-linear model identification for oscillations with 2 mm amplitude at 3 Hz. Plots from top to bottom are position, velocity and force. In all plots, blue lines indicate actual measurements, green lines indicate reference trajectories, and red asterisks indicate trigger points.

Figure 3-8(a) shows the exact same data of figure 3-7, but plotted in position-velocity-force coordinates. Plotting the data this way reveals a structure – the data lines are all contained in a wedge shaped volume. While the muscle is triggered all around the harmonic ring in the position-velocity plane, clearly the force is pronounced in only part of the space. This structure was found to be consistent across all data sets and all muscles measured.

Fitting the multi-affine model of equation 3.4 gives the plot shown in figure 3-8(b). There are two surfaces that show the estimated force developed by the muscle according to the multi-linear approximation for maximal activation ($\alpha = 1$) and zero activation ($\alpha = 0$).

Two observations are made:

- The surfaces are surprisingly planar even though the model structure allows for curvature. This indicates that the effect of cross-coupling terms between position and

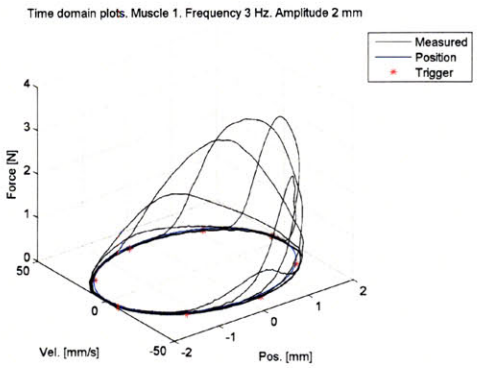

(a) Data set of figure 3-7 shown in a position-velocity-force space.

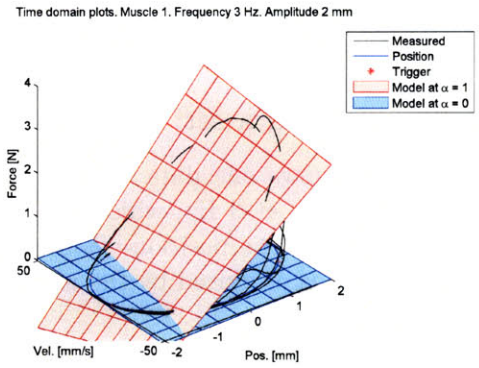

(b) Data set of figure 3-8(a) shown with multi-linear fit planes evaluated at full activation ($\alpha = 1$) and zero activation ($\alpha = 0$).)

Figure 3-8: Sample data set of multi-linear model identification for oscillations with 2 mm amplitude at 3 Hz.

velocity are minimal (i.e. the viscoelastic $Hx\dot{x}$ and $Ix\dot{x}\alpha$ terms). Otherwise some curvature of the surfaces would have been apparent.

- The plane corresponding to full activation (red plane) exhibits a larger slope in the direction of x that the direction of $\dot{x}$. This indicates that the dependence of the force on position out-weighs the dependence on velocity.

The significance of individual model terms

To make an assessment of the significance of individual terms of the model, we use the "variance accounted for" metric [51], which is defined as

$$VAF(\text{Model}) = \left(1 - \frac{Var(F_{meas} - F_{model})}{Var(F_{meas})}\right) \times 100 \tag{3.7}$$

where $Var(\cdot)$ is the variance. Essentially this measures how much of the measured data variance is captured by the model. For an unbiased estimator, the value of VAF ranges between 0% and 100%.

There are two ways to investigate the effect of the multi-affine model parameters using this metric:

1. Apply-least squares regression using only the parameters considered one-at-a-time. For example, if we are to investigate the effect of the active damping term ($G\alpha\dot{x}$) term on the results, we would evaluate the VAF metric for $F_{model1} = G\alpha\dot{x}$.

2. Apply least squares regression using all but the parameters considered. Continuing with the example, we would evaluate the VAF metric for $F_{model2} = A + Bx + C\alpha + Dx\alpha + E\dot{x} + Hx\dot{x} + Ix\dot{x}\alpha$.

If the effect of active damping is significant, then then VAF(model 1) would be high, and VAF(model 2) would be low.

Why do we need those two computations? In least squares regression, if the columns of the matrix $\mathbf{M}$ in equation 3.6 are orthogonal, then methods 1 and 2 above would yield complementary information, i.e. $VAF(\text{model 1}) + VAF(\text{model 2}) = 100\%$. However, since the matrix $\mathbf{M}$ columns are not orthogonal, then the VAFs would not necessarily sum up to 100%. Figures 3-9 shows the values of those indicators applied to all model elements for the data set of figure 3-8(a).

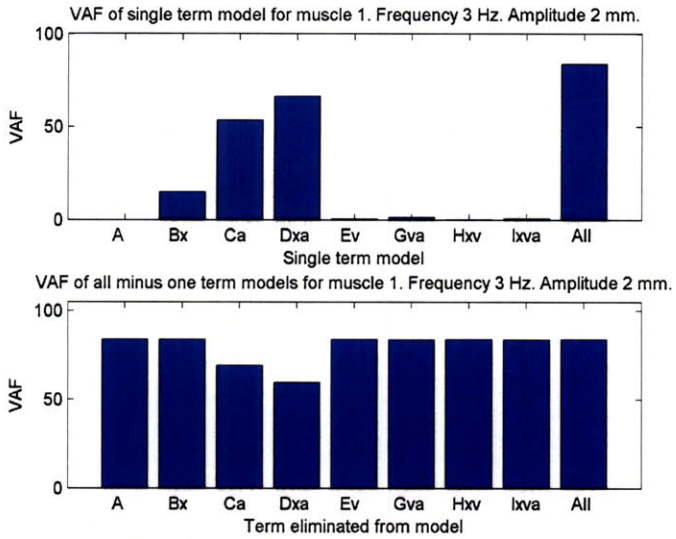

Figure 3-9: Relative contribution of all the terms in the multi-linear models for data set 1 of muscle 1. Contributions are quantified according the the "variance accounted for" metric. Notice that the $C\alpha$ and $Dx\alpha$ terms dominate. The Bx term has a smaller contribution. All other terms are negligible. This trend is observed in most other data sets.

The top bar chart indicates that a multi-affine model is capable of capturing 83.97% of the variance of the data. Furthermore, the elimination of the $E\dot{x}, G\dot{x}\alpha, Hx\dot{x}, Ix\dot{x}\alpha$ will provide minimal impact. A bilinear models consisting only of the terms A, Bx, $C\alpha$ and $Dx\alpha$ is capable of capturing 83.68% of the variance of the data.

3.4.2 One muscle: A detailed look

Now that one data set is analyze in detail, the results are reproduced for oscillations at different amplitudes and frequencies. Each of the plots of figures 3-8(a), 3-8(b) and 3-9 are reproduced for a range of frequencies and amplitudes, and are shown in figures 3-10, 3-11 and 3-12. The following observations are made:

- From figure 3-10, all data sets exhibit similar shape and structure when plotted in the position-velocity-force space, i.e. the curves are all contained in a similar "wedge" shaped volume.

- From figure 3-11, the bilinear model fits are to a large degree very similar (at least by visual inspection). They tend to deviate for the small amplitude oscillations (0.5 mm), possibly because the planes evaluate the model at a larger extrapolation range.

- From figure 3-12, the contributions to all of the terms in the multi-linear model structure are always dominated by the $C\alpha$ and $Dx\alpha$ terms. Also note that the relative contributions of the $C\alpha$ term becomes relatively more significant with decreasing oscillation amplitudes.

- The quality of the fits according to the VAF metric, using all model terms, ranges between 82.2% to 98.4% of the total variance of the experimental data.

- Because the columns of the matrix $\mathbf{M}$ are non-orthogonal, we see that the sum of heights of the bars of the individual terms do not sum to the height of the bar corresponding to all the terms. In fact, it is evident that $VAF(\text{All}) \neq VAF(C\alpha) + VAF(Dx\alpha)$.

- Since the residual forces are subtracted from the experimental force measurements, the value of the A term is always equal to zero.

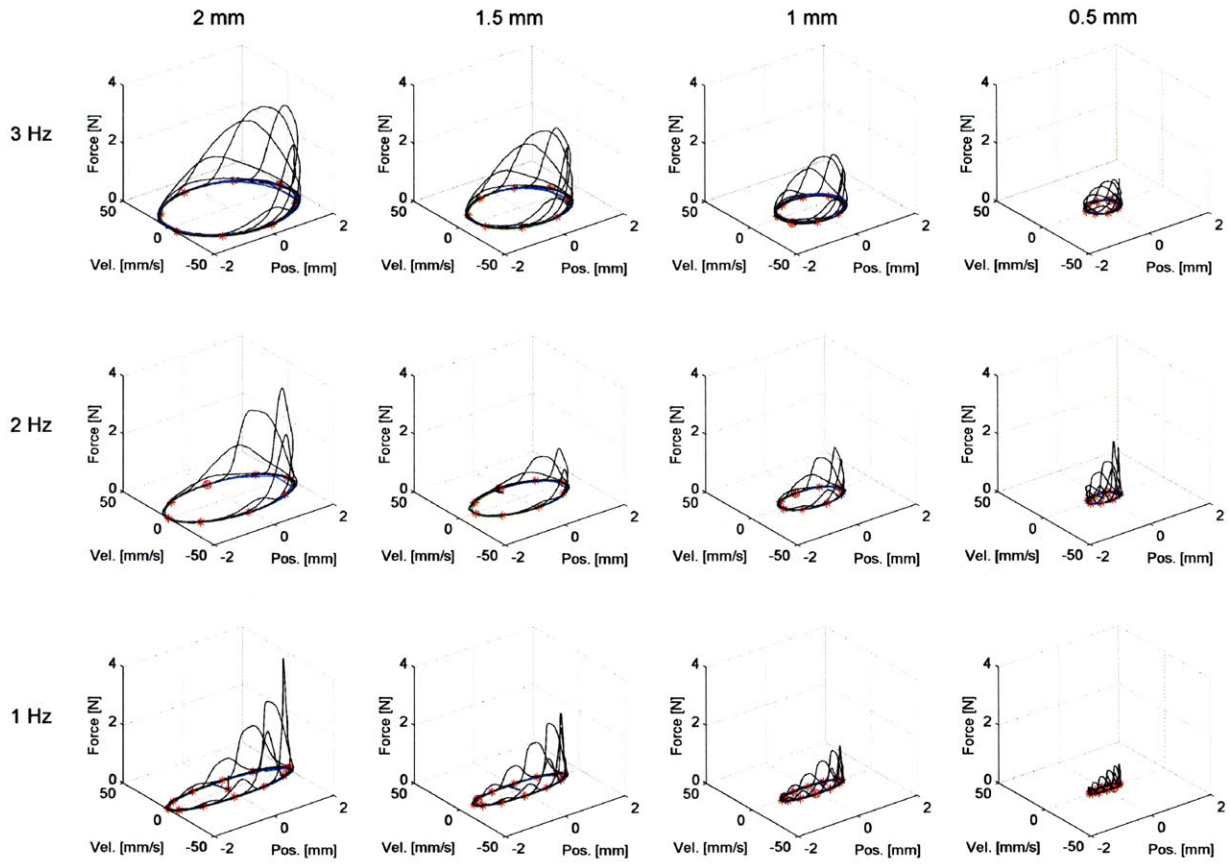

Figure 3-10: Plots of all data sets for muscle 1. The plots are constructed in an identical manner to the plot of figure 3-8(a). The different amplitudes/frequencies of the oscillations label each column/row respectively. All traces are plotted on identical scales, and thus for different velocities, the curves have different aspect ratios.

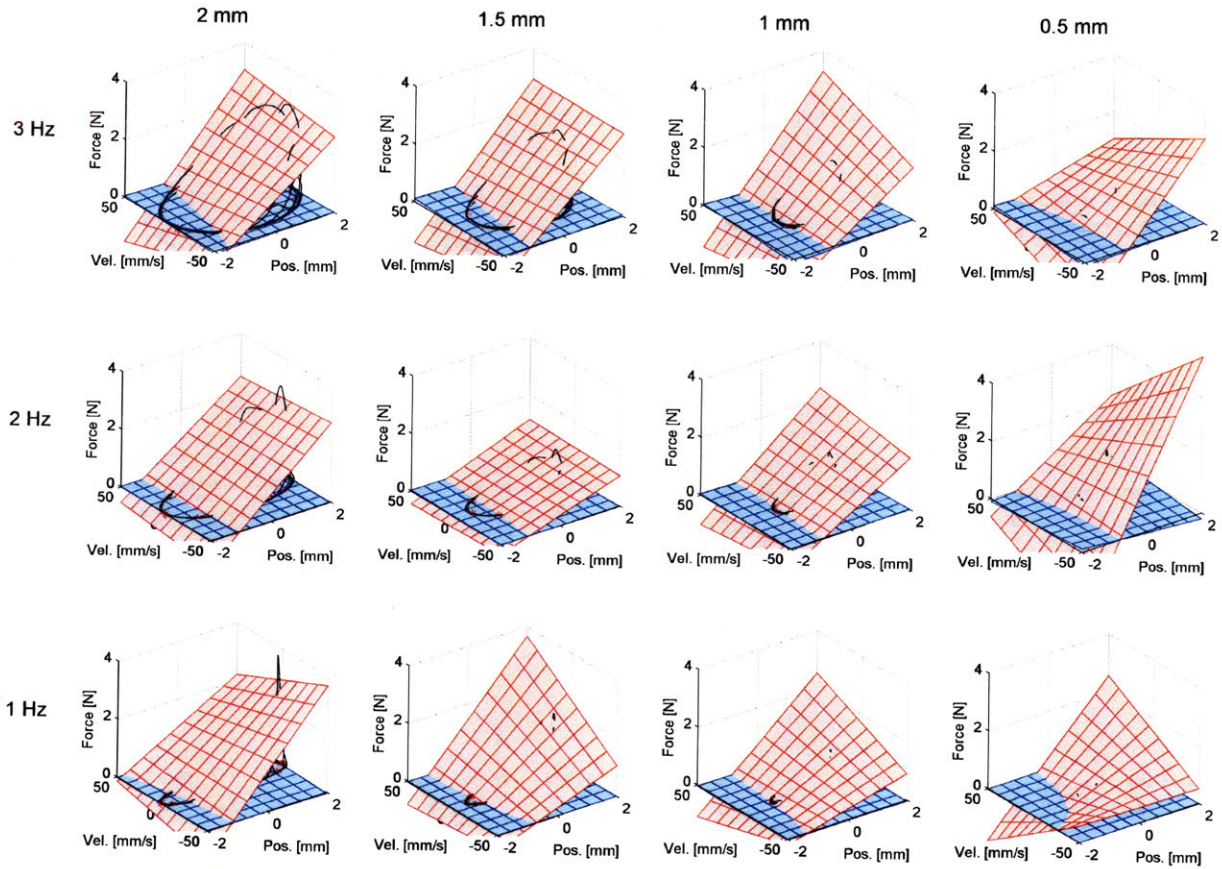

Figure 3-11: Plots of all data sets for muscle 1 with the optimal bilinear fit. The surfaces evaluate the model fit at activations levels $\alpha = 1$ (blue) and $\alpha = 0$ (red). The plots are constructed in an identical manner to the plot of figure 3-8(b). The different amplitudes/frequencies of the oscillations label each column/row respectively. All traces are plotted on identical scales, and thus for different velocities, the curves have different aspect ratios.

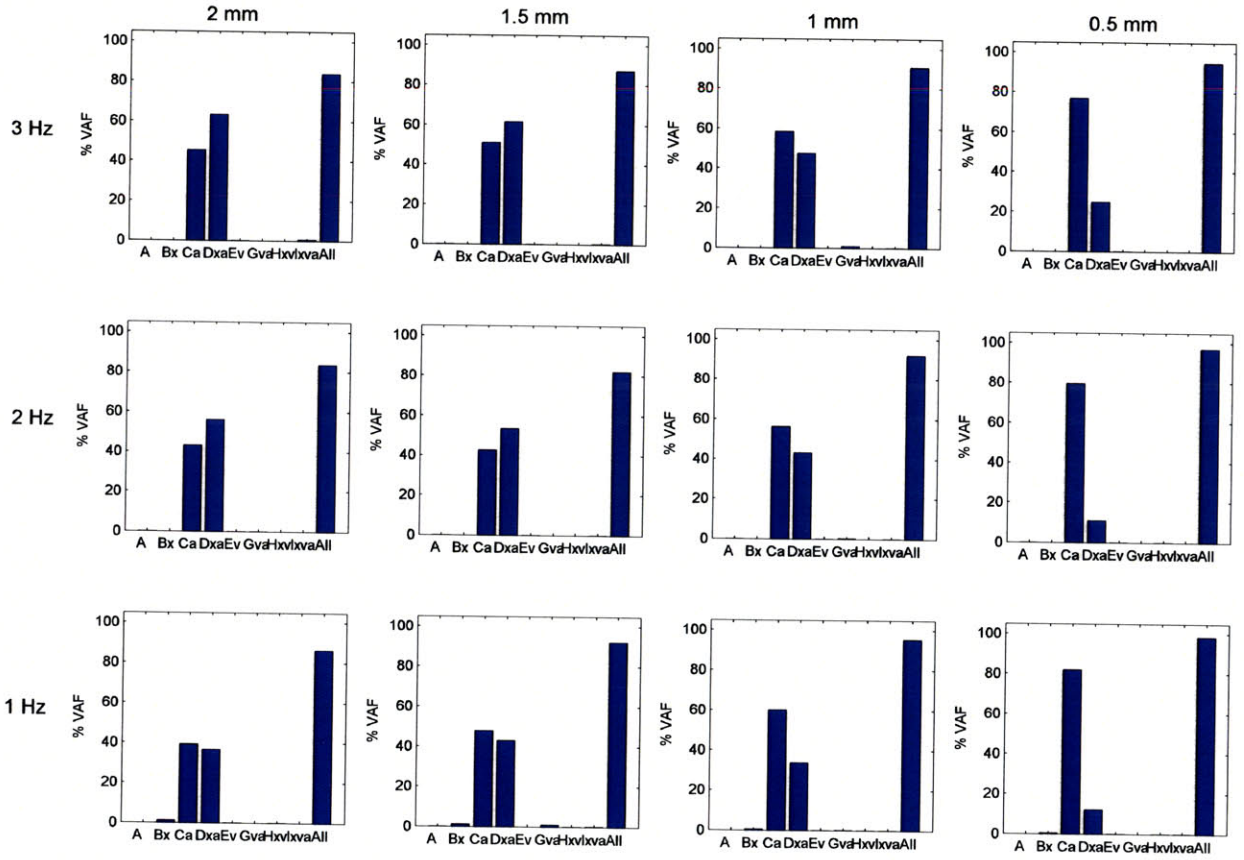

Figure 3-12: Bar charts indicate the relative contribution of each model term to each individual fit. Plots are constructed in an identical manner to the plot of figure 3-9.

3.4.3 Combining data sets for one muscle

The above plots show the data and the model fits for one data set at a time. We would like to obtain a *single model* fit for all data sets for each muscle. Doing so by direct concatenation of all data sets for a particular muscle may be inappropriate since the effect of fatigue penalizes the the amplitude of force measurements taken toward the end of an experimental session (because the muscle forces diminish). Therefore some compensation scheme is required.

One way to compensate for fatigue is to model its effect on the muscle response, and take that into account as a source of force deficit. Alternatively, we choose to use a periodic standardized test that indicates muscle "health". In particular, before each measurement, we obtain an isometric twitch response, and use that response to scale the data.

Individual isometric twitches for one experimental data set are shown in figure 3-13. Much of the decay in force levels is due to fatigue. Therefore, for modeling purposes, we use the peak values as normalizing factors. The lower plot of figure 3-13 shows that the twitch profiles are highly reproducible.

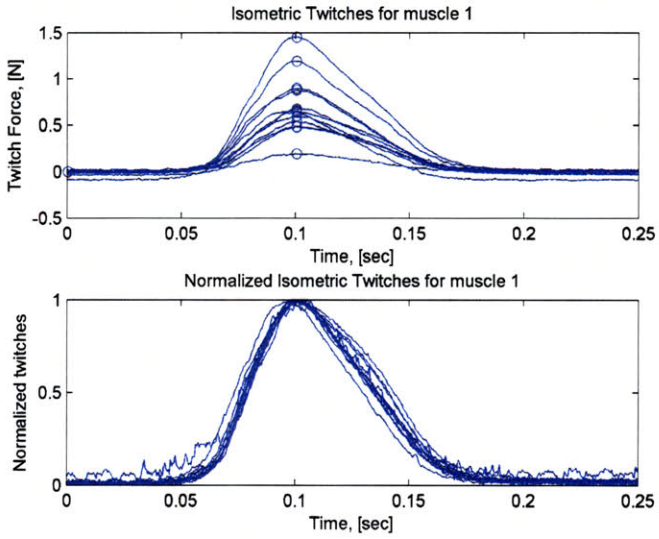

Figure 3-13: Variation of twitch profiles as the muscle fatigues. Peak values for each twitch is used as the normalizing factor.

Figure 3-14 shows all the force traces for all of the measurements taken from muscle 1. Measurements were taken at 1, 2 and 3 Hz oscillation frequencies and amplitudes of 0.5, 1, 1.5 and 2 mm. All the data of figure 3-10 is plotted on the same axes, and one single model is fit to the entire collection.

The efficacy of this one model to reproduce the variance in all the data sets is captured in figure 3-15. Note that the values of the VAF metric are generally lower than in figure 3-12 because one model now fits a much larger data set.

3.4.4 Data sets for different muscles

The experiment above is repeated for a six muscles. The experimental conditions were varied, and are summarized in table 3.1. Combining all the data sets for all frequencies and

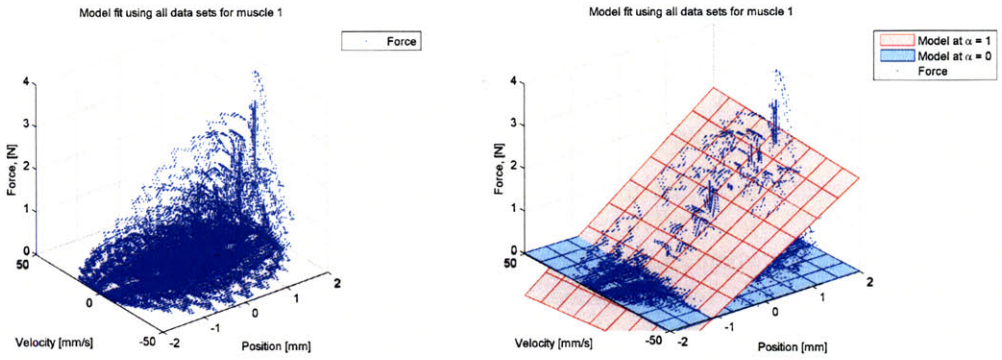

Figure 3-14: Single Bar

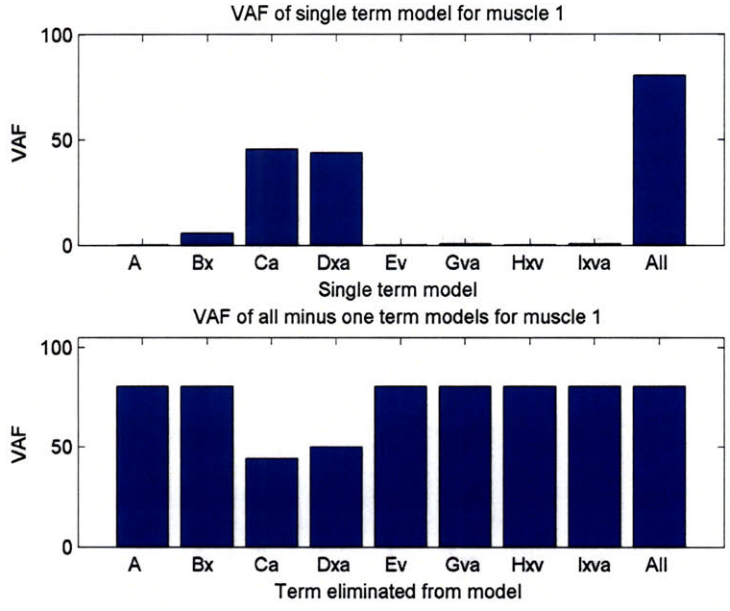

Figure 3-15: Bar chart for all data for muscle 1

amplitudes, the plots of figure 3-16 are obtained.

3.5 Conclusions

To conclude, let us return to the set of original questions posed:

What is the efficacy of multi-linear models in capturing essential features of a muscle's mechanical response for oscillatory motions?

The variance accounted-for metrics for all the experiments yielded correlations between 65.02% to 80.59% ($\mu = 74.21\%, \sigma = 5.56\%$). We assert that this is sufficient for the tests in hand, particularly when viewed in the context of how simple the models are. The essential features of a muscles response have been shown to the active force (the $C\alpha$ term) and activation dependent stiffness (the $Dx\alpha$ term).

What terms of the model should be retained, and what terms can be discarded without significant loss of model performance?

From figures 3-15 and 3-16, the Bx, $C\alpha$ and $Dx\alpha$ terms are by far the most significant terms, accounting for most of the variance contribution of the model. With the bilinear model terms only, the statistics of the VAF metric have been only slightly reduced ($\mu = 73.61\%, \sigma = 5.73\%$, range from 64.55% to 80.58%). This is a reaffirmation of the validity of bilinear muscle models suggested in the literature.

Based on experimental data, what are appropriate model parameters, and what is their variance?

The computed parameters are summarized in the following table 3.2.

Coef.	Muscle 1	Muscle 2	Muscle 3	Muscle 4	Muscle 5	Muscle 6	Muscle 10	Mean	Var
A	-0.0038	0.0006	0.0156	0.0224	0.1468	0.3248	0.0237	0.0757	0.0147
B	0.0024	0.0085	0.0134	0.0187	0.0511	0.1128	0.0008	0.0297	0.0016
C	0.7685	0.8896	1.3946	1.3723	1.4505	2.4826	1.1458	1.3577	0.3145
D	0.7912	0.8284	1.0542	0.8720	0.8618	1.1844	0.7683	0.9086	0.0234
E	0.0003	0.0002	0.0008	0.0001	0.0020	0.0015	0.0013	0.0009	0.0000
F	-0.0002	0.0019	-0.0013	0.0019	0.0056	0.0080	0.0018	0.0025	0.0000
G	-0.0002	0.0001	0.0006	0.0003	0.0013	-0.0003	0.0011	0.0004	0.0000
I	0.0017	0.0008	-0.0047	-0.0053	-0.0050	-0.0062	-0.0085	-0.0039	0.0000

Table 3.2: Coefficients of the multi-linear muscle

To enable meaningful comparisons between different muscles, and accounting for the fact that different muscles have different nominal strengths, some form of normalization is required (larger muscles naturally produce more force than smaller muscles). This is done by normalizing all the coefficients for each muscle by its C coefficient, which is an indication of the nominal strength of the muscle.

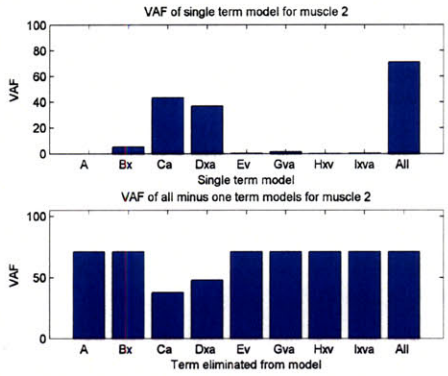

(a) Muscle 2

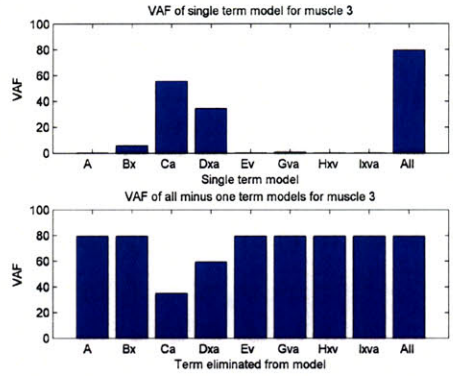

(b) Muscle 3

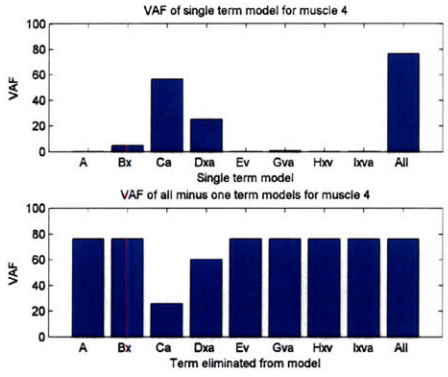

(c) Muscle 4

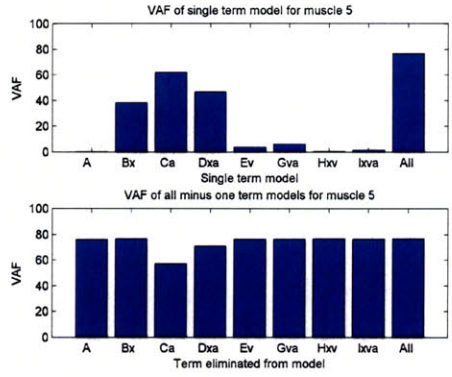

(d) Muscle 5

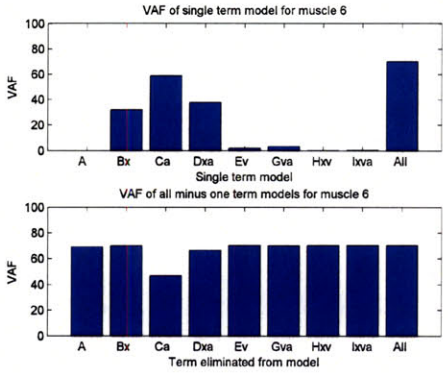

(e) Muscle 6

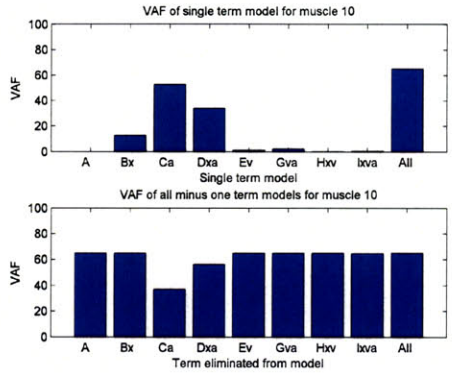

(f) Muscle 10

Figure 3-16: Summary for muscles 2, 3, 4, 5, 6 and 10.

Coefs.	Muscle 1	Muscle 2	Muscle 3	Muscle 4	Muscle 5	Muscle 6	Muscle 10	Mean	Var
A	-0.0049	0.0007	0.0112	0.0163	0.1012	0.1308	0.0207	0.0394	0.0029
B	0.0031	0.0096	0.0096	0.0137	0.0352	0.0455	0.0007	0.0168	0.0003
C	1.0000	1.0000	1.0000	1.0000	1.0000	1.0000	1.0000	1.0000	0.0000
D	1.0296	0.9312	0.7559	0.6355	0.5942	0.4771	0.6706	0.7277	0.0376
E	0.0003	0.0002	0.0006	0.0001	0.0014	0.0006	0.0012	0.0006	0.0000
F	-0.0003	0.0022	-0.0009	0.0014	0.0039	0.0032	0.0015	0.0016	0.0000
G	-0.0002	0.0001	0.0005	0.0002	0.0009	-0.0001	0.0010	0.0003	0.0000
I	0.0023	0.0009	-0.0034	-0.0038	-0.0034	-0.0025	-0.0075	-0.0025	0.0000

Table 3.3: Normalized coefficients of multi-linear model

Why is there minimal dependence on velocity?

An interesting finding of this chapter is that, under the given testing conditions, the response of the muscles can be described with essentially no dependence of muscle force on the velocity of contraction. This is indeed a surprising finding given that muscle force-velocity characteristics are among the most important and well studied properties in muscle physiology. Why is there such an apparent discrepancy?

One potential avenue for reconciliation is to consider the force-velocity relationships at sub-maximal levels. Such data is relatively rare in the muscle physiology literature, and experimental protocols vary making comparisons difficult. However, results reported in [29] indicate that at low activation levels, the force-velocity curve tends to assume a more symmetrical shape. This symmetry has also been predicted by the moment-distribution model [76, 54]. A first-order (linear) approximation of any symmetric (even) function yields a constant value, i.e. with no dependence on velocity. The model proposed in this chapter (equation 3.4) is essentially linear velocity. The activation levels in the experimental protocol, while variable in nature, average out to low activation levels. Therefore, the combination of the model and experimental protocol may collude to give this apparent independence.

Chapter 4

Optimization of Muscle Workloop Energetics

In this chapter I tackle the problem of maximizing the power transfer from muscle actuators to a passive load. More specifically the problem of maximizing the power generated by an antagonist muscle pair against a second-order mechanical load is considered. Three different methods of analyzing the problem are presented, each having its own merits:

1. Basic analysis By making simplifying assumptions regarding the problem setup and the nature of the solutions, we arrive at a mechanistic, intuitive explanation that yields interesting insights to the problem at hand. The results of this analysis motivate a more formal study of the role of muscle stiffness and co-activation on the energetic output of an antagonist pair.

2. Direct simulation One straightforward approach to maximize the power delivered to the load without the need to make additional simplifying assumptions is to systematically search over a wide family of inputs. By direct simulation and computation of the power outputs we obtain estimates of the work done by the muscles, and the conditions under which it is maximized.

3. Optimal control The third approach is tackle the optimization more formally in an optimal control framework. First order necessary conditions for optimality are derived which take the form of a two-point boundary value problem. Methods to solve the two-point boundary value problem are developed. This tool is then used to understand the role of co-activation and muscle impedance on the workloop energetics of the system.

This chapter is organized as follows. First, I set set up the problem, write the equations that model the muscle, and derive the equations of motion of the muscle actuated system. Then I present the analysis, optimization results and discussion for each of the three approaches aforementioned.

4.1 Problem Setup

The most general problem setup is that of a multi-port mechanical load acted upon by an arbitrary number of muscles with arbitrary interconnections. The problem considered here instead is one of the simplest instances, and is depicted in figure 4-1. A pair of identical,

antagonist muscles act upon a common second-order mechanical load. The electrical stimulation inputs to the muscles are $u_1(t)$ and $u_2(t)$ (or the vector $\mathbf{u} = [u_1, u_2]^T$). The muscle responds by producing contractile forces $F_1(t)$ and $F_2(t)$. This is the simplest model where muscle co-activation may play an important role in stiffness modulation (and consequently power transfer), yet it is general enough to model single degree-of-freedom joints acted upon by mono-articular muscles.

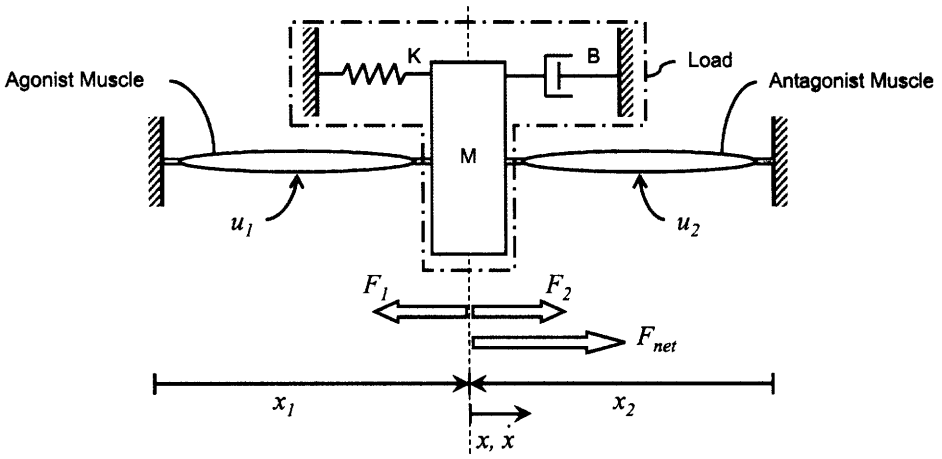

Figure 4-1: Antagonist muscle pair acting against a second order mechanical load.

The problem statement becomes: given a description of the load, and given a model of muscle contraction, find control input trajectories $u_1(t)$ and $u_2(t)$ such that the steady state power transferred from the muscles to the load is maximized under periodic oscillations.

4.1.1 System Model

To model the system, the factors are considered: i) the excitation-contraction dynamics of the muscles, ii) the dependence of force on mechanical state, and iii) the dynamics of the load. The muscle models are based on the discussion of chapter 3.

Excitation-contraction dynamics We assume the excitation-contraction dynamics are important and cannot be neglected. They are captured by second order processes with real poles that model calcium diffusion dynamics. We assume the model is as follows:

$$\begin{aligned} \frac{\alpha(s)}{U(s)} &= G(s) \\ &= \frac{p_{u_i}}{(s+p_{\beta_i})(s+p_{\alpha_i})} \end{aligned} \quad \overset{\mathcal{L}}{\Longleftrightarrow} \quad \begin{aligned} \dot{\alpha}_i(t) &= p_{\alpha_i}\alpha_i(t) + \beta_i \\ \dot{\beta}_i(t) &= p_{\beta_i}\beta_i(t) + p_{u_i}u_i(t) \end{aligned} \tag{4.1}$$

where α_i is the activation state of the muscle and β_i is an intermediate state of Ca^{2+} diffusion and re-uptake dynamics.

Multi-affine force modulation We assume that the force generated by the muscle is a multi-affine function of its activation α and its mechanical state $[x, \dot{x}]$.

$$F_i = A_i + B_i x_i + C_i \alpha_i + D_i x_i \alpha_i + E_i \dot{x}_i + G_i \dot{x}_i \alpha_i + H_i x_i \dot{x}_i + I_i x_i \dot{x}_i \alpha_i \tag{4.2}$$

While in chapter 3 we concluded that a bilinear model is sufficient, we maintain the generality of the full multi-affine model in the foregoing analysis. In actual experimentation, it is not expected to include all the parameters (A through I), since some terms may be deactivated by setting the appropriate coefficient to zero.

Load dynamics The net muscle force excites the mass-spring-damper system:

$$F_{net} = m\ddot{x} + b\dot{x} + kx \tag{4.3}$$

To interconnect the muscle model with the load model, we first write all equations in terms of the same coordinate system. We use the following transformation:

$$\begin{aligned} x_1 &= x_1^o + x \quad ; \quad \dot{x}_1 = \dot{x} \\ x_2 &= x_2^o - x \quad ; \quad \dot{x}_2 = -\dot{x} \end{aligned}$$

where x_1^o and x_2^o are the nominal lengths of the muscles. Therefore, the muscle force equations become:

$$\begin{aligned} F_1 &= A_1 + B_1(x_1^o + x) + C_1\alpha_1 + D_1(x_1^o + x)\alpha_1 + E_1\dot{x} + \\ &\quad G_1\dot{x}\alpha_1 + H_1(x_1^o + x)\dot{x} + I_1(x_1^o + x)\dot{x}\alpha_1 \\ F_2 &= A_2 - B_2(x - x_2^o) + C_2\alpha_2 - D_2(x - x_2^o)\alpha_2 - E_2\dot{x} - \\ &\quad G_2\dot{x}\alpha_2 + H_2(x - x_2^o)\dot{x} + I_2(x - x_2^o)\dot{x}\alpha_2 \end{aligned}$$

The net force is therefore given by:

$$\begin{aligned} F_{net} &= F_2 - F_1 \\ &= (A_2 - A_1) - B_2(x - x_2^o) - B_1(x_1^o + x) + (C_2\alpha_2 - C_1\alpha_1) + \\ &\quad -D_2(x - x_2^o)\alpha_2 - D_1(x_1^o + x)\alpha_1 - (E_2 + E_1)\dot{x} - (G_2\alpha_2 + G_1\alpha_1)\dot{x} + \\ &\quad (H_2(x - x_2^0) - H_1(x_1^o + x))\dot{x} + (I_2(x - x_2^o)\alpha_2 - I_1(x_1^o + x)\alpha_1)\dot{x} \end{aligned} \tag{4.4}$$

System state equations Let the system state vector be $\mathbf{x} = [\alpha_1; \beta_1; \alpha_2; \beta_2; x; \dot{x}]$, and the control vector be $\mathbf{u} = [u_1; u_2]$. The dynamics of the interconnected system are written as:

$$\begin{aligned} \dot{\mathbf{x}} &= \begin{bmatrix} \dot{\alpha}_1 \\ \dot{\beta}_1 \\ \dot{\alpha}_2 \\ \dot{\beta}_2 \\ \dot{x} \\ \ddot{x} \end{bmatrix} = \begin{bmatrix} p_{\alpha_1} & 1 & & & & \\ & p_{\beta_1} & & & & \\ & & p_{\alpha_2} & 1 & & \\ & & & p_{\beta_2} & & \\ & & & & 0 & 1 \\ & & & & -k/m & -b/m \end{bmatrix} \begin{bmatrix} \alpha_1 \\ \beta_1 \\ \alpha_2 \\ \beta_2 \\ x \\ \dot{x} \end{bmatrix} + \begin{bmatrix} p_{u_1}u_1 \\ \\ p_{u_2}u_2 \\ \\ F_{net}(\mathbf{x},\mathbf{u})/m \end{bmatrix} \\ \dot{\mathbf{x}} &= \mathbf{f}(\mathbf{x},\mathbf{u}) \end{aligned} \tag{4.5}$$

While this system is mostly linear, the nonlinearity is fairly benign in form and is due to the multi-linear nature of $F_{net}(\mathbf{x},\mathbf{u})$. The model of equation 4.5 will be treated as the basis for our analysis.

Given this model, our objective is to maximize the average power transfer from the muscles to the load. The instantaneous power delivered to the load is given by $P(t) = \dot{x}F_{net}$. The

work done by the muscles on the load is the integral of the power over one complete cycle. Therefore, the optimization problem setup becomes

$$\begin{aligned} \max_{\mathbf{u}(t)} \quad & \int_0^T \text{Power}(t)dt = \int_0^T \dot{x}F_{net}dt \\ \text{s.t.} \quad & \dot{\mathbf{x}} = \mathbf{f}(\mathbf{x}, \mathbf{u}) \\ & u_{min} \leq \mathbf{u}(t) \leq u_{max} \\ & \mathbf{x}(0) = \mathbf{x}(T) \end{aligned} \tag{4.6}$$

In this formulation, we assume that the terminal time T is given and is defined by the task objective.

In the next three subsections, I tackle problem 4.6 using three different approaches. In the first approach, a simplified and approximate solution to the problem is developed, which provides an intuitive ground. This solution yields insight to the role of co-activation on the energetics of the muscles, but at the expense of making gross assumptions that may undermine the validity of the approach. In the second approach, we relax many of the assumption and simplifications of the first approach. We use direct simulation to investigate the role of different stimulation parameters on the net output energetics, without resorting to approximations. In the final approach, we adopt a more formal treatment of the problem based on optimal control theory. Thus the three approach are presented in increasing formality.

4.2 Approach 1: A Basic Model

4.2.1 Model simplification

Let us develop a simplified model for the treatment of problem 4.6. We will take liberty in making several assumptions with the goal of achieving tractability.

First consider the muscle model. Based on the results of chapter 3, we established that a bilinear muscle model is plausible. We will use this bilinear formulation with all of its inherent assumptions, but make the additional simplification of ignoring the stimulation-activation dynamics. Therefore, the electrical stimulus signal u_i will be taken as a direct measure of the activation signal α_i.

$$\alpha_i(t) = u_i(t)$$

Based on this, we therefore assume that for each muscle, its contractile force F_i and stiffness K_i are given by

$$\begin{aligned} F_i &= A_i + B_i x_i + C_i \alpha_i + D x_i \alpha_i \\ &= A_i + B_i x_i + C_i u_i + D x_i u_i \\ K_i &= \frac{\partial F_i}{\partial x} = B_i + D_i u_i \end{aligned}$$

In this model, the residual force of the muscle is given by A_i, its passive elasticity is captured by $B_i x_i$, the stimulation dependent contraction is captured by the $C_i u_i$ term, and finally a term that couples activation and elasticity is $D_i x_i u_i$. The coefficients A_i, B_i, C_i, D_i are muscle parameters to be determined either via prior data from the literature, or from identification experiments. See chapter 3.

This bilinear muscle model has two important consequences:

1. Activation dependent stiffness Plotting the force-length curve according to this bilinear model for different values of activation u_i yields the family of curves in figure 4-2(a). The curves are plotted for different values of activation ranging from 0 to 1. Immediately we notice that force is linear in activation, and that the slope of the curves increases with increasing activity. This feature is the essence of the bilinear muscle model – that it captures the stiffening of the muscle with increasing activation.

2. Affine relationship between muscle force and stiffness Another consequence of this model is that, at a given muscle length x, the muscle stiffness is given by a linear relationship with force. This is shown in figure 4-2(b).

Consider an antagonist and identical muscle pair (i.e. $A_1 = A_2 = A, \cdots, D_1 = D_2 = D$). Let us compute the net force and stiffness applied by the muscle pair to the load. The forces are given by

$$\begin{aligned} F_1 &= A + B x_1 + C u_1 + D x_1 u_1 \\ F_2 &= A + B x_2 + C u_2 + D x_2 u_2 \\ F_{net} &= F_2 - F_1 \\ &= B(x_2 - x_1) + C(u_2 - u_1) + D(x_2 u_2 - x_1 u_1) \end{aligned}$$

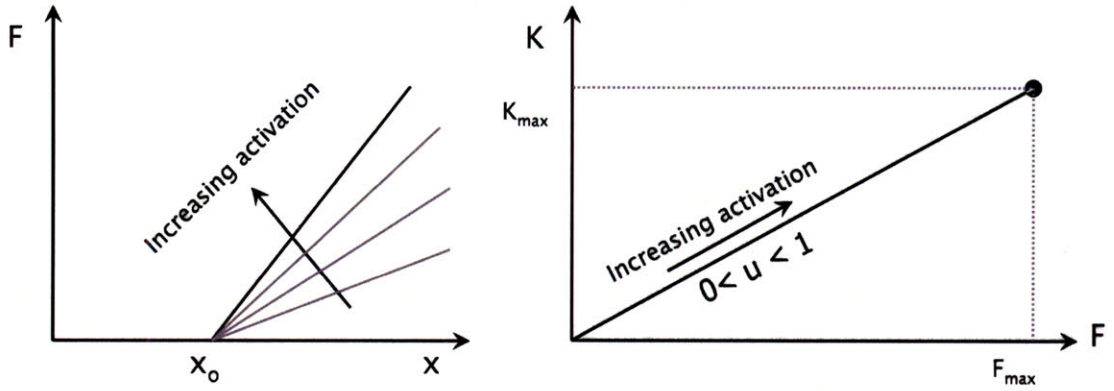

(a) Force-length relationships

(b) Force-stiffness relationship

Figure 4-2: Two properties of the bilinear muscle model

Using the coordinate transformation $x = x_1 = -x_2$, we get[1]

$$\begin{aligned} F_{net} &= -2Bx + C(u_2 - u_1) - Dx(u_2 + u_1) \\ K_{net} = \frac{\partial(-F_{net})}{\partial x} &= 2BD(u_2 + u_1) \\ &= K_1 + K_2 \end{aligned}$$

We plot the net muscle stiffness K_{net} against the net muscle force F_{net} for all combinations of $0 \leq u_1 \leq 1$ and $0 \leq u_2 \leq 1$. The achievable range is indicated by the shaded area in figure 4-3. Furthermore, one can verify that any line segment parallel to the x-axis represents a set of activations with constant sum, i.e. $u_1 + u_2 =$ constant. The diamond shaped region is similar to the co-activation analysis in [59].

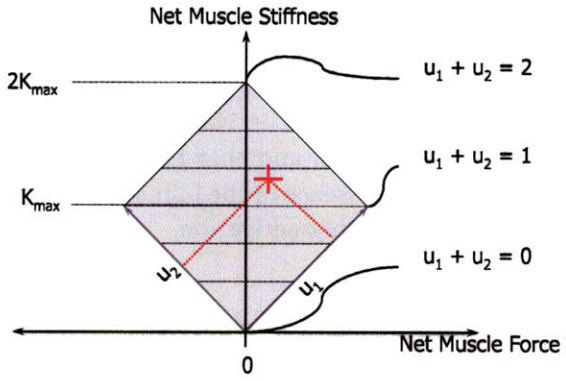

Figure 4-3: Co-activation map for a pair of bilinear muscles. The shaded area indicates achievable net muscle force and stiffness combinations for bounded and non-negative activations. The oblique $[u_1, u_2]$ axes indicated the activation levels required.

Let us make some further simplifications. Assume that this shaded region equally applies to the situation of the muscle pair acting on the mass-spring-damper load, and let us temporarily ignore the fact that this model applies only to isometric activation. Also further

[1]The net stiffness K_{net} is defined as $\frac{\partial - F_{net}}{\partial x}$ to maintain appropriate signs

assume that the load will be excited sinusoidally and antagonistically along those lines of constant activation, i.e.

$$u_1(t) = A_o(1 + \sin(\omega_s t))$$
$$u_2(t) = A_o(1 - \sin(\omega_s t))$$

In making those assumptions, we are conceptually separating the effects of the active stiffness (the Du) of the muscles from the forces produced and other dynamic effects. The resulting equations of motion of this combined muscle-load is

$$M\ddot{x} + B\dot{x} + Kx = -2Bx + C(u_2 - u_1) - D(u_2 + u_1)x$$
$$M\ddot{x} + B\dot{x} + \underbrace{(K + 2B + 2DA_o)}_{K_{total}} x = \underbrace{2CA_o}_{F_{net}} \sin(\omega_s t)$$

From standard harmonic analysis, the net power delivered by the muscles to the load is given by:

$$P(\omega_s) = \frac{F_{net}^2 \omega_s^2 B}{2\left[(K_{total} - M\omega_s^2)^2 + (B\omega_s)^2\right]} \tag{4.7}$$

where F_{net} is the amplitude of the net force produced (indicated by the horizontal abscissa in figure 4-3), ω_s is the driving frequency of stimulation, and K_{total} is defined above. Note that this combined muscle-load system has increased stiffness due to the muscle activation, the natural frequency consequently has increased to $\omega_{total} = \sqrt{K_{total}/M}$.

Equation 4.7 indicates that there are two ways to maximize $P(\omega_s)$. The first is to increase F_{net} as much as possible, since the power increases quadratically with the force applied. The second is to minimize the denominator, by ensuring that $K_{total} = M\omega_s^2$. Those two requirements cannot generally be simultaneously satisfied because of the constraints relating F_{net} and K_{net}, but their effects determine the optimal solution.

Contour and surface plots of the power as a function of F_{net} and K_{total} in equation 4.7 are shown in figures 4-4(a) through 4-4(d) for different driving frequencies ω_s. In order to maximize the net power delivered by the muscles to the system, we need to maximize the value of the power $P(\omega_s)$ over the feasible space indicated by diamond region. The location of the optimal operating points is indicated by the red asterisks in the figures[2].

[2]This optimal point is computed as follows. First, we recognize that the optimal solution must be an extremal solution, and must lie on the boundaries of the feasible space. Therefore we restrict our attention to the constraints given by

$$K_{total} = a_i F_{net} + b_i$$

where a_i and b_i are the slopes and intercepts of the four line segments bounding the feasible region. Solving for the power along those line segments, we get

$$P(\omega_s) = \frac{F_{net}^2 \omega_s^2 B}{2\left[(a_i F_{net} + b_i - M\omega_s^2)^2 + (B\omega_s)^2\right]}$$

Therefore the power is expressed explicitly in terms of the force. Taking derivatives with respect to F_{net}, and setting $\frac{\partial P}{\partial F_{net}} = 0$, we get

$$F_{net}^* = \frac{\omega_s^2(M\omega_s^2 + B^2 - 2b_i M) + b_i^2}{a_i M\omega_s^2 - a_i b_i}$$
$$K^* = M\omega_s^2 + \frac{B^2\omega_s^2}{M\omega_s^2 - b_i}$$

From those figures, an interesting result arises. One would generally expect that the maximal power levels require the muscles to activate in a manner that creates the largest amount of net forces, indicated by the widest level in the diamond shaped region. This is indeed the case in figures 4-4(a) and 4-4(d). The plots of figure 4-4(b) show that at some frequencies, it is better to "back off" a little, and not stimulate the muscles at full amplitudes. At other frequencies, it is better to over-activate the muscles such that the muscles would oppose each others actions 4-4(c). In those cases, the benefit attained from tuning the net frequencies of the muscle actuated system far outweigh the net enhancement of power due to using the full forcing amplitudes.

How do the optimal stiffness and optimal co-activation levels vary with the driving frequency, and what are the resulting power levels? Figure 4-5 shows the trends. We notice that for most of frequencies it is optimal to work with a co-activation level of one, meaning that on average one muscle is fully stimulated. This corresponds to the widest abscissa of the diamond shaped region in figure 4-3, and gives the largest force amplitude. However, for some frequency ranges it is optimal to sacrifice force amplitudes in order to match the resulting resonance frequency ω_{total} with the stimulation frequency ω_s. This effect manifests itself in two ways. In frequency region I (between 6.7 Hz and 7.8 Hz) it is optimal the that the two muscles co-contract in order to achieve this frequency tuning. In region II (between 5.1 Hz and 6.5 Hz), it is optimal that the muscles would do the opposite, i.e. contracting less than they potentially can in order not to over-boost the stiffness and the corresponding ω_{total}.

How does the picture of figure 4-5 change as the system parameters change? Figure 4-6 captures the variation of the optimal power with changes in B, K, K_{muscle} and M.

- **Variation with B (figure 4-6(a))** Since the damping term is the only non-conservative term in the load, we expect that it should be the primary determinant of net average power transfered to the load. We also find that frequency regions I and II diminish with increasing damping. Also note that as B decreases, two effects take place: First, the damping force at a given velocity decreases. Second, the amplitude of velocity of oscillation increases and, theoretically, tends toward infinity for very low values of damping. As B decreases, the velocity increases at a faster than linear rate. The dissipated power is the product of the two terms. Consequently the dissipated power increases with increasing damping. However, $B = 0$, it evaluates to exactly zero, resulting in a discontinuity in the power trend.

- **Variation with K (figure 4-6(b))** The obvious effect is that changing K shifts the resonance frequency ω_{total}, and hence the location of the peak power. Another consequence is that as K increases for a constant K_{muscle}, the ability of the muscle to influence ω_{total} decreases, and therefore the region of optimal co-activation diminishes. Therefore the smaller the nominal stiffness of the load in comparison to the active muscle stiffness, the wider regions I and II are.

- **Variation with K_{muscle} (figure 4-6(c))** Shown in . Similar to changing K, changing K_{muscle} also shifts the resonance frequency, but also offers more influence over the co-

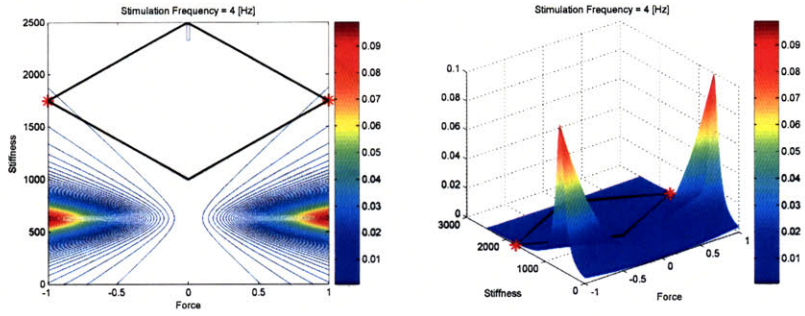

(a) Power function at $\omega_s = 4$ Hz

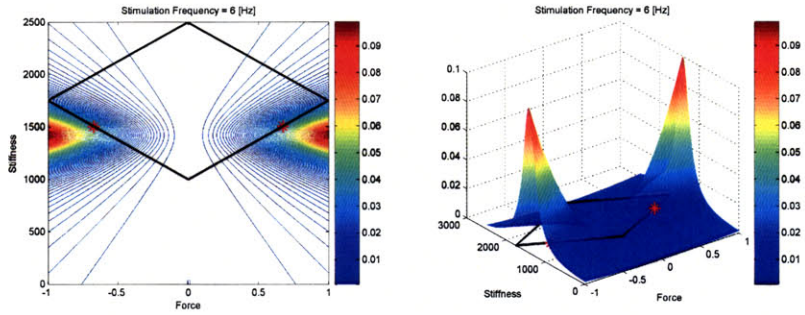

(b) Power function at $\omega_s = 6$ Hz

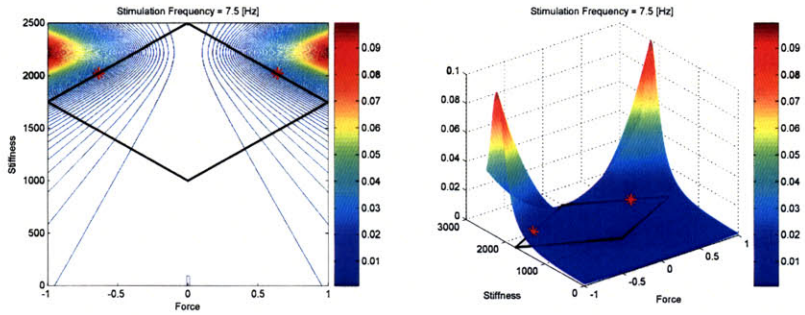

(c) Power function at $\omega_s = 7.5$ Hz

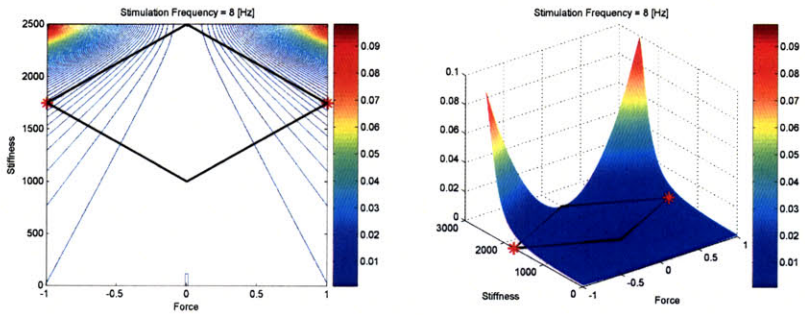

(d) Power function at $\omega_s = 8$ Hz

Figure 4-4: Power function at different frequencies of stimulation ω_s for a system with a nominal natural frequency $\omega_n = 5$ Hz. System parameters are $M = 1$, $B = 5$, $K = 1000$, and the muscle parameters are $A = 0$, $B = 15$, $C = 1$, and $D = 750$.

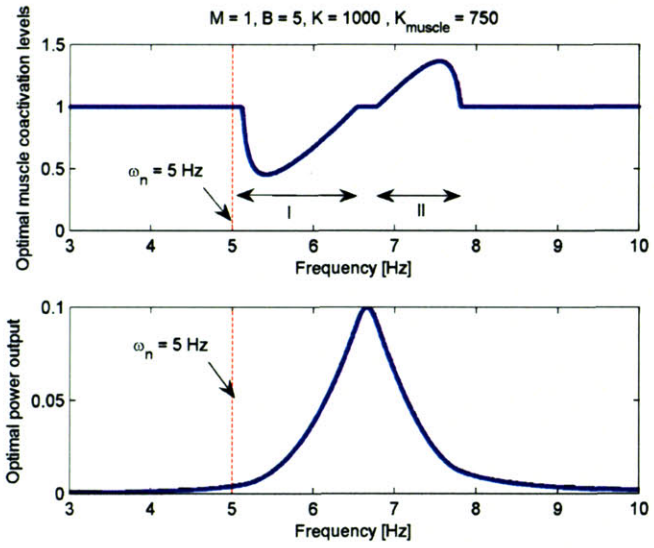

Figure 4-5: Power and co-activation levels as a function of ω_s. The natural frequency of the load ω_n is 5 Hz.

activation ranges. Therefore increasing K_{muscle} relative to K expands the regions I and II.

- **Variation with M (figure 4-6(d))** Again, the change in mass shifts the location of the optimal frequency. We also notice that for smaller mass, the widths of frequency regions I and II increases, but the variance in muscle activity decreases.

Key Points for Approach 1

The analysis above suggests the following:

- According to this simplified bilinear model, there is a constraint between the amplitude of the net force developed by the muscle pair, and the net stiffness. This constraint is characterized by the diamond shaped region in the force-stiffness coordinates shown in figure 4-3.
- The increase in muscle stiffness due to activation augments the nominal stiffness of the mass-spring-damper system. Therefore the resonance frequency of the combined muscle-load system ω_{total} is greater than the resonance frequency of the load without the muscles ω_n.
- For a harmonically excited mass-spring-damper system, the maximum power delivered to the load by the driving source occurs at at a frequency equal to ω_{total}, irrespective of the damping in the system.
- At certain stimulation frequencies $\omega_s > \omega_n$, it is optimal to co-activate the muscles in order to achieve a net increase in stiffness such that ω_{total} is tuned to match the desired excitation frequency ω_s. However, because of the force-stiffness constraint, the co-activation will be at the expense of diminishing force amplitude. But in the final analysis, this may be a dominant factor.

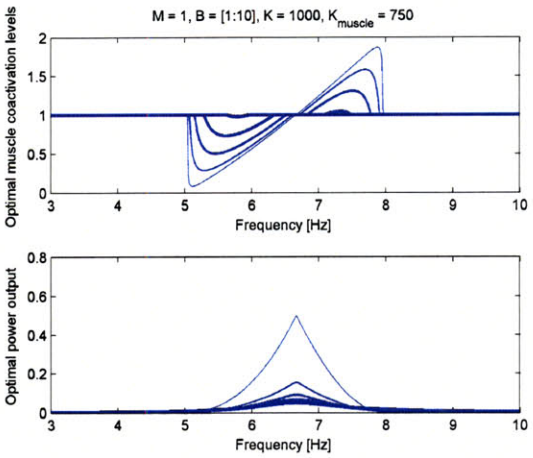

(a) B varies

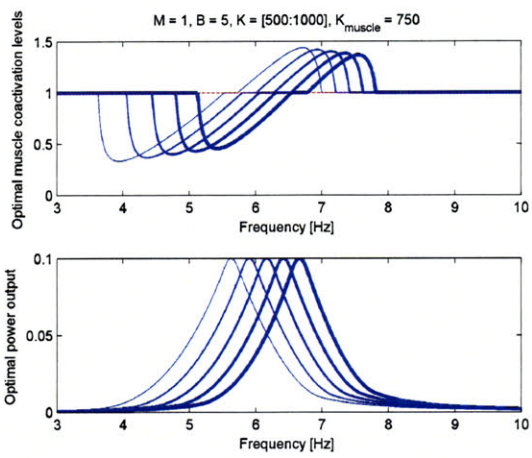

(b) K varies

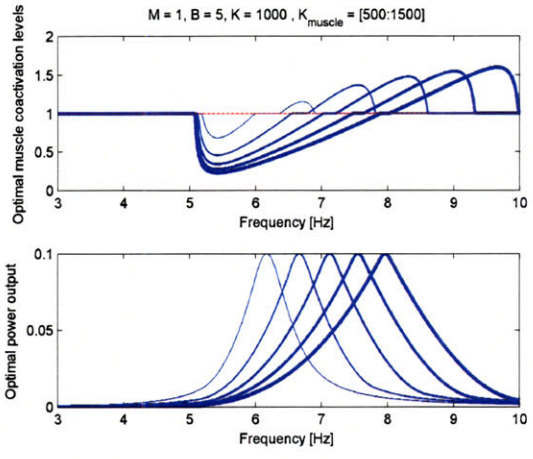

(c) K_{muscle} varies

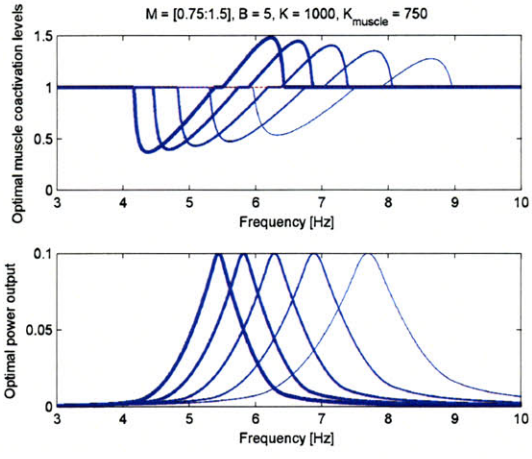

(d) M varies

Figure 4-6: Power and coactivation levels changes with system parameters. The plot titles indicate the range of variation. The thickness of the plot is proportional to the value. For example, in 4-6(a), the thinnest line corresponds to $B = 1$ and the thickest line corresponds to $B = 10$.

- At other frequencies, it is optimal to utilize the maximal amplitude excursions available.

- The absolute maximum power over all frequencies is when ω_s is equal to w_{total} evaluated at $u_1 + u_2 = 1$. This frequency optimal frequency is $w^*_{total} = \sqrt{K^*_{total}/M} = \sqrt{(K+D)/M}$.

These conclusions, however, have been a consequence of a simple model with many simplifying assumptions (in addition to the inherent assumptions of the bilinear muscle model). It is worthwhile to recap some those assumptions here:

- A bilinear muscle model with no velocity dependence holds.

- Ca^{+2} diffusion dynamics are ignored.

- The shape of the feasible space of figure 4-3 is maintained independent of position x.

It is worth noting here that even though this analysis assumed bilinear approximations, one would expect that different approximations would still lead to similar conclusions. As long as the the muscle stiffness increases with muscle force monotonically, and by virtue of the fact the forces of antagonist muscles subtract while their stiffnesses add, the resulting achievable range of force-stiffness combinations will assume a convex region, though not necessarily diamond shaped. The effects of maximizing net force amplitudes and tuning muscle stiffness will still hold in such a situation.

4.3 Approach 2: Direct Search Via Simulation

Another approach to investigating the conditions of optimal muscle power production is via direct simulation. Using the full sixth order model described in equation 4.5, we simulate the system given certain input signals $u_1(t)$ and $u_2(t)$, and compute the net delivered to the loads. We then search through a family of stimulus signals for the optimal power. We restrict our attention to stimulus trains that are are periodic, consisting of a single "on-period" per cycle. Thus, for a given load, these simulations will give us sub-optimal control trajectories, since we restricted the shape of the stimuli. The parameters we vary are the stimulus driving frequency ω_s, the pulse width t_{stim} and the phase ϕ between the signals for u_1 and u_2. Figure 4-7 shows different examples of control inputs with different parameters.

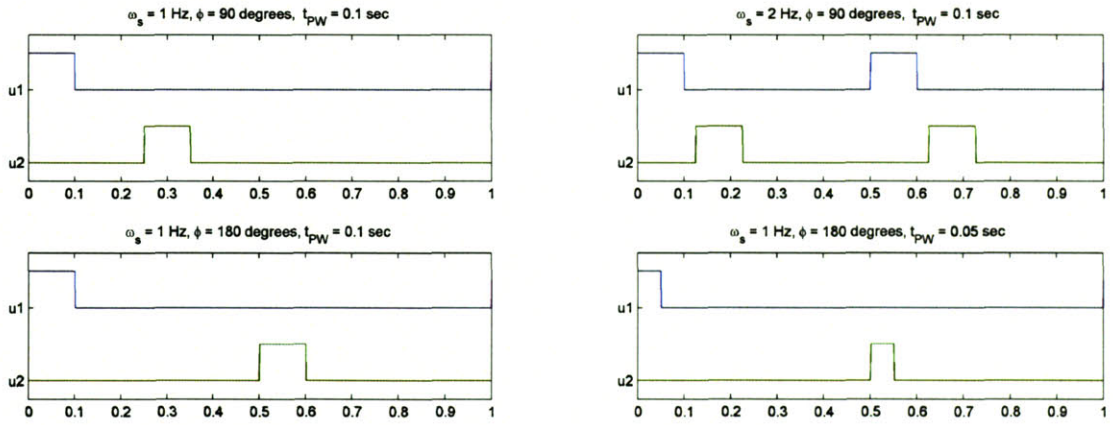

Figure 4-7: Single pulse control inputs with difference parameters

The procedure to construct the numerical simulations is as follows:

- Generate periodic control signals $u_1(t)$ and $u_2(t)$, parameterized by ω_s, t_{stim} and ϕ.
- Simulate the system, and obtain a periodic response. The simulation procedure is explained in detail in appendix C.
- Compute the average power, co-activation level, and average overall stiffness, all integrated over one complete cycle
- Vary stimulation parameters ω_s, t_{stim} and ϕ.
- Find the conditions for maximal power transfer.

Simulation Results

We run the simulations for a system with the following parameters: $A_1 = A_2 = 0$, $B_1 = B_2 = 15$, $C_1 = C_2 = 1$, $D_1 = D_2 = 750$, $M = 1$, $\omega_n = 2\pi 4$ rad/s $= 4$ Hz, and $\zeta = 0.1$. This results in a stiffness $K = 631$ and $B = 5$. The parameters of the calcium diffusion dynamics were chosen such that the system gain is 1 and the two poles are at time constants $= 0.05$ sec. We simulate the system as per the procedure above, and observe the average power as the parameters of the stimulation ω_s, ϕ, and t_{stim} are varied.

An example simulation One example result is shown in figure 4-8. In this particular case, the driving stimulation frequency is $w_s = 3$ Hz, with a phase $\phi = 90$ degrees and a stimulation duration of $t_{stim} = 0.1$ sec. The figure shows the plots of all the states, the individual and net forces, the total stiffness due to the muscles, the net power generated and the integrated work, all over one cycle. This particular simulation used 200 harmonics.

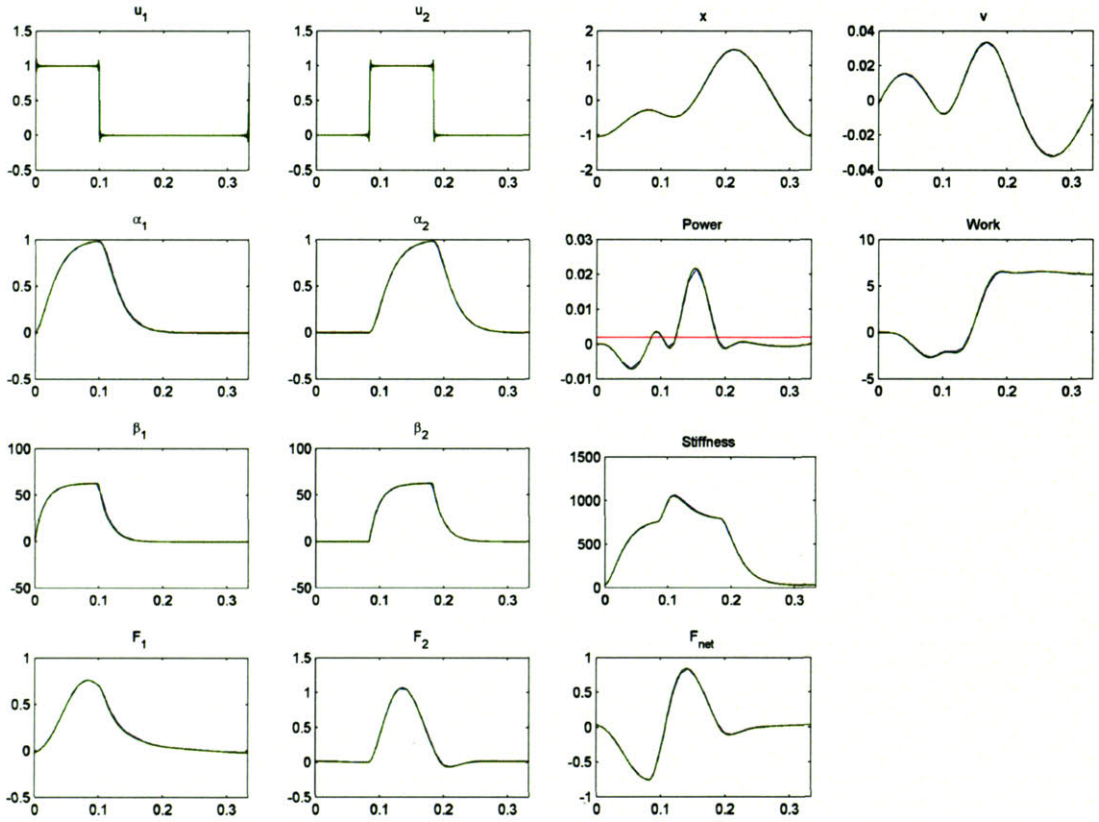

Figure 4-8: Simulation results for one particular case. The x-axis indicates time [sec] for all plots. On each plot, there are two curves that coincide. The green curve is the computation with the Fourier method of appendix C. The blue curve is a Runge-Kutta integration of the system equations with the appropriate initial condition. Since the curves coincide, this validates the Fourier method. The red curve in the power plot indicates the average power, $\bar{P}$, integrated over the full cycle.

From figure 4-8, three important parameters are extracted. The first is the average net power delivered by the muscles $\bar{P}$ (equal to 1.868E-3 in this case). The second is the average stiffness of the combined muscles due to their activations $\bar{K}_{muscle}$ (equal to 480.1 in this case). The third is the average level of co-activation ψ. While the electrical stimulation signals u_i of the two muscles do not overlap in time, the activations are indeed overlapping, and hence providing a net increase in muscle stiffness. We define the co-activation metric

as

$$\psi = \frac{2\int_{t_0}^{t_f} \min(\alpha_1, \alpha_2)\, dt}{\int_{t_0}^{t_f} \alpha_1 dt + \int_{t_0}^{t_f} \alpha_2 dt} \tag{4.8}$$

According to this definition of co-activation, the value of ψ ranges between 0 and 1 for positive activation functions. In the particular case of figure 4-8, the $\psi = 0.26$.

Simulations are repeated for all combinations of the following parameter variations:

- ω_s ranging between 1 Hz and 10 Hz in increments of 0.25 Hz.
- t_{stim} ranging between 0.01 sec and 0.25 sec in increments of 0.02 sec.
- ϕ ranging between 0 degrees and 180 degrees in increments of 5 degrees.

We compute the three quantities aforementioned ($\bar{P}$, $\bar{K}_{muscle}$ and ψ) as a function of the parameters of the control input ω_s, t_{stim} and ϕ.

Stiffness tuning For a fixed t_{stim}, we produce the plots of figures 4-9 and 4-10. For each figure, we produce a surface plot of $\bar{P}$ as a function of ω_s and t_{stim}. The color of the surface indicates ψ. In each plot, there are two planes that cut the surface. The grey plane cuts the surface at the natural frequency of the load (without the influence of the muscles, i.e. at $\omega_s = \omega_n$). The red surface cuts the surface at the frequency that corresponds to the peak power. The distance between those two planes indicates the difference in frequencies that is primarily due to the stiffness contribution of the muscles on the load. In other words, the presences of the muscles, and the activation of the muscles increases the stiffness of the overall system such that $\omega_{total} > \omega_n$.

As one might expect, for longer durations of t_{stim}, the muscles contribute a higher average stiffness to the system across one complete cycle. This is indicated by the larger plane separation distance in figures 4-10. This trend continues up to a point where stiffness tuning does not pay off any longer. When the period t_{stim} becomes excessively long (greater than 0.13 seconds in this case), the muscles are co-activated for most of the cycle of the muscles, and therefore the net forces decrease considerably.

Key Points for Approach 2

- Workloop energetics are explored via direct simulation. The stimulation patterns are restricted to periodic single-pulse waveforms of varying frequencies, pulse-widths and relative phase between the agonist and antagonist control $u_1(t)$ and $u_2(t)$.
- The optimal frequency of muscle stimulation is higher than the natural frequency of the load, primarily due to the stiffening effects the muscles induce to the system. This is consistent with the analysis in section 4.2.

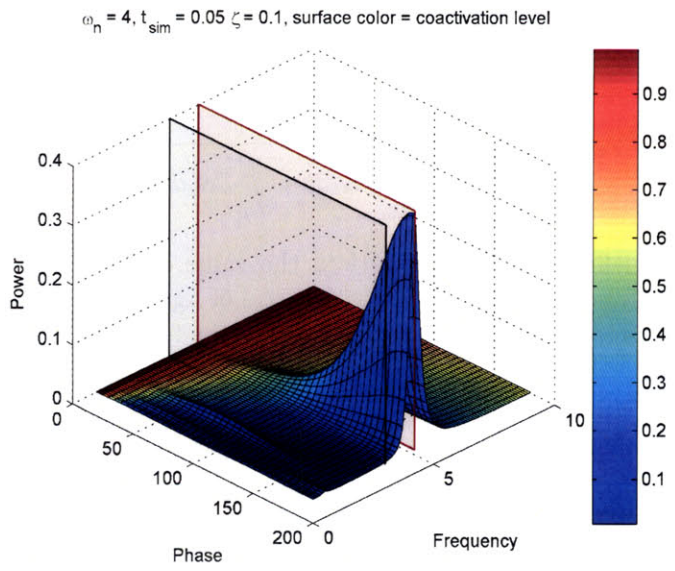

Figure 4-9: Average power acting on the load as a function of phase ϕ and driving frequency ω_s. The period of stimulation has a constant value $t_{stim} = 0.05$. The color of the surface indicates the average co-activation ψ.

4.4 Approach 3: Optimal Control

The basic model above simplified the response of muscles, and overlooked the non-isometric nature of the contractions considered and the activation dynamics. Nevertheless, it provided insight as to the role that the muscle stiffness plays in influencing the net power transfer. The direct simulation approach used a more complete model, however restricted the controls signals to belong to the class of single pulse signals.

To tackle the optimization question more formally and more generally, we seek optimal (or locally-optimal) stimulation patterns that maximize the muscle's energetic function, and observe if co-activation occurs. In this section, we adopt an optimal control approach. The problem formulation is repeated again here:

$$\begin{aligned} \min_{\mathbf{u}(t)} \quad & \int_0^T -\text{Power}(t)dt = \int_0^T -\dot{x}F_{net}dt = \int_0^T L(\mathbf{x},\mathbf{u})\mathbf{dt} \\ \text{s.t.} \quad & \dot{\mathbf{x}} = \mathbf{f}(\mathbf{x},\mathbf{u}) \\ & u_{min} \leq \mathbf{u}(t) \leq u_{max} \end{aligned}$$

where $\mathbf{f}(\mathbf{x},\mathbf{u})$ is defined in equation (4.5) and $\mathbf{u}(t) = [u_1, u_2]^T$ is the control input vector.

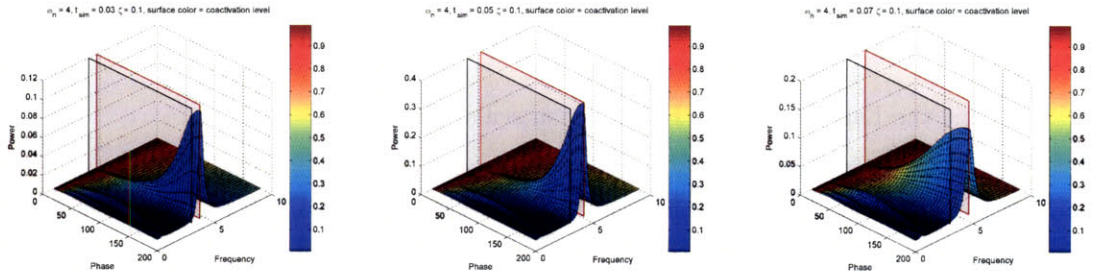

(a) $t_{stim} = 0.01$ sec

(b) $t_{stim} = 0.03$ sec

(c) $t_{stim} = 0.05$ sec

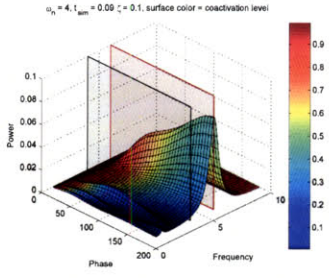

(d) $t_{stim} = 0.09$ sec

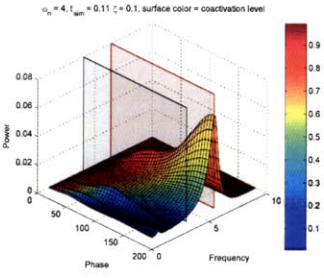

(e) $t_{stim} = 0.11$ sec

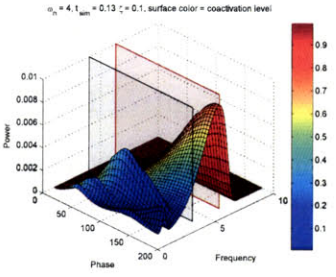

(f) $t_{stim} = 0.13$ sec

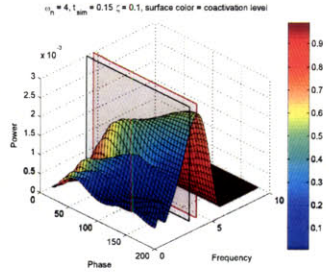

(g) $t_{stim} = 0.15$ sec

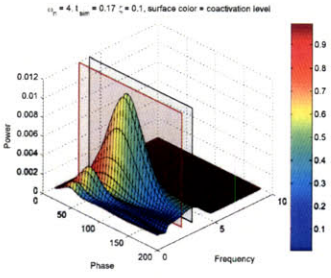

(h) $t_{stim} = 0.17$ sec

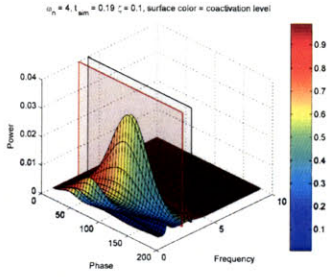

(i) $t_{stim} = 0.19$ sec

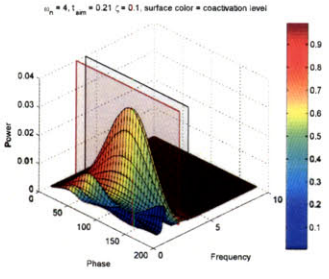

(j) $t_{stim} = 0.21$ sec

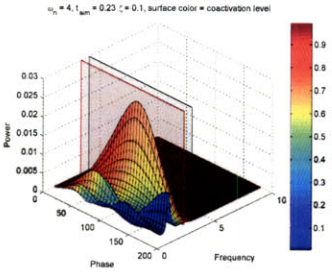

(k) $t_{stim} = 0.23$ sec

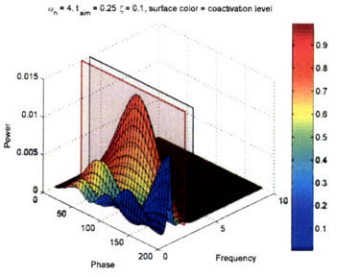

(l) $t_{stim} = 0.25$ sec

Figure 4-10: Replication of the plot of figure 4-9 for different values of t_{stim}. Note that as the activation period increases, the average stiffness increases, and consequently the separation between the two frequency planes increases. This trend breaks down beyond $t_{stim} > 0.13$.

The procedure of the analysis are as based on the application of the Pontryagin minimum principle [10]:

1. Augment the cost function with appropriate multipliers on the constraints.

2. Define the Lagrangian and Hamiltonian scalar functions.

3. Write the equations governing the dynamics of the multipliers.

4. Define the necessary conditions for optimal control.

5. Solve the resulting 2-point boundary value problem.

4.4.1 Control Derivation

Our purpose here is to derive necessary conditions for optimality of the control signals. The integrand of the cost function $L(\mathbf{x},\mathbf{u})$ and the Hamiltonian function $H(\mathbf{x},\mathbf{u})$ are given by

$$\begin{aligned} L(\mathbf{x},\mathbf{u}) &= -\dot{x}F_{net} \\ &= -\dot{x}\left\{(A_2-A_1)-B_2(x-x_2^o)-B_1(x_1^o+x)+(C_2\alpha_2-C_1\alpha_1)\right. \\ &\quad -D_2(x-x_2^o)\alpha_2-D_1(x_1^o+x)\alpha_1-(E_2+E_1)\dot{x}-(G_2\alpha_2+G_1\alpha_1)\dot{x}+ \\ &\quad \left.(H_2(x-x_2^0)-H_1(x_1^o+x))\dot{x}+(I_2(x-x_2^o)\alpha_2-I_1(x_1^o+x)\alpha_1)\dot{x}\right\} \end{aligned}$$

The Hamiltonian is a scalar function defined as

$$H(\mathbf{x},\mathbf{u}) = L(\mathbf{x},\mathbf{u})+\lambda^{\mathbf{T}}\mathbf{f}(\mathbf{x},\mathbf{u})$$

From [10], the evolution of the "optimal" co-state variables are governed by:

$$\dot{\lambda} = -\nabla_{\mathbf{x}}L(\mathbf{x},\mathbf{u})-\nabla_{\mathbf{x}}\mathbf{f}(\mathbf{x},\mathbf{u})\lambda$$

where

$$\nabla_{\mathbf{x}}L(\mathbf{x},\mathbf{u}) = \begin{bmatrix} \frac{\partial L}{\partial \alpha_1} \\ \frac{\partial L}{\partial \beta_1} \\ \frac{\partial L}{\partial \alpha_2} \\ \frac{\partial L}{\partial \beta_2} \\ \frac{\partial L}{\partial x} \\ \frac{\partial L}{\partial \dot{x}} \end{bmatrix} = \begin{bmatrix} C_1\dot{x}+D_1\dot{x}(x_1^o+x)+G_1\dot{x}^2+I_1(x_1^o+x)\dot{x}^2 \\ 0 \\ -C_2\dot{x}+D_2\dot{x}(x-x_2^o)+G_2\dot{x}^2-I_2(x-x_2^o)\dot{x}^2 \\ 0 \\ -\dot{x}\left\{\begin{array}{l} -(B_2+B_1)-(D_2\alpha_2+D_1\alpha_1)+ \\ \dot{x}(H_2-H_1)+\dot{x}(I_2\alpha_2-I_1\alpha_1) \end{array}\right\} \\ \left\{\begin{array}{l} -F_{net}-\dot{x}\{-(E_2+E_1)-(G_2\alpha_2+G_1\alpha_1)+ \\ H_2(x-x_2^o)-H_1(x_1^o+x)+I_2(x-x_2^o)\alpha_2-I_1(x_1^o+x)\alpha_1\} \end{array}\right\} \end{bmatrix}$$

and

$$\nabla_{\mathbf{x}}\mathbf{f}(\mathbf{x},\mathbf{u}) = \begin{bmatrix} \frac{\partial f_1(\mathbf{x},\mathbf{u})}{\partial \alpha_1} & \frac{\partial f_2(\mathbf{x},\mathbf{u})}{\partial \alpha_1} & \cdots & \frac{\partial f_6(\mathbf{x},\mathbf{u})}{\partial \dot{x}} \\ \frac{\partial f_1(\mathbf{x},\mathbf{u})}{\partial \beta_1} & & & \\ \vdots & & \ddots & \\ & & & \vdots \\ \frac{\partial f_1(\mathbf{x},\mathbf{u})}{\partial \dot{x}} & & \cdots & \frac{\partial f_6(\mathbf{x},\mathbf{u})}{\partial \dot{x}} \end{bmatrix}$$

$$= \begin{bmatrix} p_{\alpha_1} & 0 & 0 & 0 & 0 & \frac{1}{m}\{-C_1 - D_1(x_1^o + x) - G_1\dot{x} - I_1(x_1^o + x)\dot{x}\} \\ 1 & p_{\beta_1} & 0 & 0 & 0 & 0 \\ 0 & 0 & p_{\alpha_2} & 0 & 0 & \frac{1}{m}\{C_2 - D_2(x - x_2^o) - G_2\dot{x} + I_2(x - x_2^o)\dot{x}\} \\ 0 & 0 & 1 & p_{\beta_2} & 0 & 0 \\ 0 & 0 & 0 & 0 & 0 & -\frac{k}{m} + \frac{1}{m}\left\{ \begin{array}{l} -(B_2 + B_1) - (D_2\alpha_1 + D_1\alpha_1) + \\ (H_2 - H_1)\dot{x} + (I_2\alpha_2 - I_1\alpha_1)\dot{x} \end{array} \right\} \\ 0 & 0 & 0 & 0 & 1 & -\frac{b}{m} + \frac{1}{m}\left\{ \begin{array}{l} -(E_2 + E_1) - (G_2\alpha_2 + G_1\alpha_1) + H_2(x - x_2^o) - \\ H_1(x_1^o + x) + (I_2(x - x_2^o)\alpha_2 - I_1(x_1^o + x)\alpha_1 \end{array} \right\} \end{bmatrix}$$

The optimal control $\mathbf{u}^*$ is given by

$$\begin{aligned} \mathbf{u}^* &= \arg\min_{\mathbf{u}} H(\mathbf{x},\mathbf{u}) \\ &= \arg\min_{\mathbf{u}} L(\mathbf{x},\mathbf{u}) + \lambda^{\mathbf{T}}\mathbf{f}(\mathbf{x},\mathbf{u}) \\ &= \arg\min_{\mathbf{u}} \lambda^T\mathbf{f}(\mathbf{x},\mathbf{u}) \end{aligned}$$

where the last equality follows since $L(\mathbf{x},\mathbf{u})$ is not a function of $\mathbf{u}$ in this particular context. Therefore

$$\begin{aligned} \mathbf{u}^* &= \arg\min_{\mathbf{u}} \left[\begin{array}{l} \lambda_1(p_{\alpha_1}\alpha_1 + \beta_1) + \lambda_2(p_{\beta_1}\beta_1 + p_{u_1}u_1) + \lambda_3(p_{\alpha_2}\alpha_2 + \beta_2) + \\ \lambda_4(p_{\beta_2}\beta_2 + p_{u_2}u_2) + \lambda_5\dot{x} + \lambda_6\frac{1}{m}(-F_{net} - b\dot{x} - kx) \end{array} \right] \\ &= \arg\min_{\mathbf{u}} [\lambda_2 p_{u_1}u_1 + \lambda_4 p_{u_2}u_2] \end{aligned}$$

which implies

$$\begin{aligned} \Rightarrow u_1^* &= \left\{ \begin{array}{ll} u_{min} & \text{if } \lambda_2 p_{u_1} > 0 \\ u_{max} & \text{if } \lambda_2 p_{u_1} < 0 \end{array} \right. \\ u_2^* &= \left\{ \begin{array}{ll} u_{min} & \text{if } \lambda_4 p_{u_2} > 0 \\ u_{max} & \text{if } \lambda_4 p_{u_2} < 0 \end{array} \right. \end{aligned}$$

Therefore, depending on the signs of the switching functions $\lambda_2 p_{u_1}$ and $\lambda_4 p_{u_2}$, the control assumes only the values u_{min} or u_{max}. This is a *bang-bang control* solution, and is a reasonable outcome. Such solutions are common in minimum time problems. Intuitively,

minimum time implies maximum "acceleration", which is means maximum power. Mathematically, such solutions appear when the Hamiltonian H is a linear function in the control $\mathbf{u}$. In the absence of limits on the control, the optimization problem would be unbounded (which is reasonable, since a muscle that can generate unbounded forces will add infinite power to the load). Therefore, for the problem to be well posed, the bounds on the control inputs u_1 and u_2 are necessary.

The result that the optimal control is bang-bang is reasonable.
In summary, the first order necessary conditions for power optimal solutions are given by:

$$\dot{\mathbf{x}} = \mathbf{f}(\mathbf{x}, \mathbf{u}) \qquad \text{System Dynamics} \qquad (4.9)$$

$$\dot{\lambda} = -\nabla_{\mathbf{x}} L(\mathbf{x}, \mathbf{u}) - \nabla_{\mathbf{x}} \mathbf{f}(\mathbf{x}, \mathbf{u})\lambda \qquad \text{Costate Dynamics} \qquad (4.10)$$

$$u_1^* = \begin{cases} u_{min} & \text{if } \lambda_2 p_{u_1} > 0 \\ u_{max} & \text{if } \lambda_2 p_{u_1} < 0 \end{cases} \qquad \text{Optimal control} \qquad (4.11)$$

$$u_2^* = \begin{cases} u_{min} & \text{if } \lambda_4 p_{u_2} > 0 \\ u_{max} & \text{if } \lambda_4 p_{u_2} < 0 \end{cases}$$

$$\mathbf{x}(t=0) = \mathbf{x}(t=T_f) \qquad \text{State boundary conditions} \qquad (4.12)$$

$$\lambda(t=0) = \lambda(t=T_f) \qquad \text{Costate boundary conditions} \qquad (4.13)$$

Equations (4.9) and (4.10) define a two-point boundary value problem (2-point BVP) that is subject to the cyclic boundary conditions (4.12) and (4.13). This 2-point BVP must be solved simultaneously with the equations for the optimal control (4.11).

Peak Performance vs. Economic Performance – A More General Problem

In a slightly more general formulation, we penalize the cost of the control inputs $\mathbf{u}$ integrated over time. The weight of the control input is designated by η. Therefore, the problem formulation becomes

$$\begin{aligned} J^* &= \min_{\mathbf{u}} \int_0^T \left\{ -F_{net}\dot{x} + \eta \mathbf{u}^T \mathbf{u} \right\} dt \\ \text{s.t.} \quad & \dot{\mathbf{x}} = \mathbf{f}(\mathbf{x}, \mathbf{u}) \\ & 0 \le \mathbf{u} \le 1 \\ & \mathbf{x}(0) = \mathbf{x}(T) \\ \text{where} \quad & \eta \ge 0 \end{aligned}$$

which reduces to the original problem when $\eta = 0$.

The addition of a cost of control to the objective function transforms the problem from a "peak performance problem", to one that takes "efficiency" into account by appropriate choice of η. The presence of the a control quadratic cost will transform the control from bang-bang to one where intermediate values are utilized. The bounds on the control are still in place.

All of the optimization analysis remain essentially unchanged, however, the control terms will change. The co-state evolution equations will not change. The new expressions for the control are given by:

$$\mathbf{u}^* = \arg\min_{\mathbf{u}} \left\{ \lambda_2 p_{u_1} u_1 + \lambda_4 p_{u_2} u_2 + \eta \mathbf{u}^T \mathbf{u} \right\}$$

which evaluates to

$$u_1^* = \begin{cases} u_{max} & \text{if } \frac{-\lambda_2 p_{u_1}}{2\eta} > u_{max} \\ \frac{-\lambda_2 p_{u_1}}{2\eta} & \text{if } u_{min} < \frac{-\lambda_2 p_{u_1}}{2\eta} < u_{max} \\ u_{min} & \text{if } \frac{-\lambda_2 p_{u_1}}{2\eta} < u_{min} \end{cases} \tag{4.14}$$

$$u_2^* = \begin{cases} u_{max} & \text{if } \frac{-\lambda_4 p_{u_2}}{2\eta} > u_{max} \\ \frac{-\lambda_4 p_{u_2}}{2\eta} & \text{if } u_{min} < \frac{-\lambda_4 p_{u_2}}{2\eta} < u_{max} \\ u_{min} & \text{if } \frac{-\lambda_4 p_{u_2}}{2\eta} < u_{min} \end{cases} \tag{4.15}$$

Solution Methods

The solution of the BVP above is non-trivial, primarily due to the discontinuous nature of the control. Even with the addition of the quadratic term, the hard bounds on the control lead to the failure of many of the standard solution algorithms. We solve this issue via the use of penalty methods, which are briefly described in the next section.

Penalty methods Penalty methods simplify the solution of a constrained optimization problem by converting it to a sequence of unconstrained optimization problems [28]. This sequence of problems is solved, with an increasing penalty function added for violating the constraints. In the limit, as the value of the penalty weight increases, the solutions will converge to the optimal solution of the constrained problem.

Consider the following illustrative example. Suppose we want to minimize the function $f(x) = 100x^2 - 100x$ subject to $x \geq 2$ and $x \leq 3$. Figure 4-11(a) shows a plot of this function, and the bounds of the feasible range. From the figure, it is evident that the minimum solution occurs at $x^* = 2$. Also, we notice that the minimizer of the unconstrained $f(x)$ is at $x = 0.5$, indicated by the red asterisk. One way of solving this problem, is to augment a cost for violating the constraints. Therefore, we would minimize a function in the form of $f_k(x) = 100x^2 - 100x + c_k p(x)$, where $p(x)$ is a penalty function for violating the constraints, and c_k is a positive penalty weight. Penalty functions must have the property that $p(x) = 0$ for all x that are within the feasible range, and $p(x) > 0$ for all x that are

infeasible. In this particular example, we choose a quadratic penalty function in the form of

$$p(x) = \begin{cases} (x-3)^2 & \text{if } x > 3 \\ 0 & \text{if } x \text{ is feasible} \\ (2-x)^2 & \text{if } x < 2 \end{cases}$$

This quadratic form of the penalty function has desirable differentiability properties.

We start by solving the problem for $c_k = 0$, and then progressively increase the value of c_k as shown in figure 4-11(b). For each c_k, we get an optimal solution of x_k^*, also indicated by a red asterisk. We monitor the change in the value of x_k^* until further increase in changing the penalty weight does not further change the value of x_k^* significantly. Finally the solution converges to $x_k^* = x^* = 2$.

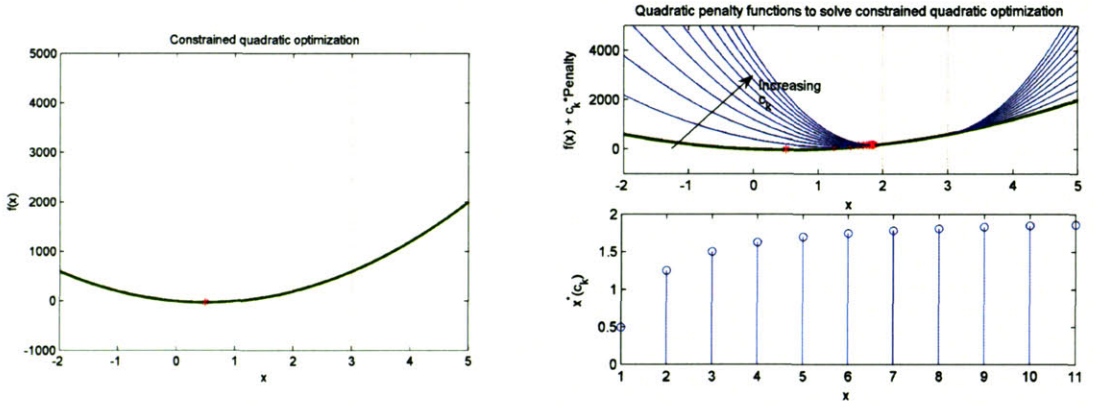

(a) Constrained quadratic optimization

(b) Constrained quadratic optimization with penalty functions

Figure 4-11:

Applying penalty methods to the problem Penalty methods, as described in the section above, are applied to the optimal control problem in the following manner. We would like to make sure that the control is limited to the admissible bounds, i.e. $u_i \leq u_{max}$ and $u_i \geq u_{min}$ for all t. Therefore the penalties are imposed if the control u_i violates those bounds. We also use quadratic penalties in the form of

$$p(u_i) = \begin{cases} (u_i - u_{max})^2 & \text{if } u_i > u_{max} \\ 0 & \text{if } u_i \text{ is feasible} \\ (u_{min} - u_i)^2 & \text{if } u_i < u_{min} \end{cases}$$

Therefore, the optimal control problem takes the following form:

$$
\begin{aligned}
J^* &= \min_{\mathbf{u}} \int_0^T -F_{net}\dot{x} + c_k p(u - u_{max}) + c_k p(u_{min} - u)dt \\
\text{s.t.} \quad & \dot{\mathbf{x}} = \mathbf{f}(\mathbf{x}, \mathbf{u}) \\
& \mathbf{x}(0) = \mathbf{x}(T) \\
\text{where} \quad & \eta \geq 0 \\
& c_k \geq 0 \\
& p(y) = \begin{cases} 0 & \text{for } y < 0 \\ y^2 & \text{for } y \geq 0 \end{cases}
\end{aligned}
$$

Recall that the optimal control was a bang-bang control strategy. This means that, depending on the sign of the switching function, it is optimal to push the control signal as far out as possible. Previously, we placed hard bounds on the signal. With the penalty methods, this bound is softened it becomes optimal to push the control signal as far out until the penalty dominates.

Consider the case if the resulting optimal control is between u_{min} and u_{max}. Then $p(u_i) = 0$. Therefore,

$$
\begin{aligned}
u_1^* &= \arg\min_{u_1} \left\{ \lambda_2 p_{u_1} + \eta \mathbf{u}^T \mathbf{u} \right\} \\
\Rightarrow u_1^* &= \frac{-\lambda_2 p_{u_1}}{2\eta}
\end{aligned}
$$

$$
\begin{aligned}
u_2^* &= \arg\min_{u_2} \left\{ \lambda_4 p_{u_2} + \eta \mathbf{u}^T \mathbf{u} \right\} \\
\Rightarrow u_2^* &= \frac{-\lambda_4 p_{u_2}}{2\eta}
\end{aligned}
$$

If $\frac{-\lambda_2 p_{u_1}}{2\eta} > u_{max}$ or $\frac{-\lambda_4 p_{u_2}}{2\eta} > u_{max}$, then $p(u_i) = (u_i - u_{max})^2$. Therefore,

$$
\begin{aligned}
u_1^* &= \arg\min_{u_1} \left\{ \lambda_2 p_{u_1} + \eta \mathbf{u}^T \mathbf{u} + c_k(u_1 - u_{max}) \right\} \\
\Rightarrow u_1^* &= \frac{2c_k u_{max} - \lambda_2 p_{u_1}}{2(\eta + c_k)}
\end{aligned}
$$

$$
\begin{aligned}
u_2^* &= \arg\min_{u_2} \left\{ \lambda_4 p_{u_2} + \eta \mathbf{u}^T \mathbf{u} + c_k(u_2 - u_{max}) \right\} \\
\Rightarrow u_2^* &= \frac{2c_k u_{max} - \lambda_4 p_{u_2}}{2(\eta + c_k)}
\end{aligned}
$$

If $\frac{-\lambda_2 p_{u_1}}{2\eta} < u_{min}$ or $\frac{-\lambda_4 p_{u_2}}{2\eta} < u_{min}$, then $p(u_i) = (u_{min} - u_i^2$. Therefore,

$$u_1^* = \arg\min_{u_1} \left\{ \lambda_2 p_{u_1} + \mathbf{u}^T \mathbf{u}\alpha + c_k (u_{min} - u_1)^2 \right\}$$

$$\Rightarrow u_1^* = \frac{2c_k u_{min} - \lambda_2 p_{u_1}}{2(\eta + c_k)}$$

$$u_2^* = \arg\min_{u_2} \left\{ \lambda_4 p_{u_2} + \mathbf{u}^T \mathbf{u}\alpha + c_k (u_{min} - u_2)^2 \right\}$$

$$\Rightarrow u_2^* = \frac{2c_k u_{min} - \lambda_4 p_{u_2}}{2(\eta + c_k)}$$

In summary:

$$u_1^* = \begin{cases} \dfrac{-\lambda_2 p_{u_1}}{2\eta} & \text{if } u_{min} < \dfrac{-\lambda_2 p_{u_1}}{2\eta} < u_{max} \\ \dfrac{2c_k u_{max} - \lambda_2 p_{u_1}}{2(\eta + c_k)} & \text{if } \dfrac{-\lambda_2 p_{u_1}}{2\eta} > u_{max} \\ \dfrac{2c_k u_{min} - \lambda_2 p_{u_1}}{2(\eta + c_k)} & \text{if } \dfrac{-\lambda_2 p_{u_1}}{2\eta} < u_{min} \end{cases} \tag{4.16}$$

$$u_2^* = \begin{cases} \dfrac{-\lambda_4 p_{u_2}}{2\eta} & \text{if } u_{min} < \dfrac{-\lambda_4 p_{u_2}}{2\eta} < u_{max} \\ \dfrac{2c_k u_{max} - \lambda_4 p_{u_2}}{2(\eta + c_k)} & \text{if } \dfrac{-\lambda_4 p_{u_2}}{2\eta} > u_{max} \\ \dfrac{2c_k u_{min} - \lambda_4 p_{u_2}}{2(\eta + c_k)} & \text{if } \dfrac{-\lambda_4 p_{u_2}}{2\eta} < u_{min} \end{cases} \tag{4.17}$$

We solve this softened version of the problem numerically. We start with low values for c_k, and increase it until $u_i(t)$ violates the bounds constraints to within acceptable errors.

Solving the 2-point boundary value problem The 2-point boundary value problem is solved using the MATLAB solver `bvp4c` for increasing values of c_k. This solver descretizes the solution space to via an adaptive mesh, and fits piecewise cubic functions to each segment. The residuals in the interface points have to match the differential equation, and the boundary conditions. For a description of the algorithm, refer to [66].

The solution approach in this section enables us to investigate a few interesting questions via computation of the power optimal controls. For example, we can vary the parameters of the muscles and the load, and observe their effects on the power generated. We can turn one muscle "off" by setting its coefficients to zero. We can compare the bilinear muscles with linear "impedance-free" actuators by turning the bilinear coefficients to zero. In the next section, some of those questions are investigated.

4.4.2 Optimal control results

In this section, we use the optimal control tools developed to answer questions regarding conditions of muscle optimal power generation:

What control input maximizes the power delivered by the muscles to the load? By computing the optimal control (equations 4.14 and 4.15), and the corresponding system response, we obtain power optimal periodic trajectories. Figure 4-12 shows two examples of the optimal solutions when the commanded driving frequencies F_s are 4 Hz and 5 Hz. The plots show time profiles of the control, activation, forces, stiffnesses, load displacement and velocity, power and workloops.

From the solutions we observe that the input control $u(t)$ is symmetric and 180^o out of phase. We also notice that the co-activation levels (and hence the stiffness of the muscles) are higher for the 5 Hz stimulation than the 4 Hz levels, which is compatible with the notion of increasing the muscle stiffness contributions, and therefore matching the stimulation frequencies to the overall resonance frequencies. We also notice that at 5 Hz stimulation frequency, the input controls $u_1(t)$ and $u_2(t)$ overlap.

What is the effect of muscle impedance (stiffness) on optimal solution? One way to elucidate the effect of muscle impedance is to compare its performance to that of a similar "impedance-free" actuator as shown in figure 4-13. Such an actuator would have the same temporal dynamics (i.e. activation dynamics) and nominal force levels that the muscle would have. In order to realize this, we model the impedance-free actuator as a muscles with identical activation dynamics $G(s)$ to that of the bilinear muscles. However the parameters of the bilinear model do not include impedance effects. For this actuator, the bilinear parameters are set to $A = 0$, $B = 0$, $C = 1$, and most importantly, $D = 0$.

Solving the optimal control problem for various stimulation frequencies results in the plot of figure 4-14. Each point on the curves summarize one solution to the problem as described in figures 4-12. The plots are explained as follows:

- For the impedance free plot, we notice that the optimal power generating frequency coincides with the resonance of the load (4 Hz). We also notice that the peak repeats itself at slower frequencies that have a period time that is an integer multiple of the resonance period time. At those frequencies, the optimal solution collapses to a repetitions of peak power attained at 4 Hz, and hence the repetitous structure of the plot.

- The peak power for the bilinear muscle pair is shifted in comparison to the impedance-free case, in a manner reminiscent of the direct simulations of figure 4-10. The increase in frequency can be estimated form net contributions of the stiffnesses of the muscles, and its average effect on the system resonance frequency.

What is the role of co-activation? Is it an epiphenomenon of activation dynamics? In the previous sections, based on intuitive reasoning, we showed why co-activation may be desirable from a frequency tuning perspective. It may be argued however that any observed co-activation in the optimal solution is an epiphenomenon of the dynamics of Ca^{2+} release and re-uptake (which were not modelled in approach I). To test for this effect, we compare the co-activation levels for the optimal solution with muscles and compare it to

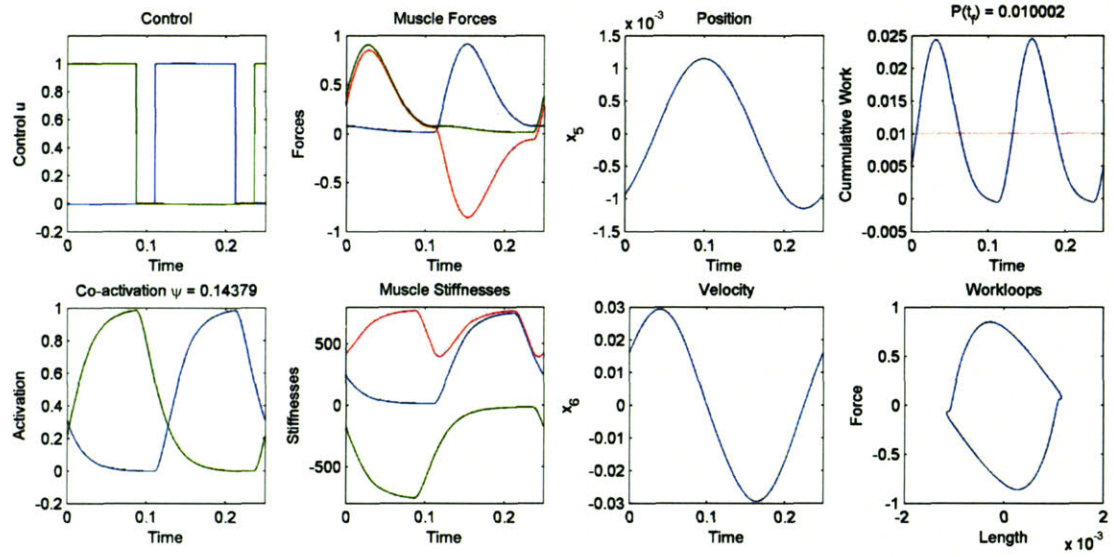

(a) Optimal solution at $F_s = 4$ Hz.

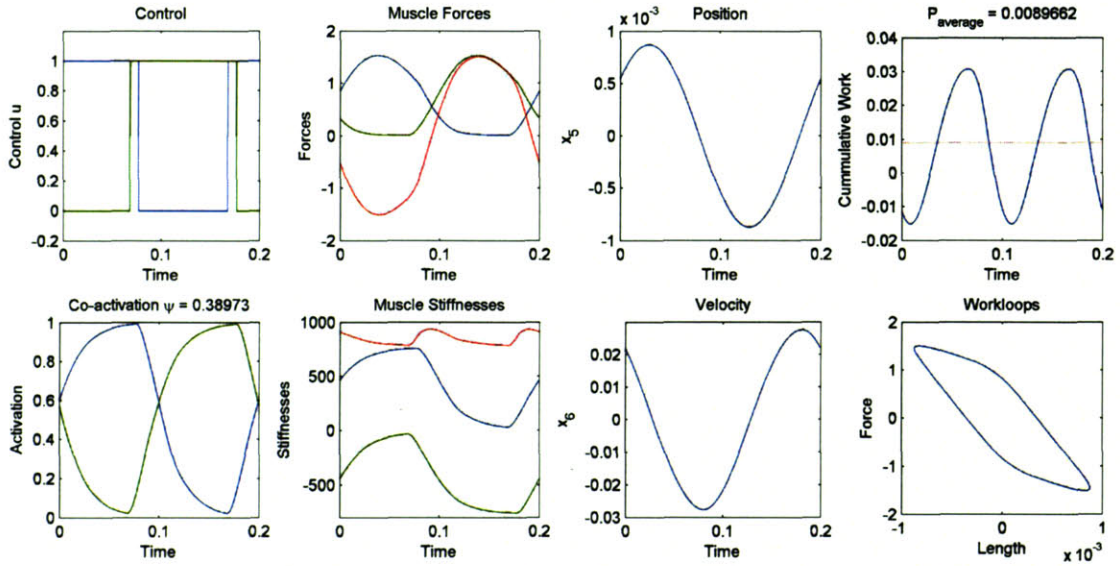

(b) Optimal solution at $F_s = 5$ Hz.

Figure 4-12: Optimal control solutions. The blue traces are for the agonist muscle, green for the antagonist and red for the net quantities (such as net force and net stiffness).

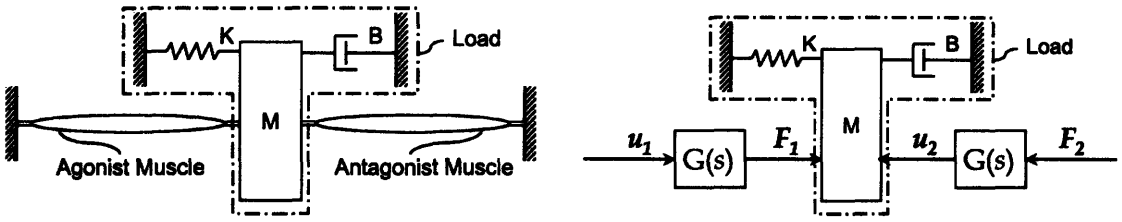

(a) Two muscles

(b) Two impedance-free muscles

Figure 4-13: Comparison of muscles with impedance-free actuators

the co-activation levels with the impedance-free actuators. The results are shown in the lower plot of figure 4-14.

It becomes evident from the plots that there is a certain baseline of co-activation that is unavoidable because of Ca^{2+} dynamics. This co-activation unavoidable because the activation dynamics do not allow the muscle to turn on or off sufficiently fast to accommodate the required stimulation frequencies. Therefore this baseline co-activation increases linearly with frequency F_s. The apparent jumps in the optimal co-activation levels is due the repetitious pattern described above. This curve is then taken as the impedance-free co-activation baseline.

For the bilinear muscles, there is a clear modulation about this baseline. The manner in which this level is modulated is very similar to the pattern of figure 4-5. Similar explanations are attributed: at frequencies higher than the optimal frequencies, the muscles are co-activated more than is required by the impedance-free co-activation baseline in order to stiffen the muscles to tune the system stiffness appropriately. At lower frequencies, the optimal solution "backs-off", and stimulates activates the muscles less than what is required.

Can antagonist muscles cooperate to produce more power than the sum of individual muscles? We compare the optimal solutions of two bilinear muscles to the optimal solution of one bilinear muscle driving on the same load. The comparisons are shown in figure 4-15. It becomes evident from the figure that, at all frequencies, the power from two bilinear muscles is always greater than two muscles, sometimes reaching a peak of approximately 9 times higher or more. While the peak powers have a ratio of 4, the comparison at given stimulation frequencies may enable a more favorable comparison.

How does this level of cooperation compare with that of two impedance-free muscles? We compare the optimal solutions of two impedance-free actuators to the optimal solution of one impedance-free actuator acting on the same load. The comparisons are shown in figure 4-16. The power ratio is a constant at 4 throughout (with the exception of two notches that are numerical errors at small power levels).

How does the speed of Ca^{2+} dynamics affect net co-activation levels? One way to investigate this effect would be to replicate the plots of figure 4-14 but for various models of Ca^{2+} dynamics with different speeds. Particularly, we focus on the the location of the poles of $G(s)$, and the compare how the diffusion rates affect the net energetics of the system.

Plots are shown in figures 4-17 and 4-17 for the impedance-free and the bilinear cases. Again, each point on the curves is a solution of the appropriate optimal control problem.

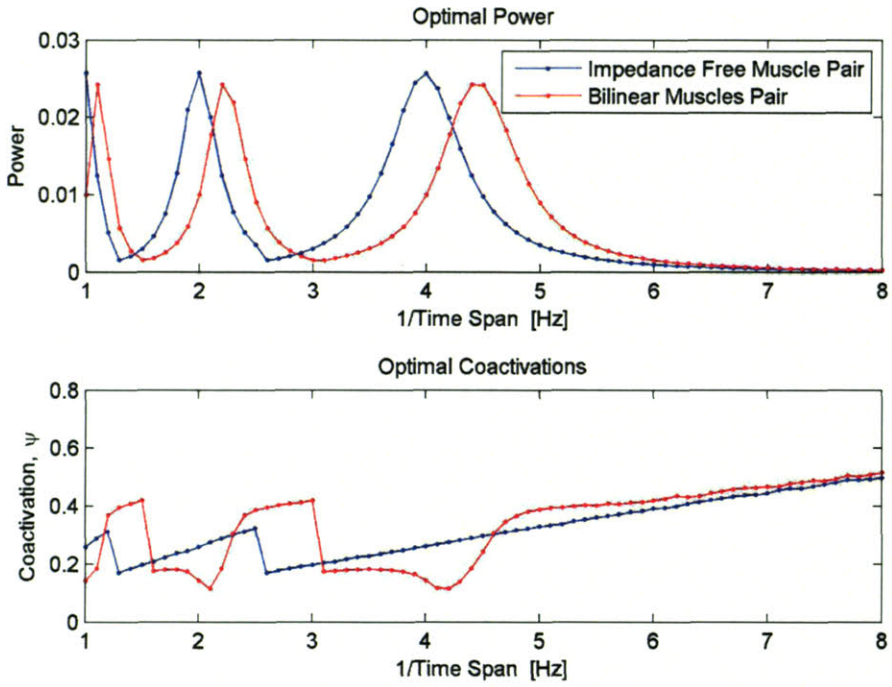

Figure 4-14: Power comparison between bilinear and impedance free muscles. Top: power levels for the given time span. Bottom: resulting co-activaiton levels at the optimal solutions.

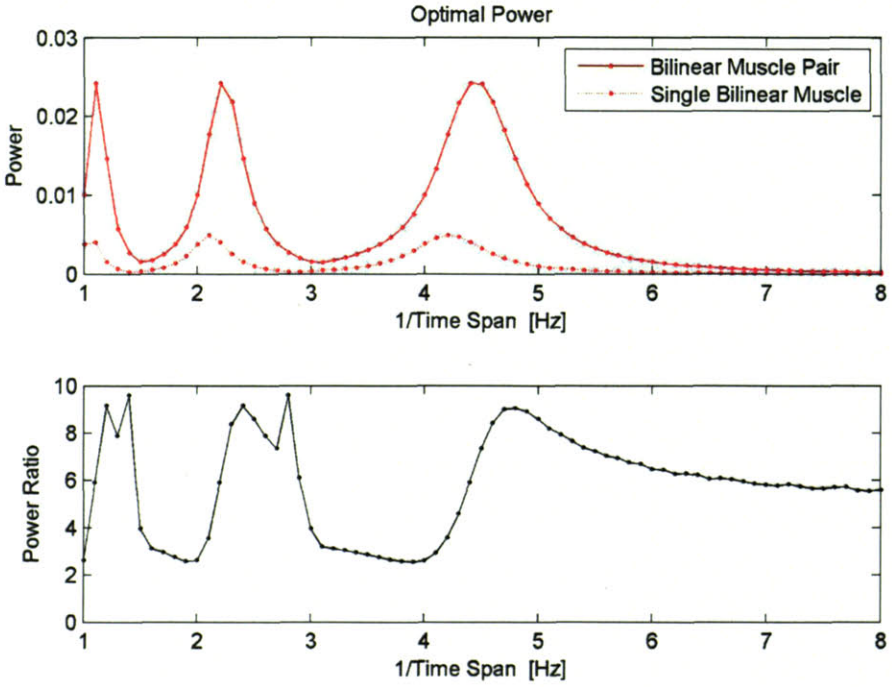

Figure 4-15: Optimal solutions for single and double bilinear solutions

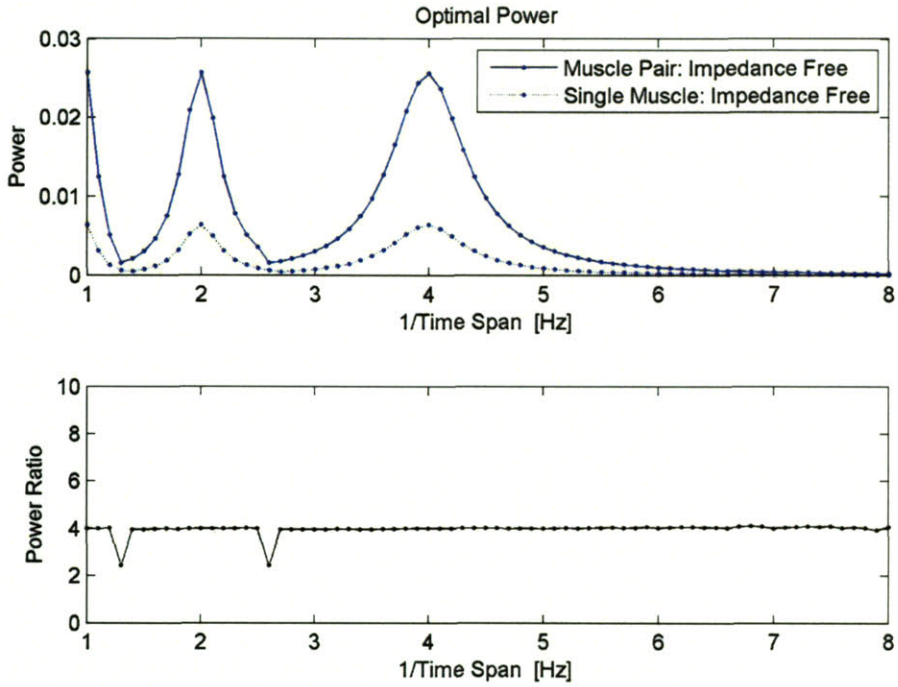

Figure 4-16: Optimal solutions for a single and a pair of impedance free muscles. The two depressions in the power ratio curve are primarily due to simulation noise that is amplified when dividing by small numbers.

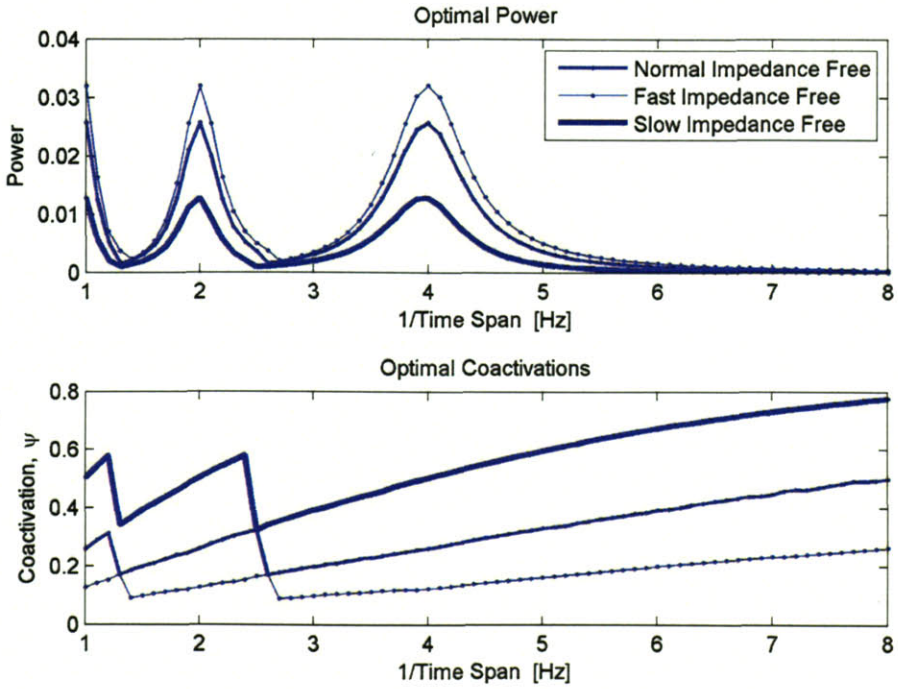

Figure 4-17: Optimal powers and co-activation levels for the impedance free muscles at various speeds

Key Points for Approach 3

- The optimal solutions for the system driven by bilinear muscles is obtained via optimal control analysis. The resulting control was a bang-bang control function, who function and duration are determined by the stimulation period and system parameters.
- The solution was numerically attained using quadratic penalty functions. These functions alleviate the hard non-differentiable control amplitude bounding constraints by adding softer, differentiable costs terms to the objective function. By increasing the weighting factor for these functions, the solution gravitates to a feasible control trajectory.
- Due to the temporal dynamics of the muscles $G(s)$, there is an unavoidable baseline co-activation level that is linearly increasing with frequency.
- The level of optimal muscle co-activation ψ is modulated about the unavoidable baseline so as to modulate the average system impedance to match that of the desired stimulation frequency F_s.
- Faster muscles naturally are more capable of enabling more power, and do so with less co-activation.
- A pair of bilinear muscles may interact in a manner to produce substantially more power at particular frequencies than the power generated by a single muscle.

4.5 An impedance matching interpretation

The analysis in the preceding three sections have direct connections with the engineering notion of impedance matching. When two dynamical networks are interconnected, it is said that the optimal condition for power transfer occurs whenever the "impedances are matched". What does this exactly mean?

In appendix B, an explicit derivation "impedance matching" is presented, primarily for linear systems undergoing either DC or steady-state sinusoidal AC interactions. The results for a bilinear systems in DC conditions are also presented.

Now consider an example of a source network that consists of an ideal force source in series with a spring acting on a mass-spring-damper system. For the case of muscles, co-activation is a knob that changes the stiffness of this in-series spring. The impedance of the load is

$$Z_L = \frac{M(j\omega)^2 + Bj\omega + K}{j\omega} = B + j\left(M\omega - \frac{K}{\omega}\right)$$

The impedance of the source is

$$Z_S = \frac{K_s}{j\omega}$$

Therefore, for this source impedance, we do not have the ability to arbitrarily change the phase. It is always 90^o. For a given driving frequency and a given load, what is the optimal source impedance K_s? From equation B.1:

$$\begin{aligned} X_S &= -X_L \\ &= j\left(\frac{K}{\omega} - M\omega\right) \\ &= \frac{1}{j\omega}\left(M\omega^2 - K\right) \end{aligned}$$

which is equivalent to a source stiffness of $K_s = M\omega^2 - K$. Under such conditions, the total system resonance frequency becomes $\omega_n = \sqrt{(K + K_s)/M} = \sqrt{(K + M\omega^2 - K)/M} = \omega$, which implies that the source stiffness is chosen so that the resonance frequency ω_n of the system matches the desired excitation frequency ω.

In a similar manner, an antagonist muscle pair has the ability to change the source stiffness K_s such that resonance conditions are achieved. The plots in figure 4-12 confirm this. The average stiffness due to the muscles in the plots, when factored with the dynamics of the load, result in a resonance frequency that is the same as the desired excitation frequency.

Chapter 5

Experimental Workloop Measurements

This chapter presents experimental workloop measurements for the thesis problem (as depicted in figure 4-1). All measurements are carried out using the apparatus and protocol described in chapter 2 and the methods therein.

These workloop measures are fundamentally different from the standard measures employed in the muscle physiology literature. To the extent of the authors knowledge, these are the first controlled *in vitro* workloop measures where the muscles interact against a finite-impedance load, and where the muscles have a means to communicate mechanically, and influence each others response. This is not an experimental tweak, but rather a substantially different testing paradigm.

Since a dissected muscle can only be used for a limited amount of *in vitro* experimental measurements, it is prohibitive to test all the conditions described in the workloop optimizations chapter 4. Therefore it becomes necessary to test for certain particular effects. The following two are considered:

- Optimal stimulation frequency: that the power optimal frequency of stimulation must include the effects of muscle stiffness
- Workloops of antagonist muscle pairs: that antagonist muscles may cooperate to generate more power than that produced by the individual muscles acting separately.

Experimental parameters In all of the measurements below, the load is chosen to be a second-order mechanical system with the following parameters: natural frequency $\omega_n = 4$ Hz, damping ratio $\zeta = 0.15$, and a nominal stiffness $K = 3000$ N/m. At each electrical stimulation trigger point, a train of pulses with duration of 50 ms, frequency 200 Hz and pulse width of 100 μs is delivered to the muscles via the electrodes as shown in figure 5-1. Thus each train consists of 10 pulses. The amplitudes of the pulses vary for each particular muscle specimen, primarily depending on the contact between the electrodes and the muscle. However, for a particular muscle, once the amplitude is set, it is maintained constant for all measurements taken on that particular muscle. The load stimulation frequency F_s is controlled by the frequency of triggering the stimulator. This varies, and will be indicated, depending on the experimental conditions. Typically the stimulus trigger frequencies range between 4 to 6 Hz (in relation to the $\omega_n = 4$ Hz load), but will be indicated for each pertaining measurement.

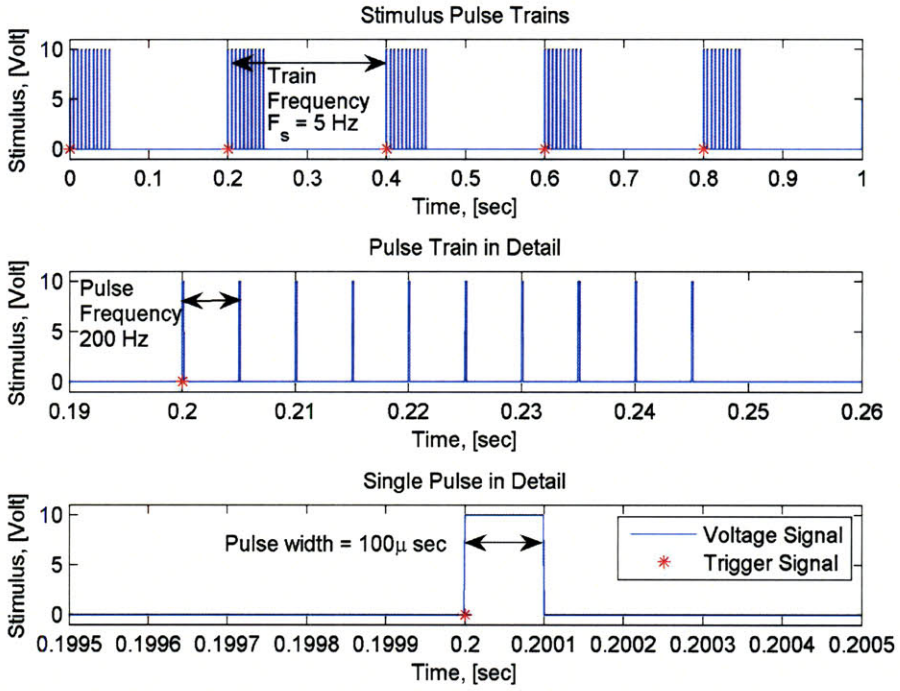

Figure 5-1: Description of a typical stimulus signal for the workloop experimental measurements.

Factoring out fatigue Since the muscles fatigue as workloops measurements progress in time, absolute measurements of power penalize measurements taken at a later stage of an experimental session as compared to those taken earlier. Therefore we focus on taking the *ratios* between successive measurements. For example, when comparing the power output of a muscle pair under two different conditions (A and B), we take a series of alternating measurements at $[A, B, A, B, A, B, \ldots]$. The absolute values of the measurements are expected to decrease as the muscle fatigues. However, the ratios of the power output at two successive measurements is assumed not to be significantly affected by fatigue, but are assumed to be affected only by the difference between the measurement conditions. Another reason for considering ratios is that it becomes necessary to compare outcomes from different muscle preparations. There is a considerable variation in the size of the frogs obtained (whole body mass ranges between 29 grams and 46 grams). This inevitably affects the size of the dissected muscles, and thus their power outputs.

5.1 Workloops with Antagonist Muscle Pairs

I start by showing two individual workloop measurements for a muscle pair. In these measurements, the muscles act against the load, and are stimulated in an alternating manner. Figures 5-2(a) and 5-2(b) shows the time domain force and position data for 4 Hz stimulation frequency, with the system starting from rest. Stimulus trigger points are indicated on the figure via the red and green lines.

This data is replotted in the form of a workloop in figures 5-2(c) and 5-2(d). Each workloop for each muscle is plotted in the respective coordinates of each muscles coordinates, and therefore all the workloops have the same sense. The net workloops, plotting the net force against position, are plotted in figure 5-2(e), and the net work generated by the muscle pair for consecutive cycles is plotted in figure 5-2(f).

By comparison, the workloops for a stimulation frequency of 5 Hz are all plotted in a similar manner in figure 5-3. A few observations are made:

- The first cycle has a substantially lower amplitude oscillation amplitude since the system starts from resting initial conditions. This is in contrast to standard muscle testing experiments where the motion is imposed on the muscles, and steady state conditions may be achieved prior to muscle stimulations.
- As cycles progress, the area of the workloops diminish due to muscle fatigue.
- The magnitude and shape of the workloops change considerably with frequency. The change in shape (from a more rounded workloop at 4 Hz, to a more triangular shape at 5 Hz), may be attributed primarily to the change in phase between the stimulus and response of the load. This change in phase is also apparent from the time domain plots.

It is important to note that these measurements, to the author's knowledge, are the first direct *in vitro* workloop measurements where muscles interact with a finite impedance source. Furthermore, the muscles are interacting against a common load, and thereby communicate mechanically, and can affect one another.

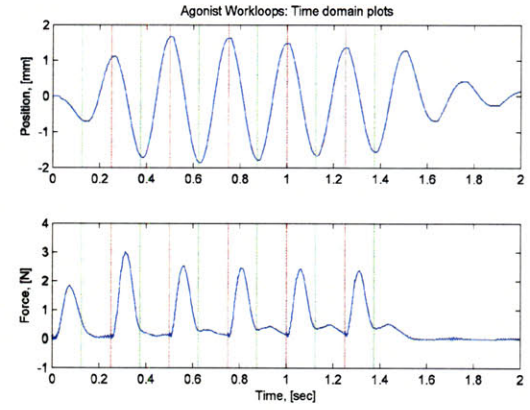

(a) Agonist muscle

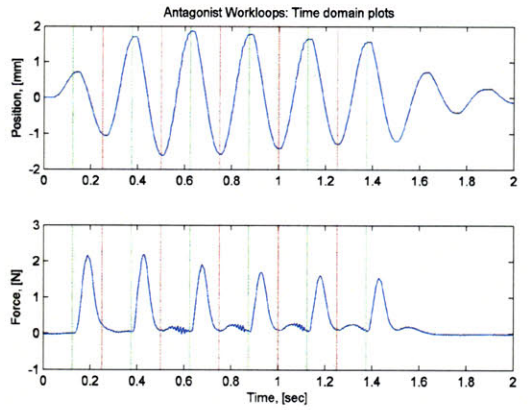

(b) Antagonist muscle

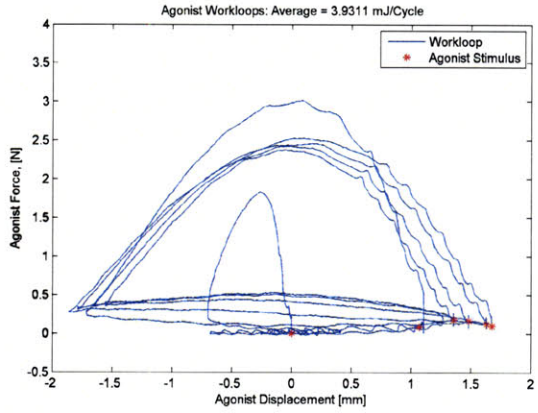

(c) Antagonist muscle

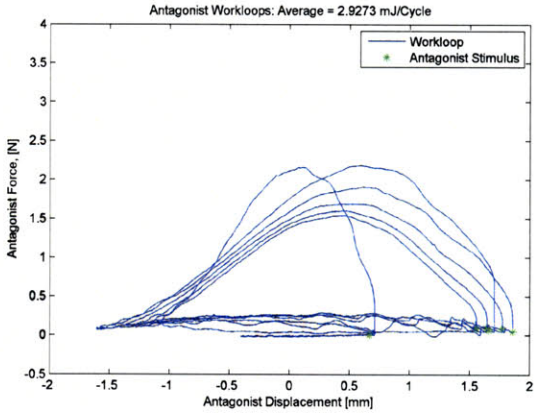

(d) Antagonist muscle

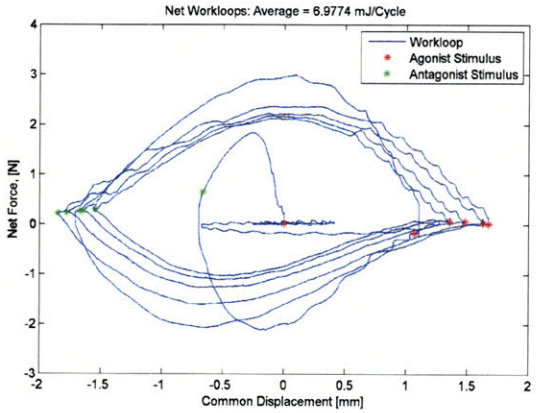

(e) Antagonist muscle

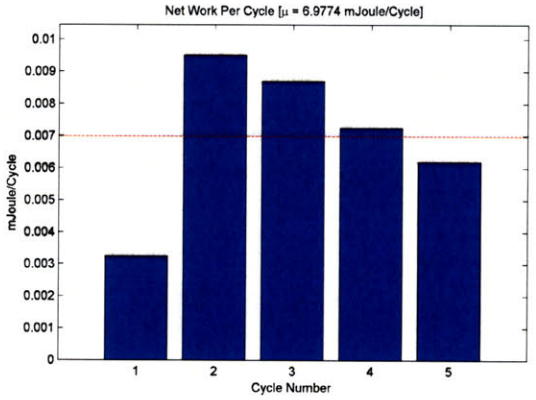

(f) Antagonist muscle

Figure 5-2: Workloop measurements for antagonist muscle pair at 4 Hz with 180^o stimulation phase. Time domain plots for the agonist (a) and antagonist (b) muscles. Respective workloops are plotted in (c) and (d). The net workloops are shown in (e). A bar chart for the net work delivered to the system is shown in (f). The red and green lines in (a-b) and asterisks in (c-e) represent the stimulus trigger times for the agonist (red) and anatagonist (green) muscles. For plots (a) through (d), positive position values indicate a lengthening muscle, while positive force values are contractile.

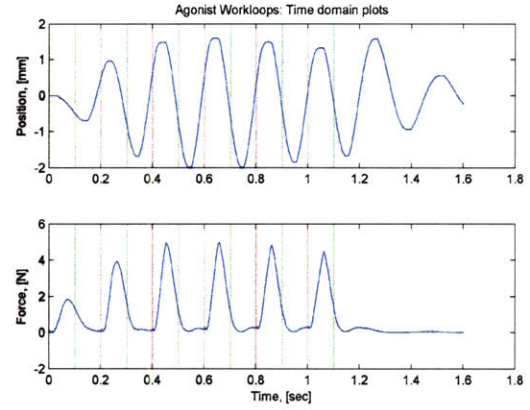

(a) Agonist muscle

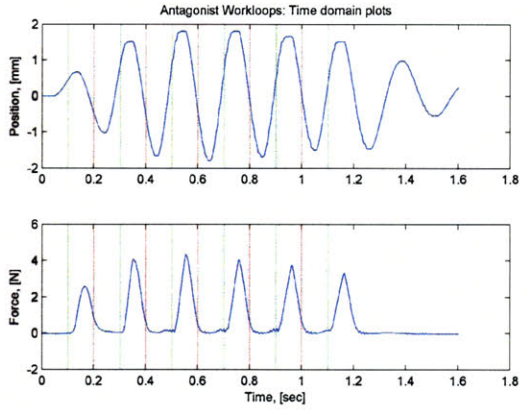

(b) Antagonist muscle

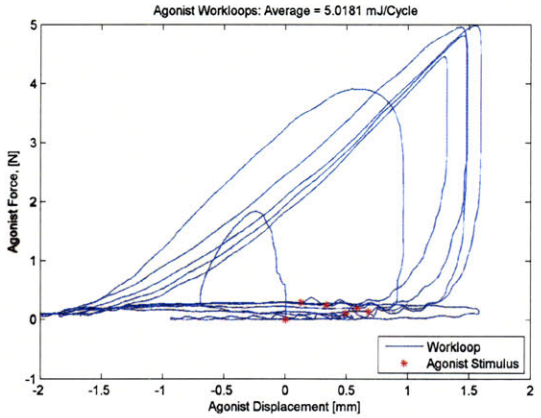

(c) Antagonist muscle

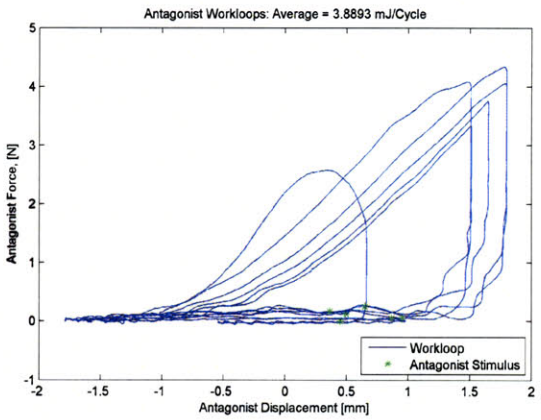

(d) Antagonist muscle

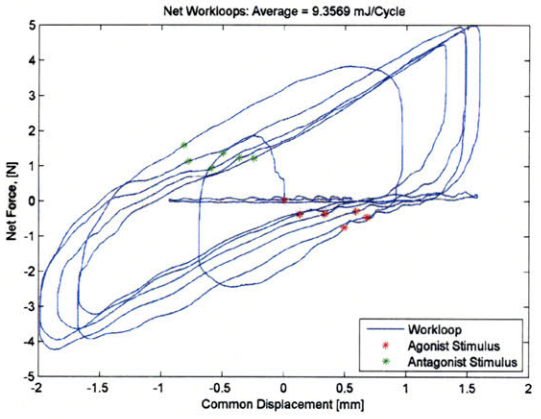

(e) Antagonist muscle

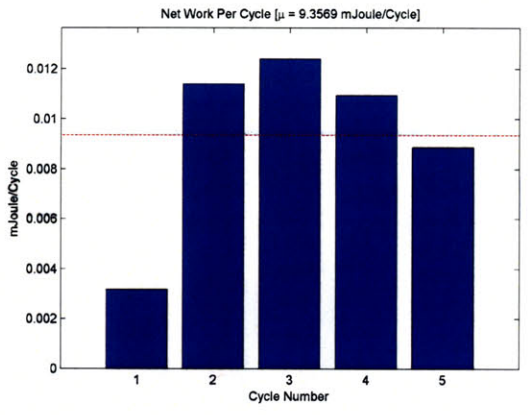

(f) Antagonist muscle

Figure 5-3: Workloop measurements for antagonist muscle pair at 5 Hz with 180^o stimulation phase. Time domain plots for the agonist (a) and antagonist (b) muscles. Respective workloops are plotted in (c) and (d). The net workloops are shown in (e). A bar chart for the net work delivered to the system is shown in (f). The red and green lines in (a-b) and asterisks in (c-e) represent the stimulus trigger times for the agonist (red) and antagonist (green) muscles. For plots (a) through (d), positive position values indicate a lengthening muscle, while positive force values are contractile.

5.2 Optimal Stimulation Frequency

Now that individual workloop data sets are shown, let us focus testing some of the ideas proposed as a consequence of the optimization results of chapter 4. We start with the notion that the optimal frequency of stimulation of the system must take into account the enhanced muscle stiffness due to activation. The muscle-actuate system is stimulated at 4, 5 and 6 Hz, and a comparison of the net workloop energetics is made.

The experimental conditions considered are summarized in table 5.1. Bar charts showing absolute and ratiometric power measures are shown in in figures 5-4 and 5-5. A final comparison of the power at different frequencies is compiled in figure 5-6.

Muscle Pair	Frequency Comparison	Number of measurements
1	4 & 5 Hz	4
2	4 & 5 Hz	4
3	6 & 5 Hz	7
4	6 & 5 Hz	5

Table 5.1: Frequency conditions

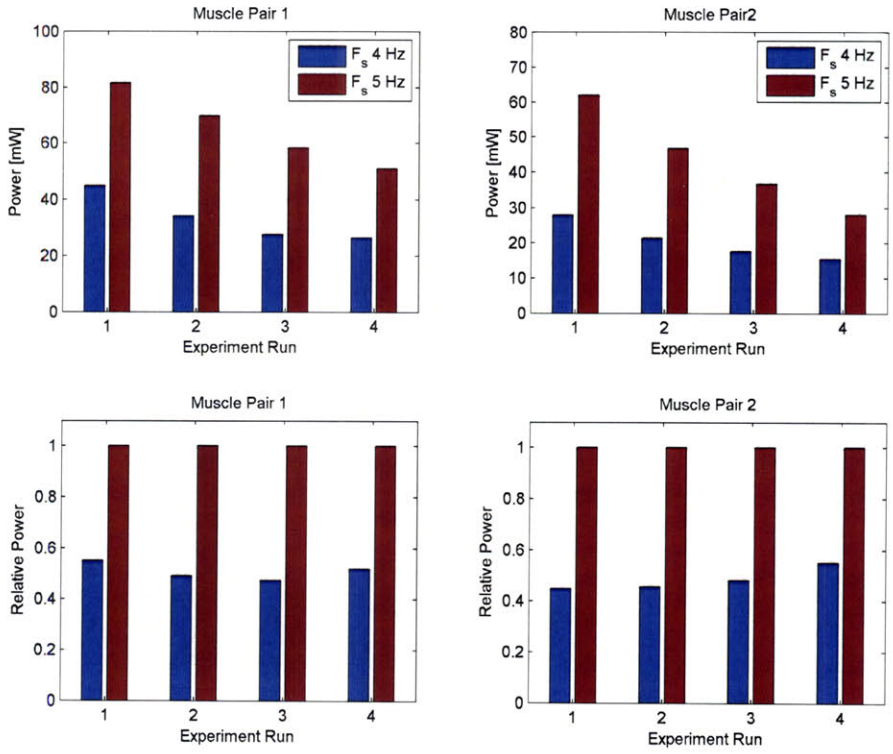

Figure 5-4: A comparison of power output generated by two muscle pairs. Top row compares absolute power at 4 Hz (blue) and 5 Hz (red). Since the muscles fatigue, we notice a declining trend in power measurements. To account for fatigue, power measures are normalized, and we focus on ratios of consecutive measurements.

The experimental evidence thus far supports several notions resulting from chapter 4. Figure 5-6 shows that the optimal frequency for driving this load is closer to 5 Hz than it is

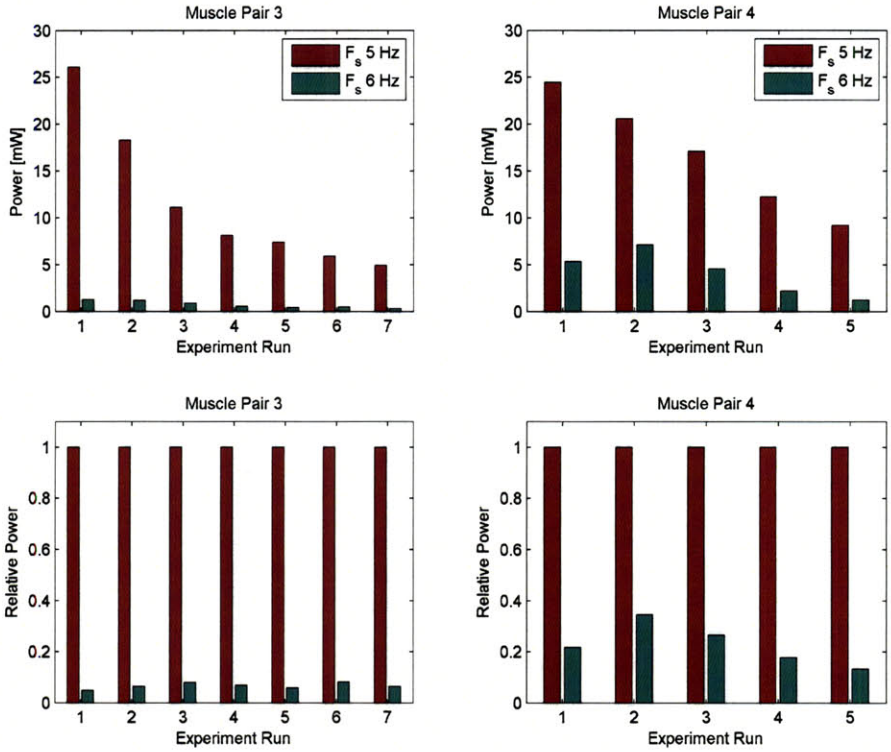

Figure 5-5: A comparison of power output generated by two muscle pairs. Top row compares absolute power at 6 Hz (green) and 5 Hz (red). Since the muscles fatigue, we notice a declining trend in power measurements. To account for fatigue, power measures are normalized, and we focus on ratios of consecutive measurements.

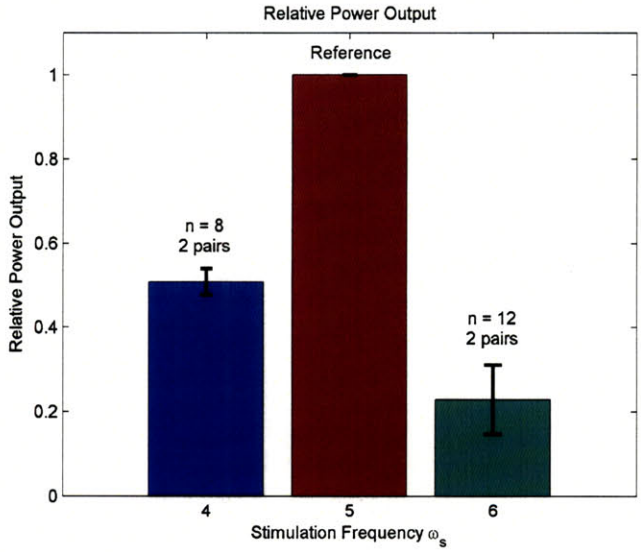

Figure 5-6: Summarizing the data of figures 5-4 and 5-5, the optimal stimulation for power generation is closer to 5 Hz. Error bars indicate 1 standard deviation on the ratiometric measures.

to 4 Hz, which is the natural frequency of the load. This indicates that effects of frequency stiffening are apparent, and that the active stiffness of the actuator must be taken into consideration. While this is not a surprising result, and has been considered in the muscle physiology literature to explain frequencies of oscillation (especially high frequency flight muscle), in this controlled environment we show this effect explicitly.

5.3 Workloops of Antagonist Muscle Pairs

The second idea we investigate experimentally is that a muscle pair actuating a mass-spring-damper system, acting in parallel can produce more power than the sum of powers generated by the individual muscles. Measurements were made on three muscle pairs. For each muscle pair, 9 to 14 measurement sets are taken. For each measurement set, three measurements are taken:

- Workloop power generated by the agonist alone P_a.
- Workloop power generated by the antagonist alone P_n.
- Workloop power generated by the muscle pair stimulated at 180^0 from each other P_{a+n}.

The order in which particular measurements are made within each set is randomized. For each measurement set, the data is normalized by P_{a+n}. Furthermore, the ratio $r = P_{a+n}/(P_a + P_n)$ is computed, which allows us to make comparisons with figure 4-15. Figure 5-7 summarizes the measurements for three muscle pairs. We show raw data, as well as relative power measurements, normalized by P_{a+n} for each set.

Muscle Pair	Number of measurements	Average ratio r
1	9	2.27
2	10	2.20
3	14	1.28

Table 5.2: Frequency conditions

In comparing the measurements of P_{a+n} to $P_a + P_n$, the results a somewhat mixed. The first two muscle pairs show a ratio $r > 2$, clearly indicating the energetic advantage. However, the last measurement showed a smaller ratio (table 5.2), even though the experimental conditions are identical. We also note that for muscle pair 3, measurement sets 1 and 3 show that the ratio r is less than 1. It is not clear why this may be the case.

It is also important to note that the power advantage is less than that predicted in chapter 4. A few factors may contribute to this. First, the muscle parameters (particularly those of the bilinear model), while based on the data from chapter 3, may not necessarily be the same for the particular preparations used. Secondly, while in simulation the power factor can, in theory, be magnified by a factor of 9, this will inevitably require motions with amplitudes and velocities that are higher than for the ranges characterized in chapter 3. The same would also apply to the limitations on forces produced.

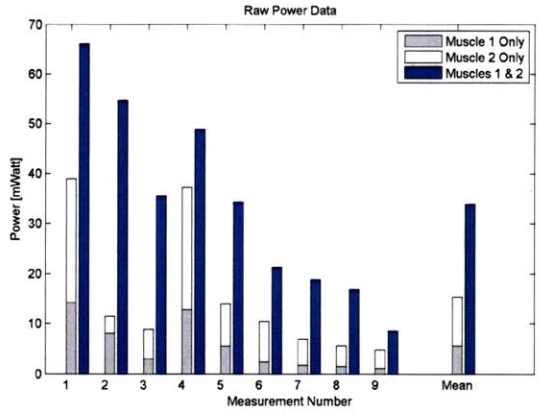

(a) Muscle Pair 1: Raw power data

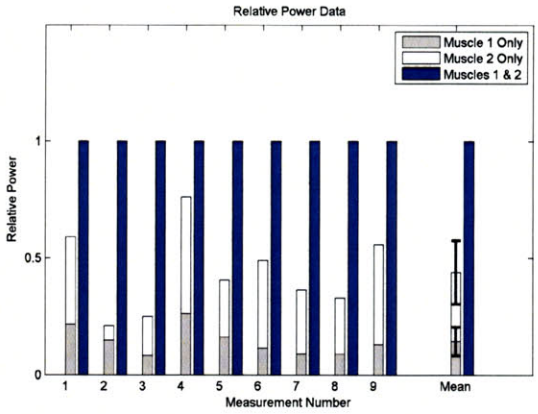

(b) Muscle Pair 1: Power normalized by P_{a+n}

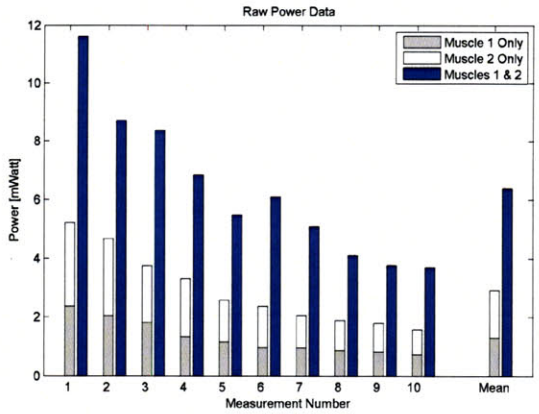

(c) Muscle Pair 2: Raw power data

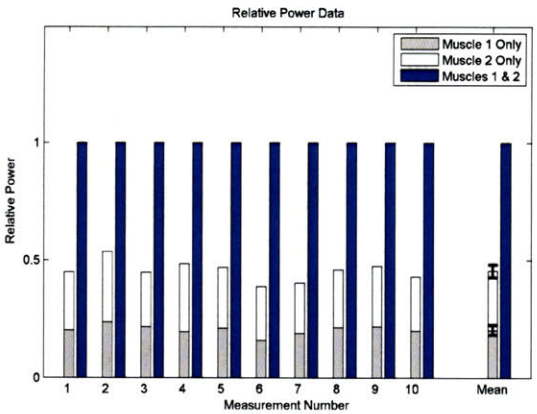

(d) Muscle Pair 2: Power normalized by P_{a+n}

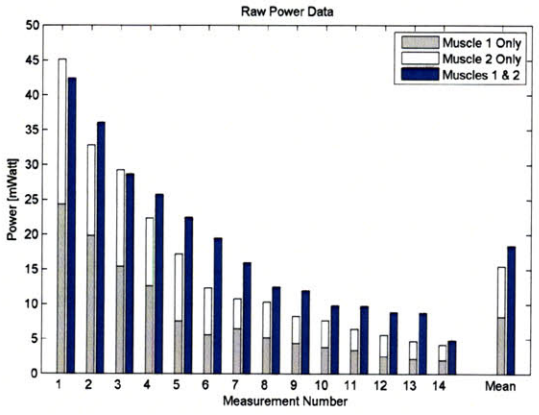

(e) Muscle Pair 3: Raw power data

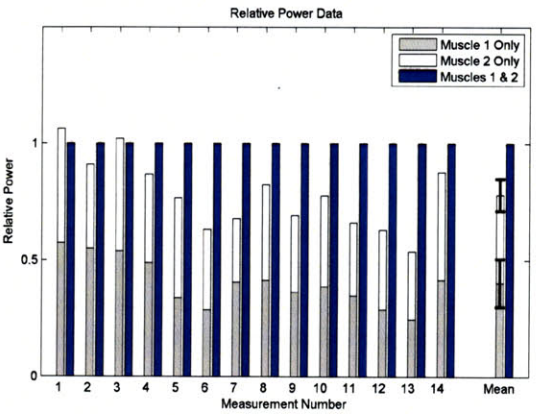

(f) Muscle Pair 3: Power normalized by P_{a+n}

Figure 5-7: Comparison of power output of individual muscles vs. power output of pairs. The left column (a, c and e) shows bar charts of absolute power measurements. The right side plots show data normalized by P_{a+n} for each measurement. The error bars in the normalized plots indicate $\pm$ one standard deviation. The measurements of P_a and P_n are stacked on top of each other to be compared with the measurements of P_{a+n}.

Chapter 6

Conclusions and Future Work

This thesis set out to answer the following questions:

- How is the power generating capability of muscle maximized?
- Are there situations in which antagonist co-activation leads to enhanced muscle power generation, and if so, what is the underlying mechanism?

Several tools were assembled to answer these questions. The first question was tackled via model-based optimal-control. Necessary conditions for optimality suggest that to generate maximal power, the optimal stimulation pattern takes a bang-bang form. This optimization was based on a muscle model obtained via identification techniques. Identification results show that the description of the contractile dynamics of muscles based on a Weiner model structure yields a reasonable approximation of their responses (approximately 75% VAF). These results were consistent across different specimens of the same muscle type. Surprisingly, the contractile forces, in their aggregate effects, were independent of the velocity of contraction.

To enable experimentation, necessary instrumentation was developed in chapter 2. The instrumentation hardware and software allow for a clear separation between load dynamics and muscle dynamics, and allow for the study of the interaction of muscles with loads. This is an important feature. Furthermore, we demonstrated a new method by which muscle workloop energetics can be evaluated, and antagonist pairs can be studied *in vitro*. The experimental results of this thesis could not be attained with standard, zero-admittance muscle workloop measurements.

The second question was tackled via computation of the optimal solutions as well as experimental verification of antagonist workloops. It was found that the impedance of muscles plays an important role in determining power-optimal stimulation. The optimal contraction frequency must include the effects of muscle impedance when coupled to the load. The level of muscle co-activation modulates the net contribution of muscle stiffness to the load dynamics. Depending on the desired excitation frequency, optimal stimulation parameters show direct modulation of co-activation about a baseline that is determined by the excitation-contraction dynamics of the muscle. Furthermore, antagonist muscles may cooperate to produce more power synergistically than compared to the sum of powers from the muscles acting on the load independently. Finally, an interpretation of our findings based on the classical engineering notion of impedance-matching was presented.

6.1 Future Work

Biological evidence of co-activation Are there examples of biological motions that use co-activation to enhance output energetics? For example, EMG readings of antagonist muscles actuating the pectoral fin in the bluegill sunfish show an overlap in stimulation [50] at steady-state locomotion. This implies co-stimulation, which is a stronger condition than co-activation. Is this co-activation due to a need for stabilization, a need for higher energetic performance, or is it perhaps a necessary consequence of the dynamics and kinematics of swimming?

What is the role of series elasticity? Tendons may provide a substantial amount of series elasticity [77]. The form of series elasticity affects the capability of a muscle to modulate the net impedance of muscle-tendon complex. If the tendons are linear springs (i.e. constant impedance), then this capability diminishes. If the tendon is a nonlinear hardening spring, then the stiffness due to co-activation depends more on tendon properties than muscle properties. The question becomes, to what extent is it possible to modulate the stiffness given the tendon properties, and what are the implications on optimized power energetics? Furthermore, from an anatomical perspective, is there any correlation between the stiffness of the tendons and the need to modulate impedance (from an energetics point of view)?

Investigating the role of series elasticity requires reformulation of the problem. Simply adding the elasticity in the model does not suffice since the resulting equations suffer from derivative causality (see [7], page 33), and thereby the dynamics of the system become ill-posed. Therefore small masses m_t are added to alleviate this problem, with the added advantage of modeling the muscle and tendon masses. The resulting model is shown in figure 6-1. While this problem is more complex (10th order system), the optimization techniques should still apply.

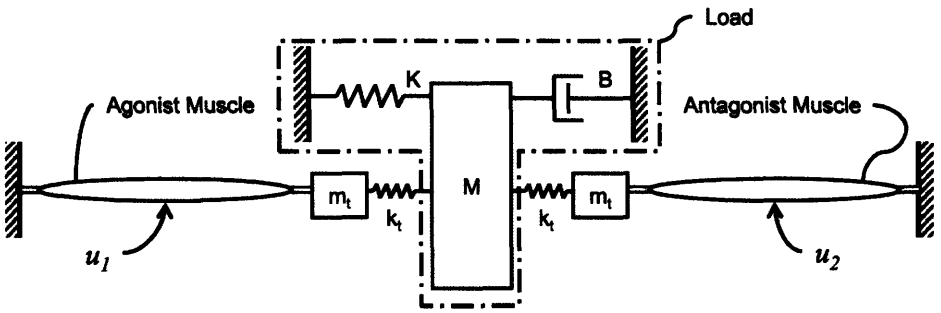

Figure 6-1: Problem setup with tendon elasticity. The tendon stiffness is shown as k_t.

On the apparent lack of velocity dependence In chapter 3 it became apparent that for the proposed model structure and the experimental protocol employed, the muscle response exhibited minimal dependence on velocity. Further work is needed to clarify if this is an artifact of the model-structure utilized and the particular experimental design, or if this is an intrinsic muscle property that becomes more apparent at sub-maximal stimulation levels.

From an energetics perspective, is muscle impedance a "bug" or a "feature"? The plots of figure 3 show that across a broad frequency range, bilinear muscles show the same peak energetic level as that obtained by impedance-free actuators. This may imply that the impedance properties of muscles are energetically undesirable (a "bug") since the required co-activation is metabolically expensive. On the other hand, one may ask if there are situations where the impedance of muscles enables higher levels of power generation. For example, muscle stiffness may create resonance out of non-resonant loads, and co-activation may be used to modulate the resonance frequency[1]. This would potentially lead to large energetic advantages. In this case, muscle impedance would be a desirable "feature".

Additional muscle functions We only looked at one particular biomechanical role for muscle: that of power generators. Many other roles are at least equally important (as illustrated in figure 1-1). Therefore many questions arise, including: How do the conclusions of this thesis change when muscles act as power absorbing dissipating elements [2]? Is the change simply a change of sign in the optimal control formulation, or are there other consequences that need to be accounted for? How can direct or feedback modulation of joint stiffness be implemented?

Implications on new actuator designs The results of this thesis may also have implications on new actuator design and control methodologies. The essential property of muscle that was exploited is that muscle stiffness increases with activation. This gave rise to the bilinear model, based on which the role of co-activation was studied. Several actuator materials do exhibit a similar increase in stiffness with activation. For example, Nickle-Titanium (NiTi) shape memory alloys exhibit a three fold increase in stiffness across their activation range while polyelectrolyte gel actuators experience upto a ten fold increase in stiffness.[41]. Since those actuators offer that same essential feature, the analytic and optimization tools developed in this thesis may be applicable as well.

Muscles as engineering actuators Can muscles be used as viable engineering as actuators in robotic systems? Monetemagno and colleagues [45] have demonstrated micro devices that are actuated by cultured muscle tissue. Similarly micro-fluidic systems have been used as perfusion systems to differentiate, align and engineer muscle tissue [3]. The ability to use muscle optimally in those circumstances, particularly from an energetic perspective is desirable. The work presented in this thesis sheds light on how to control the muscles of maximal energetic performance.

[1]This was suggested by Professor Neville Hogan.

Appendix A

The Structure and Function of Skeletal Muscle

A.1 The structure of skeletal muscle

What gives rise to muscle force? At the most basic level, muscles consist two types of parallel protein filaments: thick filaments and thin filaments. Thick filaments consist of the protein myosin with *myosin heads* that protrude radially outwards of the bundle. The thin filaments predominantly consist of the proteins actin, tropomyosin and troponin. Other proteins exist, such as titin for example, that play secondary roles in the contractile process, but provide structural integrity to the muscle [24].

The *sarcomere* is the smallest functional unit of the muscle. A sarcomere consists of a bundle of protein filaments that are organized in an hexagonal, inter-digitating manner. Sarcomeres are typically 1 micron in diameter, and 1-3 microns in length, depending on the contractile state of the muscle. Sarcomeres are connected in-series, forming *myofibrils.* These are wrapped in a network of electrical conduction pathways and stores of calcium ions called the *transverse tubules* and the *sarcoplasmic reticula.* Myofibrils are bundled to form muscles *fibers* which, in turn, form the muscle belly. The fibers extend along the length of the muscle, connecting two *tendons*, that form the mechanical interface with the skeletal structure.

The muscle interfaces with the nervous system via the *motor end plates* at the *neuromuscular junction.* The neuromuscular junction conducts the action potentials that encode motor commands from the nervous system to the muscle body. The end plates contain a collection of receptors of acetylcholine, a common neurotransmitter. This allows the muscle to interface with the nerves in a manner similar to synapses.

Once a descending action potential crosses the neuromuscular junction, it is conducted to the entire muscle volume via the sarcoplasimic reticula and the transverse tubules. The action potential temporarily depolarizes the cell membranes, and allows calcium ions (Ca^{2+}) to diffuse to the sarcoplasm by the action of calcium ion channels. The presence of Ca^{2+}, phosphocreatine, ATP and other metabolites allows the molecular contractile machinery to operate. The actin-troponon-tropomyosin complex undergoes conformal changes in the presence of calcium to expose myosin binding sites. Myosin heads, which are undergoing random motions attach to those binding sites forming transient linkages, or a *cross-bridges.* Cross-bridges execute two power strokes that generate relative forces between those two chains before detaching. Thus, the cross-bridge is the fundamental indivisible unit of muscle

contraction is the *cross-bridge*. The net result is a sliding motion between the two chains, which gives rise to the name sliding-filament model of contraction. The parallel action of a large number of cross-bridges acting simultaneously sum up to give rise to the muscle force. The active stiffness of the muscle is also largely dependent on the number of binding cross-bridges, which makes bilinear muscle models plausible.

A.2 Macro-scale mechanical properties

The structure of muscles and its contractile mechanisms give rise to a set of well defined biomechanical properties that are well studied. Those properties define a contractile force as a function of its activation, mechanical state (strain, relative velocity, and force), as well as its chemical state. Several cross-sections this relationship have been well defined in the biomechanics literature.

For example, a muscle's *passive force-length* characteristic measures the forces generated by the muscle as a function of its length in the absence of any activation. *Active force-length* relationships typically are characterized at at full activation (although sub-maximal relationships have also been reported). Such experiments have been reported at the level of individual muscles, fibers, sarcomeres, both in vivo and in vitro [56, 74]. Similarly *force-velocity* characteristics measure such quantities at constant velocities. Again, most canonical measurements characterize such properties either in the absence of activation (passive damping) or under full stimulation. These are just two examples of the many possible characterizations performed on muscle.

Appendix B

Impedance Matching

In this appendix, the classical engineering notion of impedance matching is considered in relation to the optimal power conditions described in the previous chapters. Impedance matching is an important concept heavily utilized in the design of antennas, robotic transmission systems, power grids, and others. This appendix serves the discussion in chapter 6 where we interpret the optimal control results in the context of impedance matching. The conditions are derived for three cases:

- An interconnection of linear systems operating in DC conditions
- An interconnection of linear systems operating in steady-state AC conditions
- An interconnection of a bilinear source and a linear load operating in steady-state DC conditions
- Finally, for bilinear system source and a linear load operating in steady-state AC conditions, the approach is only stated.

To generalize the discussion, we use generalized domain-independent variables. Generalized effort variables are $e(t), E(s)$ (time and frequency domains), and generalized flow variables are $f(t), F(s)$. In the mechanical domain, the effort variable is force and the flow variable is velocity. In electrical networks the effort is typically a voltage and the flow is the current to the network. The subscripts $(\cdot)_L$ and $(\cdot)_S$ denote load and source respectively. Therefore the load impedance is Z_L and the source impedance is Z_S. Optimal variables are denoted by an asterisk (e.g. Z_S^*), and conjugates of complex numbers are indicated by an apostrophe (e.g. Z_S').

It is important to clarify if the source is modeled as a Thevenin equivalent network or a Norton equivalent network. In a Thevenin equivalent network, the source is modeled as an ideal effort source is series with an internal impedance. In a Norton equivalent network, the source is modeled as an ideal flow source in parallel with an internal impedance. The distinction between the two is important because the *statement* regarding the conditions for optimal power requirements will be different under both cases. For example, in the linear DC case, if we are modeling the source as a Thevenin equivalent network, then it is generally desirable to *minimize* the series source impedance in order to maximize power transfer. In contrast, if we are modeling the source as a Norton equivalent network, then it is desirable to *maximize* the parallel source impedance in order to maximize power transfer. Converting from one network representation to another will show that the conditions are

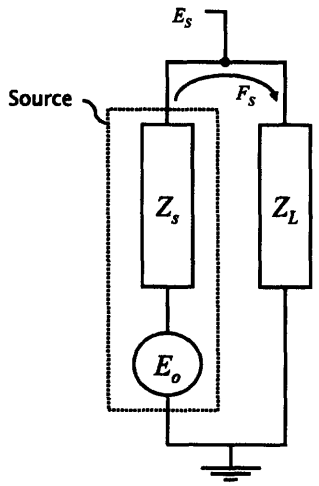

Figure B-1: Thevenin equivalent network

essentially identical – it is only the statements that differ. Therefore confusion may occur if the source model is not clearly defined. In the following discussion, we will consider only Thevenin equivalent networks.

B.1 Impedance Matching for Linear Systems

B.1.1 The linear DC case

Assume a Thevenin network representation of a source driving a load. The source is modeled as an ideal effort source providing constant effort E_o in series with a DC impedance (resistance in this case) Z_S as shown in figure B-1 . Since we are considering the DC case, the source and load impedance are real, nonnegative quantities. The flow in the network is denoted by F. Therefore, the source is described as

$$E_S = E_o - Z_S F_Z$$

A linear load is described by

$$E_L = Z_L F_L$$

When the two systems are interconnected, we impose the conditions of common flow and effort, that is $F_L = F_S = F$ and $E_S = E_L = E$. Solving simultaneously in terms of the common variables gives the following operating point:

$$\begin{aligned} F &= \frac{E_o}{Z_L + Z_S} \\ E &= E_o \frac{Z_L}{Z_L + Z_S} \end{aligned}$$

At this operating point, the power flow is given by

$$P = EF = E_o^2 \frac{Z_L}{(Z_L + Z_S)^2}$$

Now consider under what conditions is the power transfer maximized. The power is clearly dependent on E_o, Z_S and Z_L. Examine the effects of varying the three parameters on the net power flow:

Case 1: Maximizing over the effort source E_o

$$E_o^* = \arg\max_{E_o} P = \arg\max_{E_o} \left\{ E_o^2 \frac{Z_L}{(Z_L + Z_S)^2} \right\} = E_o^{max}$$

which implies that the optimal effort should be maximized to the highest possible value E_o^{max}.

Case 2: Maximizing over the source impedance (Z_S)

$$Z_S^* = \arg\max_{Z_S} P = \arg\max_{Z_S} \left\{ E_o^2 \frac{Z_L}{(Z_L + Z_S)^2} \right\} = Z_S^{min}$$

The power transfer is maximized by minimizing the denominator. Clearly for all non-negative Z_S, this is attained at the minimum possible value $Z_S = Z_S^{min}$.

Case 3: Maximizing over the load impedance (Z_L)

$$Z_L^* = \arg\max_{Z_L} P = \arg\max_{Z_L} \left\{ E_o^2 \frac{Z_L}{(Z_L + Z_S)^2} \right\}$$

To solve this, we write:

$$\begin{aligned} \frac{dP}{dZ_L} = 0 &= E_o^2 \left\{ \frac{1}{(Z_L + Z_S)^2} + \frac{Z_L(-2)}{(Z_L + Z_S)^3} \right\} \\ 0 &= (Z_L + Z_S) - 2Z_L \\ \Rightarrow \quad Z_L^* &= Z_S \end{aligned}$$

Therefore the optimal load impedance is equal to (or *matched* to) the source impedance. Having said that, the maximal power is given by

$$P^* = \frac{(E_o^{max})^2}{4Z_S^{min}}$$

In summary, for a DC network, and in the absence of other constraints, to maximize the power transfered from the source to the load, the effort source should be maximized. In parallel, the source impedance should be minimized. Finally, the load impedance should should be selected, when possible, to match that of the source.

B.1.2 The linear dynamic case

Now consider the situation when the source and load impedances are linear dynamical systems undergoing steady-state sinusoidal responses. Following the same analysis steps as before, assume that the ideal effort source is given by

$$E_o(t) = E_o e^{j\omega t}$$

The source effort is then given by

$$E_S = (E_o - Z_S \cdot F_S)\, e^{j\omega t}$$

where here Z_S, Z_L, F_S and F_L are in general complex quantities. The load is characterized by

$$E_L(t) = Z_L \cdot F_L e^{j\omega t}$$

Imposing interconnection constraints, we have $F_S = F_L = F$ and $E_S = E_L = E$. Solving simultaneously, we get:

$$\begin{aligned} F &= E_0 \frac{1}{Z_L + Z_S} e^{j\omega t} \\ E &= E_0 \frac{Z_L}{Z_L + Z_S} e^{j\omega t} \end{aligned}$$

The power is characterized by the following phasor quantity

$$\begin{aligned} P &= E \cdot F' \\ &= \frac{|E_o|^2 Z_L'}{|Z_L + Z_S|^2} \end{aligned}$$

Note that this is the complex power, which includes the real power (real part) and the reactive power (imaginary part). Also note that the frequency of power oscillation is twice that of the source. Our objective is to find what conditions give rise to maximal real power transfer.

The reactive power is not considered in steady state cases because it integrates to identically zero over a complete cycle. The real power is given by:

$$\begin{aligned} P_{real} &= \Re\left\{ |E_o|^2 \frac{Z_L'}{|Z_L + Z_S|^2} \right\} \\ &= |E_o|^2 \frac{R_L}{|Z_L + Z_S|^2} \\ &= |E_o|^2 \frac{R_L}{(R_L + R_S)^2 + (X_L + X_S)^2} \end{aligned}$$

where $Z_L = R_L + iX_L$ and $Z_S = R_S + iX_S$. Note that resistances $R_{(\cdot)}$ are non-negative, where as reactances $X_{(\cdot)}$ can be either positive or negative.

Similar to the discussion for the DC case, we now define three cases:

Case 1: Maximizing over the effort source E_o Similar to above

$$E_o^* = \arg\max_{E_o} P = \arg\max_{E_o} \left\{ |E_o|^2 \frac{R_L}{|Z_L + Z_S|^2} \right\} = E_o^{max}$$

which implies that the ideal effort source should be maximized to the highest possible limit E_o^{max}.

Case 2: Maximizing over the source impedance (Z_S) The source impedance consists of two parts (R_S and Z_S). We maximize over each separately

$$R_S^* = \arg\max_{R_S} P_{real} = \arg\max_{R_S} \left\{ |E_o|^2 \frac{R_L}{(R_L+R_S)^2+(X_L+X_S)^2} \right\} = R_S^{min}$$

$$X_S^* = \arg\max_{X_S} P_{real} = \arg\max_{X_S} \left\{ |E_o|^2 \frac{R_L}{(R_L+R_S)^2+(X_L+X_S)^2} \right\} = -X_L$$

Case 3: Maximizing over the load impedance (Z_L) Again, the impedance consists of two parts (R_S and Z_S). We maximize over each separately

$$X_L^* = \arg\max_{X_L} P = \arg\max_{X_L} \left\{ |E_o|^2 \frac{R_L}{(R_L+R_S)^2+(X_L+X_S)^2} \right\}$$

To solve this, we write:

$$\begin{aligned} 0 = \frac{dP_{real}}{dX_S} &= |E_o|^2 \frac{-R_L}{((R_L+R_S)^2+(X_L+X_S)^2)^2} 2(X_L+X_S) \\ 0 &= X_L+X_S \\ X_L &= -X_S \end{aligned} \tag{B.1}$$

$$R_L^* = \arg\max_{R_L} P = \arg\max_{R_L} \left\{ |E_o|^2 \frac{R_L}{(R_L+R_S)^2+(X_L+X_S)^2} \right\}$$

To solve this, we write:

$$\begin{aligned} \frac{dP_{real}}{dR_L} = 0 &= |E_o|^2 \frac{1}{(R_L+R_S)^2+(X_L+X_S)^2} + \frac{-E_o^2 \cdot R_L \cdot 2 \cdot (R_L+R_S)}{((R_L+R_S)^2+(X_L+X_S)^2)^2} \\ 0 &= |E_o|^2 \frac{1}{(R_L+R_S)^2+(X_L+X_S)^2} \left[1 - \frac{R_L \cdot 2(R_L+R_S)}{(R_L+R_S)^2+(X_L+X_S)^2} \right] \\ R_L &= \sqrt{R_S^2+(X_L+X_S)^2} \\ &= R_S \qquad \text{if } X_L = -X_S \text{ as from above} \end{aligned} \tag{B.2}$$

In summary, for the dynamic case, and in the absence of other constraints, to maximize the power transfered from the source to the load, the effort source should be maximized. In parallel, the real part source impedance should be minimized, and then, the load impedance should match the complex conjugate of the source impedance, or $Z_L^*(j\omega) = Z_S'(j\omega)$.

Complex Conjugate Impedances

What does it mean to have the complex conjugate impedance of a mechanical system? The impedance of a mass-spring-damper system is given by

$$\begin{aligned} I(j\omega) &= \frac{-M\omega^2 + jB\omega + K}{j\omega} \\ &= B + j\left(M\omega - \frac{K}{\omega}\right) \end{aligned}$$

Therefore the complex conjugate of this can be *attained at a particular matching frequency* ω_m as such:

$$I^*(j\omega) = B + j\left(\frac{K}{\omega_m} - M\omega_m\right)$$

which can be attained, for example, if the mass of the conjugate system has a *mass* of (K/ω^2) and a *stiffness* of $(M\omega^2)$. See plots below for examples.

B.2 Impedance Matching for Linear Loads with Bilinear Sources

What happens in the case of a bilinear source? In this section we consider

The DC Bilinear Case

Consider a case where a muscle is attached to a mass-spring-damper system. The stiffness and damping of the muscle are activation dependent, and are given by the bilinear formulation. In terms of impedances, we may write (while abusing notations):

$$Z_S = \underbrace{\left(b^o + \frac{k^o}{s}\right)}_{Z_S^o} + \underbrace{\left(\tilde{b} + \frac{\tilde{k}}{s}\right)}_{\tilde{Z}_S} E_o$$

From the power formulation, recall that

$$P = E \cdot F = \frac{E_o^2 Z_L}{(Z_L + Z_S)^2}$$

To compute the optimal activation (E_o) that gives us the most power, we write

$$\begin{aligned} \frac{dP}{dE_o} &= \frac{\partial P}{\partial E_o} + \frac{\partial P}{\partial Z_S}\frac{\partial Z_S}{\partial E_o} \\ 0 &= \frac{2E_o Z_L}{(Z_L + Z_S)^2} + \frac{-2E_o^2 Z_L}{(Z_L + Z_S)^3}\left(\tilde{b} + \frac{\tilde{k}}{s}\right) \\ 0 &= Z_L(Z_L + Z_S) - E_o Z_L\left(\tilde{b} + \frac{\tilde{k}}{s}\right) \\ 0 &= E_o(Z_L + Z_S Z_S^o) \end{aligned}$$

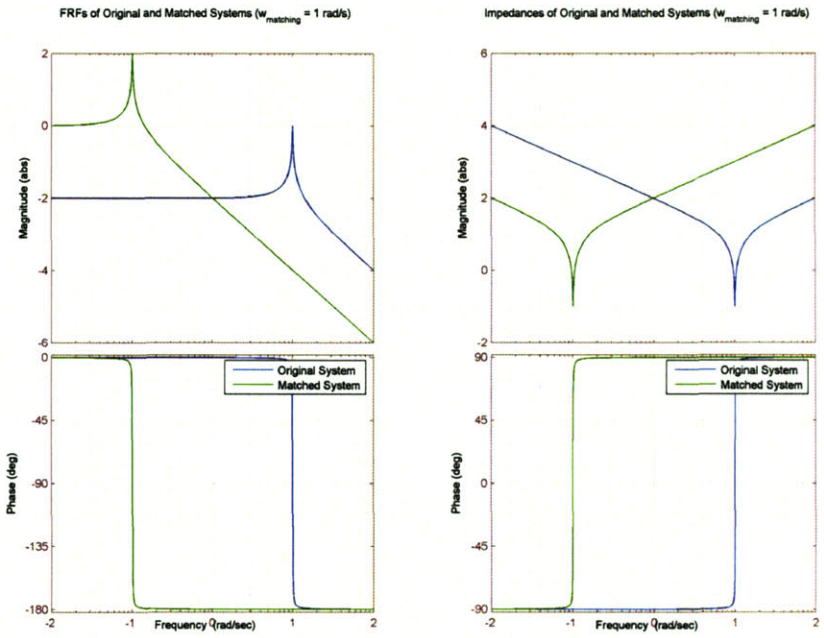

Figure B-2: Impedance matched at $\omega = 1$. Original system parameters: M = 1; K = 100; B = 0.1

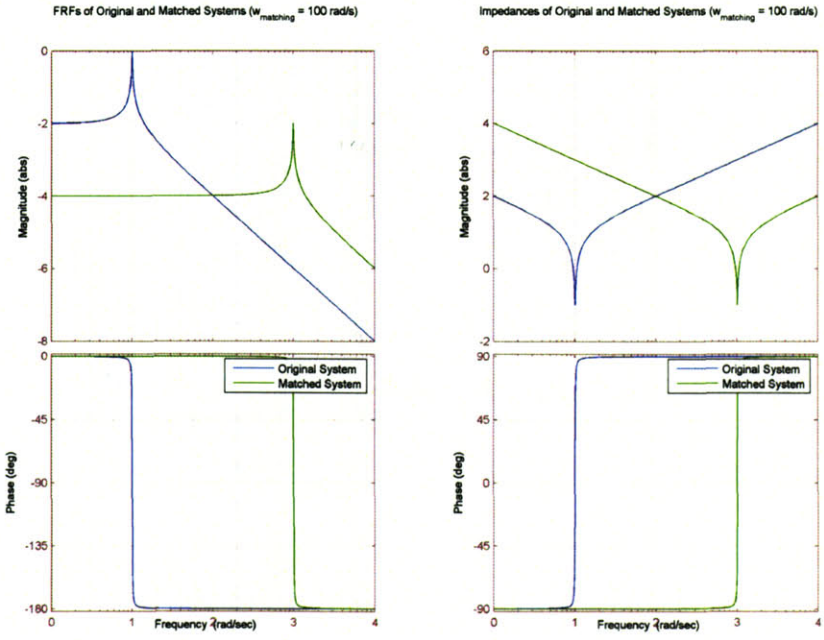

Figure B-3: Impedance matched at $\omega = 1$. Original system parameters: M = 1; K = 100; B = 0.1

which clearly is satisfied when $E_o = 0$, which corresponds to a minimum rather than a maximum. The power actually has no maximum. It's supremum is never attained. This supremum is given by

$$\lim_{E_o \to \infty} P = \frac{Z_L}{\tilde{Z}_S^2}$$

which is a complex number that indicates both the real and reactive power.

The Dynamic Bilinear Case

In such an analysis, one can no longer write the expression in a simple form as above. The problem will need to be cast in a optimal control framework as in chapter 4.

Appendix C

Simulation of Periodic Solutions

This appendix presents a method of computing periodic solutions of system 4.5 due to the periodic control input. One way to simulate the system is to integrate equation 4.5 (perhaps via Runge-Kutta integrators) starting with zero initial conditions. We may integrate the system for a sufficiently long duration until the homogeneous solution dies out, leaving only the forced periodic response. In our studies, we found that this approach is not practical because the computational time is very long. This is particularly important since we will need to evaluate many cases to achieve a systematic search over the parameters of the input functions.

An alternative, and less time consuming approach is to *directly* find a periodic solution that satisfies the model equations. In this appendix, we describe how this is achieved. The method is based on harmonic balancing, and is described as follows.

We need to find *periodic* solution of the state vector $\mathbf{x}$ due to a periodic input vector $\mathbf{u}$ and satisfies the system differential equation 4.5. First let us write the control inputs in terms of their Fourier series coefficients

$$u_1 = \sum_{k=-\infty}^{\infty} c_{u_1 k} e^{i\omega k t}; \qquad u_2 = \sum_{k=-\infty}^{\infty} c_{u_2 k} e^{i\omega k t};$$

Next we recognize that the solution of the system will also be periodic. Therefore, the

solution for each of the states and their derivatives can be written in terms of Fourier series:

$$\alpha_1 = \sum_{k=-\infty}^{\infty} c_{\alpha_1 k} e^{i\omega k t}; \qquad \dot{\alpha}_1 = \sum_{k=-\infty}^{\infty} c_{\alpha_1 k} i\omega k e^{i\omega k t};$$

$$\beta_1 = \sum_{k=-\infty}^{\infty} c_{\beta_1 k} e^{i\omega k t}; \qquad \dot{\beta}_1 = \sum_{k=-\infty}^{\infty} c_{\beta_1 k} i\omega k e^{i\omega k t};$$

$$\alpha_2 = \sum_{k=-\infty}^{\infty} c_{\alpha_2 k} e^{i\omega k t}; \qquad \dot{\alpha}_2 = \sum_{k=-\infty}^{\infty} c_{\alpha_2 k} i\omega k e^{i\omega k t};$$

$$\beta_2 = \sum_{k=-\infty}^{\infty} c_{\beta_2 k} e^{i\omega k t}; \qquad \dot{\beta}_2 = \sum_{k=-\infty}^{\infty} c_{\beta_2 k} i\omega k e^{i\omega k t};$$

$$x = \sum_{k=-\infty}^{\infty} c_{xk} e^{i\omega k t}; \qquad \dot{x} = \sum_{k=-\infty}^{\infty} c_{xk} i\omega k e^{i\omega k t};$$

$$\dot{x} = \sum_{k=-\infty}^{\infty} c_{\dot{x}k} e^{i\omega k t}; \qquad \ddot{x} = \sum_{k=-\infty}^{\infty} c_{\dot{x}k} i\omega k e^{i\omega k t};$$

The differential equation 4.5 represents a constraint relating the Fourier coefficients of the different states $c_{.k}$. If the system was linear, then those constraints would also be linear, and solving for the coefficients would be straightforward. However, because of the nonlinearity in the forcing function, the constraints in the coefficients become nonlinear as well.

By judicious choice of solving for parameters, and exploiting the multi-linear structure, the problem can be solved by a cascade of least-squares regression computations, that are relatively fast. We proceed as follows. From equation (4.5), it is clear that the dynamics of $\alpha_1, \beta_1, \alpha_2, \beta_2$ are linear in u_1 and u_2. Therefore, the Fourier coefficients of those variables are directly related to the Fourier coefficients of the control inputs by the value of the transfer functions evaluated at $s = i\omega k$. Therefore,

$$\begin{aligned} c_{\beta_1 k} &= \frac{p_{u_1} c_{u_1 k}}{i\omega k - p_{\beta_1}} \\ c_{\alpha_1 k} &= \frac{c_{\beta_1 k}}{i\omega k - p_{\alpha_1}} \\ c_{\beta_2 k} &= \frac{p_{u_2} c_{u_2 k}}{i\omega k - p_{\beta_2}} \\ c_{\alpha_2 k} &= \frac{c_{\beta_2 k}}{i\omega k - p_{\alpha_2}} \end{aligned} \tag{C.1}$$

Since the forcing term is nonlinear, we use a slightly different approach to solve for c_{xk}

$$\begin{aligned} M\ddot{x} + B\dot{x} + Kx = (A_2 - A_1) - B_2(x - x_2^o) - B_1(x_1^o + x) + (C_2\alpha_2 - C_1\alpha_1) \\ - D_2(x - x_2^o)\alpha_2 - D_1(x_1^o + x)\alpha_1 \end{aligned}$$

Substituting $x = \sum c_{xk} e^{i\omega k t}$ we get

$$\overbrace{\left[-\omega^2 k^2 M + i\omega k B + K + B_1 + B_2 + D_1\alpha_1(t) + D_2\alpha_2(t)\right] e^{i\omega k t}}^{N_k(t)} c_{xk}$$
$$=$$
$$\underbrace{A_2 - A_1 + B_2 x_2^0 - B_1 x_1^0 + (C_2 + D_2 x_2^0)\alpha_2(t) - (C_1 + D_1 x_1^0)\alpha_1(t)}_{b_k(t)}$$

or

$$N_k(t) c_{xk} \quad = b_k(t)$$

Writing this last expression for different k and t, we get

$$\begin{bmatrix} N_k(t_o) \\ \vdots \\ N_k(t) \\ \vdots \\ N_k(t_f) \end{bmatrix} c_{xk} = \begin{bmatrix} b_k(t_o) \\ \vdots \\ b_k(t) \\ \vdots \\ b_k(t_f) \end{bmatrix}$$
$$\mathbf{N} c_{xk} = \mathbf{b}$$
$$c_{xk} = (\mathbf{N}^T\mathbf{N})^{-1}\mathbf{N}^T\mathbf{b} \tag{C.2}$$

Finally,

$$c_{\dot{x}k} = i\omega k c_{xk} \tag{C.3}$$

In summary, the procedure becomes:

1. Compute $c_{u_1 k}$ and $c_{u_2 k}$, the Fourier coefficients of u_1 and u_2 respectively.
2. Using $c_{u_1 k}$ and $c_{u_2 k}$, compute the Fourier coefficients $c_{\beta_1 k}$, $c_{\alpha_1 k}$, $c_{\beta_2 k}$, and $c_{\alpha_1 k}$ as in equations C.1.
3. By inverse Fourier transforms, compute the states $\beta_1(t)$, $\alpha_1(t)$, $\beta_2(t)$, and $\alpha_2(t)$.
4. Compute the coefficients c_{x_k} and $c_{\dot{x}_k}$ using equations C.2 and C.3..
5. Compute $x(t)$ and $\dot{x}(t)$ by inverse Fourier transforms.
6. Compute the power $P(t) = \dot{x}(t) \cdot F_{net}(t)$

Bibliography

[1] A. Ahn, R. Monti, and A. Biewener. In vivo and in vitro heterogeneity of segment length changes in the semimembranosus muscle of the toad. *J. Physiol.*, 549:877–888, 2003.

[2] Anna Ahn and Robert Full. A motor and a brake: Two leg extensor muscles acting at the same joint manage energy differently in a running insect. *J. Exp. Biol.*, 205:379–389, 2002.

[3] Xavier Figueroa-Masot Anna Tourovskaia and Albert Folch. Differentiation-on-a-chip: A microfluidic platform for long-term cell culture studies. *Lab on Chip*, 5:14–19, 2005.

[4] Alan S. Bahler, John T. Fales, and Kenneth L. Zieler. The dynamic properties of mammalian skeletal muscle. *J. General. Physiol.*, 51:369–384, 1968.

[5] P. Bawa, A. Mannard, and R. B. Stein. Effects of elastic loads on the contractions of cat muscles. *Biol. Cybernetics*, 22:129–137, 1976.

[6] P. Bawa, A. Mannard, and R. B. Stein. Predictions and experimental tests of a visco-elastic muscle model using elastic and inertial loads. *Biol. Cybernetics*, 22:139–145, 1976.

[7] Max Berniker. *Linearity, Motor Primitives and Low-Dimensionality in the Spinal Organization of Motor Control.* PhD thesis, Massachusetts Institute of Technology (MIT), 2005.

[8] Leonas Bernotas, Patrick E. Crago, and Howard J. Chizeck. A discrete-time model of electrically stimulated muscle. *IEEE Trans. Biomed. Eng.*, 33(9):829–838, September 1986.

[9] I. E. Brown and G. E. Loeb. Design of a mathematical model of force in whole skeletal muscle. *Proceedings of the IEEE EMBC and CBMEC*, pages 1243–1244, 1999.

[10] Arthur E. Bryson and Yu-Chi Ho. *Applied Optimal Control: Optimization, Estimation and Control.* John Wiley & Sons, New York, 1975.

[11] Etienne Burdet, Rieko Osu, David W. Franklin, Theodore E. Milner, and Mitsuo Kawato. The central nervous system stabilizes unstable dynamics by learning optimal impedance. *Nature*, 414:446–449, November 2001.

[12] Howard J. Chizeck, Seokjoo Chang, Richard B. Stein, Avram Scheiner, and Donald C. Ferencz. Identification of electrically stimulated quadriceps muscles in paraplegic subjects. *IEEE Trans. Biomed. Eng.*, 46(1):51–61, January 1999.

[13] Howard J. Chizeck, Patrick E. Crago, and Leon Kofman. Robust closed loop control of isometric muscle force using pulsewidth modulation. *IEEE Trans. Biomed. Eng.*, 35(7):510–517, July 1988.

[14] Howard J. Chizeck, Ning Lan, Linda Streeter Palmieri, and Patrick E. Crago. Feedback control of electrically stimulated muscle using simultaneous pulse width and stimulus period modulation. *IEEE Trans. Biomed. Eng.*, 38(12):1224–1234, December 1991.

[15] Patrick E. Crago, Richard Nakai, and Howard J. Chizeck. Feedback regulation of hand grasp opening and contact force during stimulation of paralyzed muscle. *IEEE Trans. Biomed. Eng.*, 38(1):17–28, January 1991.

[16] E. Don Stevens D. Zyme. Effect of cycle frequency and excursion amplitude on work done by rat diaphragm muscle. *Can. J. of Zool.*, 67:1294–1299, 1989.

[17] L. del Re, F. Kraus, J. Schultheiss, and H. Gerber. Self-tuning pid controller for lower limb fes with nonlinear compensation. In *Proceedings of the American Control Conference*, pages 2015–2019, 1994.

[18] Michael H. Dickinson, Claire T. Farley, Robert J. Full, M. A. R. Koehl, Rodger Kram, and Steven Lehman. How animals move: An integrative view. *Science*, 288(2):100–106, 2000.

[19] Stephen J. Dorgan and Mark J. OMalley. A nonlinear mathematical model of electrically stimulated skeletal muscle. *IEEE Trans. Neural Syst. Rehab. Eng.*, 5(2):179–194, June 1997.

[20] William K. Durfee. Task-based methods for evaluating electrically stimulated antagonist muscle pairs. *IEEE Trans. Biomed. Eng.*, 36(3):309–321, March 1989.

[21] William K. Durfee and Karon E. MacLean. Methods for estimating isometric recruitment curves of electrically stimulated muscle. *IEEE Trans. Biomed. Eng.*, 36(7):654–666, July 1989.

[22] William K. Durfee and Karen I. Palmer. Estimation of force-activation, force-length and force-velocity properties in isolated, electrically stimulated muscle. *IEEE Trans. Biomed. Eng.*, 41(3):205–216, March 1994.

[23] K. A. P. Edman. The velocity of unloaded shortening and its relation to sarcomere length and isometric force in vertebrate muscle fibres. *J. Physiol.*, 291:143–159, 1978.

[24] James H. Schwartz Eric R. Kandell and Thomas M. Jessell. *Principles of Neurosciences, 4th ed.* McGraw-Hill, 2000.

[25] Prisca C. Eser, Nick de N. Donaldson, Hans Knecht, and Edgar Stussi. Influence of different stimulation frequencies on power output and fatigue during FES-cycling in recently injured SCI people. *IEEE Trans. Neural Syst. Rehab. Eng.*, 11(3):236–240, September 2003.

[26] Waleed Farahat and Hugh Herr. An apparatus for characterization and control of isolated muscle. *IEEE Trans. Neural Syst. Rehab. Eng.*, 13(4):473–481, December 2005.

[27] Waleed Farahat and Hugh Herr. A method for identification of electrically stimulated muscle. In *Proceedings of the 27th International Conference of the IEEE Engineering in Medicine and Biology Society, Shanghai, China*, 2005.

[28] Robert Fruend. Lecture notes on nonlinear programming (course notes for 6.252), 2004.

[29] P.M.H. Rack G.C. Joyce and D.R. Westbury. The mechanical properties of cat soleus muscle during controlled lengthening and shortening movements. *Journal of Physiology*, 204:461–467, 1969.

[30] Joseph Giuffrida and Patrick E. Crago. Reciprocal EMG control of elbow extension by FES. *IEEE Trans. Neural Syst. Rehab. Eng.*, 9(4):338–345, December 2001.

[31] Henrik Gollee, Ken J. Hunt, and Duncan E. Wood. New results in feedback control of unsupported standing in paraplegia. *IEEE Trans. Neural Syst. Rehab. Eng.*, 12(1):73–80, March 2004.

[32] Hiroaki Gomi and Rieko Osu. Task-dependent viscoelasticity of human multijoint arm and its spatial characteristics for interaction with environments. *J. Neuroscience*, 18(21):89658978, November 1998.

[33] Peter Gorman and Thomas Mortimer. The effect of stimulus parameters on the recruitement characteristics of derect nerve stimulation. *IEEE Trans. Biomed. Eng.*, 30(7):407–414, July 1983.

[34] A. V. Hill. The heat of shortening and the dynamic constants of muscle. *Proc. R. Soc. London*, 126:136–195, 1938.

[35] A. V. Hill. The series elastic component of muscle. *Proc. R. Soc. London*, 137:237–280, 1950.

[36] A. V. Hill. The effects of series compliance on the tension developed in the muscle twitch. *Proc. R. Soc. London*, 138:325–329, 1951.

[37] Neville Hogan. Adaptive control of mechanical impedance by coactivation of agonist muscles. *IEEE Trans. Automat. Contr.*, 29(8):681–690, August 1984.

[38] Neville Hogan. *Multiple Muscle Systems: Biomechanics and Movement Organization*, chapter 9. Springer-Verlag, 1990.

[39] Neville Hogan. Muscle models. course notes for 2.183 - biomechanics and neural control of movement, Spring 2003.

[40] I. W. Hunter and M. J. Korenberg. The identification of nonlinear biological systems: Wiener and hammerstein cascade models. *Biological Cybernetics*, 55:135–144, 1986.

[41] Ian W. Hunter and Serge Lafontaine. A comparison of muscle with artificial actuators. *IEEE Solid-State Sensor and Actuator Workshop*, pages 178–165, 1992.

[42] A. F. Huxely and R. M. Simmons. Mechanical properties of the cross-bridges of frog striated muscle. *J. Physiol.*, 218:59–60, October 1971.

[43] E. Don Stevens J. Renaud. A comparison between field habits and contractile performance of frog and toad sartorius muscle. *J. Comp. Physiol.*, 151:127–131, 1983.

[44] Saso Jezernik, Ruben Wassink, and Thierry Keller. Sliding mode closed loop control of FES: Controlling the shank movement. *IEEE Trans. Biomed. Eng.*, 51(2):263–272, February 2004.

[45] Jacob J. Schmidt Jianzhong Xi and Carlo D. Montemagno. Self-assembled microdevices driven by muscle. *Nature Materials*, 4:180–184, February 2005.

[46] Robert Josephson. Mechanical power output from striated muscle during cyclic contraction. *J. Exp. Biol.*, 114:493–512, 1985.

[47] Robert Josephson and Darrell Stokes. Strain, muscle length and work output in a crab muscle. *J. Exp. Biol.*, 145:45–61, 1989.

[48] A. Krylow and W. Zev Rymer. Role of intrinsic muscle properties in producing smooth movements. *IEEE Trans. Biomed. Eng.*, 44(2):165–175, February 1997.

[49] Ning Lan, Patrick E. Crago, and Howard J. Chizeck. Feedback control methods for task regulation by electrical stimulation of muscles. *IEEE Trans. Biomed. Eng.*, 38(12):1213–1223, December 1991.

[50] George V Lauder, Peter G A Madden, Rajat Mittal, Haibo Dong, and Meliha Bozkurttas. Locomotion with flexible propulsors: I. experimental analysis of pectoral fin swimming in sunfish. *Bioinspiration & Biomimetics*, 1(4):S25–S34, 2006.

[51] Lennart Ljung. *System Idenfication: Theory for the User.* Prentice-Hall, second edition, 1990.

[52] G. E. Loeb, F.J.R. Richmond, S. Olney, T. Cameron, A.C. Dupont, K. Hood, and R.A.Peck. BION - bionic neurons for functional and therapeutic electrical stimulation. In *Proceedings of the 20th Conference Annual International Conference of the IEEE Engineering in Medicine and Biology*, pages 2305–2307, 1998.

[53] E. Luiker and E. Don Stevens. Effect of stimulus train duration and cycle frequency on the capacity to do work in the pectoral fin of muscle of the pumpkinseed sunfish, *Lopomis gibbosus. Can. J. of Zool.*, 71:2185–2189, 1993.

[54] S. Ma. *Activation dynamics for the distribution-moment model of muscle.* PhD thesis, Washington University, St. Louis, MO, 1988.

[55] Hidenobu Mashima. Force-velocity relation and contractility in striated muscles. *Jap. J. of Phys.*, 34:1–17, 1984.

[56] Thomas A. McMahon. *Muscles, Reflexes and Locomotion.* Princeton University Press, New Jersey, 1984.

[57] Petra Mela, Peter H. Veltink, Peter A. Huijing, Stanley Salmons, and Jonathan C. Jarvis. The optimal stimulation pattern for skeletal muscle is dependent on muscle length. *IEEE Trans. Neural Syst. Rehab. Eng.*, 10(2):85–92, June 2002.

[58] M. Munih, K. Hunt, and N. Donalson. Variation of recruitment nonlinearity and dynamic response of ankle plantarflexors. *Medical Engineering & Physics*, 22:97–107, 2000.

[59] William R. Murray and Neville Hogan. Co-contraction of antagonist muscles: Predictions and observations. In *Proceedings of the IEEE Engineering in Medicine and Biology Society 10th Annual International Conference*, pages 1926–1927, 1988.

[60] John M. Olson and Richard L. Marsh. Activation patterns and length changes in hindlimb muscles of the bullfrog rana catesbeiana during jumping. *J. Exp. Biol*, 201:2763–2777, 1998.

[61] Robert Riener, Maurizio Ferrarin, Esteban Enrique Pavan, and Carlo Albino Frigo. Patient driven control of FES supported standing up and sitting down: Experimental results. *IEEE Trans. Neural Syst. Rehab. Eng.*, 8(4):523–529, December 2000.

[62] Robert Riener and Thomas Fuhr. Patient driven control of FES supported standing up: A simulation study. *IEEE Trans. Neural Syst. Rehab. Eng.*, 6(2):113–124, June 1998.

[63] Robert Riener, Jochen Quintern, and Cunther Schmidt. Biomechanical model of the human knee evaluated by neuromuscular stimulation. *J. Biomechanics*, 29(9):1157–1167, 1996.

[64] Steven J. Schroeck, William C. Messner, and Robert J. McNab. On compensator design for linear time-invariant dual-input single-output systems. *IEEE/ASME Trans. Mechatronics*, 6(1):50–57, March 2001.

[65] Aurora Scientific. http://www.aurorascientific.com/, 2004.

[66] Lawrence F. Shampine and Jacek Kierzenka. Solving boundary value problems for ordinary differential equations in MATLAB using `bvp4c`, 2000.

[67] Guayhaur Shue, Patrick E. Crago, and Howard J. Chizeck. Muscle-joint models incorporating activation dynamics, moment-angle and moment-velocity properties. *IEEE Trans. Biomed. Eng.*, 42(2):212–223, February 1995.

[68] E. Don Stevens. Effect of pH and stimulus phase on work done by isolated frog sartorius muscle during cyclical contraction. *J. Muscle Research and Cell Motility*, 9:329–333, 1988.

[69] E. Don Stevens. The pattern of stimulation influences the amount of oscillatory work done by frog muscle. *Journal of Physiology*, 494(1):279–285, 1996.

[70] Darrell Stokes and Robert Josephson. The mechanical power output of a crab respiratory muscle. *J. Exp. Biol.*, 140:287–299, 1988.

[71] Peter H. Veltink, Howard J. Chizeck, Patrick E. Crago, and Ahmed El-Bialy. Nonlinear joint angle control of artifically stimulated muscle. *IEEE Trans. Biomed. Eng.*, 39(4):368–380, April 1992.

[72] George F. Wilhere, Patrick E. Crago, and Howard J. Chizeck. Design and evaluation of a digital closed loop controller for the regulation of muscle force by recruitment modulation. *IEEE Trans. Biomed. Eng.*, 32(9):668–676, September 1985.

[73] J.M. Winters and S.L-Y. Woo, editors. *Multiple Muscle Systems: Biomechanics and Movement Organization.* Springer-Verlag, 1990.

[74] Roger C. Woledge, Nancy A. Curtin, and Earl Homsher. *Energetic Aspects of Muscle Contraction.* Monographs of the Physiological Society No. 41. Academic Press, San Diego, 1985.

[75] A. Barziali Z. Karu, W. Durfee. Reducing muscle fatigue in FES applications by stimulating with n-let pulse trains. *IEEE Trans. Biomed. Eng.*, 42(8):809–817, August 1995.

[76] George I. Zahalak. *Multiple Muscle Systems: Biomechanics and Movement Organization*, chapter 1. Springer-Verlag, 1990.

[77] Felix Zajac. Muscle and tendon: Properties, models, scaling and application to biomechanics and motor control. *Crit. Rev. in Biomedical Engineering*, 17(2), 1989.

[78] Bing-He Zhou, S. R. Katz, R. V. Baratta, M. Solomonow, and R. D. D'Ambrosia. Evaluation of antagonist coactivation strategies elicited from electrically stimulated muscles under load-moving conditions. *IEEE Trans. Biomed. Eng.*, 44:620–633, July 1997.